

INVESTIGATING DAMAGE IN DISCONTINUOUS FIBER COMPOSITES
THROUGH COUPLED IN-SITU X-RAY TOMOGRAPHY EXPERIMENTS AND
SIMULATIONS

A Dissertation
Submitted to the Faculty
of
Purdue University
by
Imad Hanhan

In Partial Fulfillment of the
Requirements for the Degree
of
Doctor of Philosophy

May 2020
Purdue University
West Lafayette, Indiana

THE PURDUE UNIVERSITY GRADUATE SCHOOL
STATEMENT OF DISSERTATION APPROVAL

Dr. Michael D. Sangid, Chair

Elmer F. Bruhn Associate Professor,
School of Aeronautics and Astronautics

Dr. Chelsea Davis

School of Materials Engineering

Dr. Tyler Tallman

School of Aeronautics and Astronautics

Dr. Charles L. Tucker III

Alexander D. Rankin Professor Emeritus,
University of Illinois at Urbana-Champaign

Approved by:

Dr. Gregory Blaisdell

Head of the Graduate Program of Aeronautics and Astronautics

To my parents, Amin and Gloria, and to my dog, Miller: without your unconditional love and support, this would not have been possible.

ACKNOWLEDGMENTS

I would first like to thank my advisor, Dr. Michael Sangid, for his guidance and support throughout my Master's and PhD degrees; his mentorship throughout my research career has allowed me to grow both academically and professionally. Thank you to my colleague Ronald Agyei who worked very closely with me on the 3D fiber detection aspects of this work. Thank you also to all of my laboratory colleagues, especially John Rotella who helped with certain aspects of the destructive analysis, and Ritwik Bandyopadhyay, Prithvirajan Veerappan, and Dr. Kartik Kapoor for providing advice when I was troubleshooting aspects of the simulations in this work; you have all helped create a fun and collaborative work environment.

I would also like to thank my committee members, Dr. Chelsea Davis, Dr. Tyler Tallman, and especially Dr. Charles L. Tucker III, for generously offering their time and guidance throughout my PhD. Thank you to Pavel Shevchenko and Dr. Francesco De Carlo from Argonne National Laboratory, and Dr. Xianghui Xiao who is currently at Brookhaven National Laboratory, for their help and guidance in acquiring the X-ray tomography data; I'm very grateful for the many skills I've developed throughout my experiences at Argonne National Laboratory.

Thank you to Dr. Alan Wedgewood of Dupont for providing the composite material studied in this work. Thank you also to Dr. Bhisham Sharma, currently at Wichita State University, for developing the initial 2D characterization algorithms used in the initial stages of the destructive analysis. Additionally, thank you to Steve Carter for providing the AA7050 fatigue data, which was used in the verification of the image processing tools developed in this work.

The use of the Advanced Photon Source at Argonne National Laboratory was supported by the US Department of Energy, Office of Science, Office of Basic Energy Sciences, under contract No. DE-AC02-06CH11357. Thank you to the following

funding agencies for their support of this work: the National Science Foundation (NSF) Graduate Research Fellowship Program Award Number DGE-1333468, the NSF CMMI MoM Award No. 1662554, and the Defense Advanced Research Projects Agency Award No. HR0011-17-2-0069.

TABLE OF CONTENTS

	Page
LIST OF TABLES	viii
LIST OF FIGURES	ix
ABSTRACT	xiv
1 INTRODUCTION	1
1.1 Background	1
1.2 Research Contributions	4
2 TOMOGRAPHY IMAGE PROCESSING	6
2.1 Introduction	6
2.2 Methods	10
2.3 Visualizing and Classifying 3D Data Using ModLayer	12
2.3.1 Identifying damage in 3D time lapse images	12
2.3.2 Correcting feature segmentation in tomography images of a composite material's microstructure	14
2.3.3 Correcting feature segmentation of <i>in-situ</i> AA7050 fatigue crack growth tomography images	16
2.4 Conclusion	18
3 NON-DESTRUCTIVE AND DESTRUCTIVE ANALYSIS	20
3.1 Introduction	20
3.2 Materials and Methods	22
3.2.1 Composite Material	22
3.2.2 Defining Fiber Orientation	24
3.3 Non-destructive X-ray μ -CT and Feature Detection	25
3.4 Destructive Optical Microscopy	27
3.4.1 Sectioning, polishing, and plasma etching	27
3.4.2 Destructively determining the sign of the out-of-plane angle	29
3.4.3 Destructively measuring the fiber length distribution	33
3.5 Results	33
3.5.1 Fiber and porosity volume fractions	33
3.5.2 Fiber orientation distribution	34
3.5.3 Fiber length distribution	36
3.6 Discussion	37
3.7 Conclusion	41
4 DAMAGE INITIATION: MICRO-VOID NUCLEATION	45

	Page
4.1 Introduction	45
4.2 Methods	48
4.2.1 Experimental details	48
4.2.2 Simulation details	50
4.3 Results	55
4.3.1 The role of porosity manufacturing defects and the ductile frac- ture zone	55
4.3.2 Experimental micro-void nucleation during damage initiation . .	57
4.3.3 Simulated heterogeneous stresses and strains in the microstructure	57
4.4 Discussion	60
4.5 Conclusion	61
5 DAMAGE PROGRESSION: CRACK PROPAGATION	63
5.1 Introduction	63
5.2 Materials and Methods	67
5.2.1 Composite Material	67
5.2.2 Experimental Details	67
5.2.3 Experimental Post-Processing	71
5.2.4 Simulation Details	73
5.3 Results and Discussion	75
5.3.1 Interfacial Matrix Cracking	76
5.3.2 Conoidal Matrix Cracking	79
5.3.3 Fiber Breakage	80
5.4 Conclusion	84
6 CONCLUSIONS	87
REFERENCES	91
A ALGORITHM FOR DESTRUCTIVE OUT-OF-PLANE ANGLE ANALYSIS	99

LIST OF TABLES

Table	Page
3.1 Microstructural parameters computed using non-destructive and destructive techniques.	42

LIST OF FIGURES

Figure	Page
2.1 A flowchart showing the post-processing of 3D images in MATLAB, which sometimes requires the user to export their data to an external software for visualization and manual correction of automated segmentation results that incorrectly captured certain features, whereas ModLayer allows for direct visualization and free-hand drawing corrections of 3D stacked images within MATLAB (as shown by the sample images), providing a streamlined multi-class segmentation correction process that can yield accurate results for further quantification of segmented features.	7
2.2 The overall layout of ModLayer shown in (A), with the Colormap options including the additional 'jetwhite' Colormap shown in (B), as well as the image selection menu in (C) and the modify toggle button in (D).	9
2.3 Using ModLayer to visualize and investigate time lapse X-ray μ -CT images of a GFRP composite simultaneously at (A) the unloaded state and (B) the loaded state by scrolling, zooming, and panning through the linked time-resolved images. ModLayer was then used to mark the locations of damage by drawing around the regions of interest circled in (B), in order to impose a segmentation value of -1 to produce the classified image shown in (C) for damage quantification.	11
2.4 (A) Using ModLayer to improve automated segmentation conducted on X-ray μ -CT images (with axes shown in pixels and where 1 pixel = 1.3 μm) of a glass fiber reinforced polymer, where (B) shows an example of drawing directly on the μ -CT image to correct the segmentation of a pore, (C) shows drawing directly on the μ -CT image to correct under-segmented fibers, and (D) shows drawing directly on the segmented image to separate touching segmented fibers.	13
2.5 ModLayer was used to improve the automated segmentation conducted on (A) <i>in-situ</i> X-ray μ -CT images of an aluminum alloy undergoing fatigue crack growth, where (B) shows an example of the result of automated segmentation, and (C) shows the segmented image after corrections were conducted in ModLayer by drawing directly on the μ -CT image or on the multi-class segmentation, with locations of correcting over-detection of particles circled in (B) and (C).	17

Figure	Page
3.1 Comparing non-destructive X-ray μ -CT and typical destructive microscopy techniques for characterizing discontinuous fiber reinforced polymer matrix composites.	23
3.2 Schematic (A) showing the in-plane angle ϕ and the out-of-plane angle θ used to describe the 3D orientation of a fiber, and schematic (B) showing the elliptical cross-sections of three fibers, two of which have equal magnitude but opposite signs of θ	25
3.3 Progression of the surface after (A) rough polishing, (B) final polishing, (C) plasma etching, and (D) post-processing with elliptical fits around the cross- section of each fiber.	28
3.4 Schematic showing (A) the ambiguity of the out-of-plane angle θ , (B) successive polishing to determine the sign of θ , (C) the reference image with the two predicted centroid positions, and (D) the reference image and target image schematically overlaid to determine the sign of θ	30
3.5 (A) Overlay of optical micrographs showing the reference image (green) and target image (red), with arrows pointing from the centroid on the reference image to the centroid on the target image, as well as plots of the (B) A_{13} and the (C) A_{23} components of the A_{ij} tensor, showing the upper bound, the lower bound, and the true value determined through successive polishing and automatic image analysis. (For interpretation of the references to colour in this figure legend, the reader is referred to the Web version of this article.	32
3.6 The radial fiber orientation distribution averaged along equal area concentric annuli of the specimen for (A) A_{11} , (B) A_{22} , (C) A_{33} , (D) A_{12} , (E) A_{13} , and (F) A_{23} from both non-destructive and destructive characterization of the same fibers.	35
3.7 Comparison of the weight fiber length distributions determined non- destructively and destructively.	37
3.8 A sample of the of X-ray μ -CT images (A) which included the matching optical microscopy image plus and minus $26 \mu m$, the detected 3D porosity (B), the surface of the specimen achieved through polishing but before plasma etching of the matching region (C) as well as the 2D porosity detected from the optical micrograph (D).	39
3.9 An example of a curved fiber towards the flow direction, Z, in a tomography image (A) with its detected 3D morphology overlaid in (B).	40

Figure	Page
4.1 An overview of the <i>in-situ</i> study where (A) shows a sample 9 of the 1500 X-ray projected radiographs captured by the detector over 180°, (B) shows the <i>in-situ</i> loading set-up with the miniature load frame, (C) shows the view of the speckled specimen from the optical camera used for computing macroscopic strain, and (D) and (E) show the reconstructed tomography images at 0 load and at maximum load (just before fracture), respectively.	47
4.2 A schematic representation of the condensed data procedure, which converts 3D matrix data (high memory demand) to meta-data format, which reduces the file size by approximately 99%.	50
4.3 A schematic representation of using condensed fiber data to determine which fibers may contain artificial discontinuities.	51
4.4 The sequence of post-processing the reconstructed tomography images in (A) to achieve high fidelity feature detection shown in (B), which includes specimen edge detection, porosity manufacturing defect detection, and individual fiber detection in 3D, as well as the instantiated model (C), the 368 fibers within the model (D), and the manufacturing porosity defects within the model (E).	53
4.5 The procedure used to mesh the instantiated model where (A) shows a fiber in red, a porosity manufacturing defect in blue, and the matrix in grey, (B) shows the removed manufacturing pore, (C) and (D) show the voxels meshed using tetrahedral elements, and (E) shows a meshed fiber in the matrix.	54
4.6 Shown in (A) are the fibers detected within the gauge section of the specimen at 0 load where each fiber is individually detected and assigned a fiber ID, and where the green outline indicates the location of ductile fracture observed experimentally, which is also shown in the tomography images just before fracture in (B). Preexisting porosity, micro-void nucleation, and eventual void coalescence in the ductile fracture zone are shown in (C) at 0 load, (D) at 96% of failure, and (E) just before failure.	56
4.7 The fibers that interacted with the micro-void nucleation events (A) at the unloaded state with grey spheres at the locations of simulated matrix hydrostatic stress hot-spots, and (B) at 50% of the macroscopic failure strain with the experimentally determined micro-void nucleation shown in red, with (C) an overlay of a sample of the DVC ϵ_{zz} strain hot-spots. The coupled micro-void nucleation and early fiber breakage is shown in (D) and (E) at the unloaded state, and in (F) and (G) at 50% of the macroscopic failure strain.	58

Figure	Page	
4.8	An overview of the cropped simulation results (cropped to visualize away from the boundary conditions) of the specimen region shown in the tomography images of (A) which were post-processed for feature detection shown in (B). The heterogeneous strain in the loading direction (ϵ_{zz}) is shown in (C), the heterogeneous stress in the loading direction (σ_{zz}) is shown in (D), the heterogeneous hydrostatic stress (σ_{hyd}) of the matrix is shown in (E), and the agglomerations of matrix elements in the 99.997 th percentile of hydrostatic stress, with the fibers they interact with, are shown in (F).	59
5.1	An overview of the <i>in-situ</i> study where (A) shows the <i>in-situ</i> loading set-up with the miniature load frame, (B) shows a sample of the reconstructed tomography images, (C) shows the ductile fracture zone just before fracture, and (D) shows a sample of the fibers detected in the microstructure (cropped away from the edges by 340 μm radially).	68
5.2	An overview of the damage initiation events labeled 1 through 6 that occurred within the ductile fracture zone visualized at (A) the unloaded state, and at (B) $0.5\epsilon_f$, with a blue box indicating the region of interest for the damage propagation analysis, and with corresponding tomography images at each of the 6 locations, where sites labeled 1-5 were micro-void nucleation, and site 6 was early debonding.	69
5.3	An overview of the coupled experiment and simulation, where (A) is the region of interest for the damage propagation analysis at 0 load, (B) is the tracked region at $0.5\epsilon_f$ that contained sites of damage initiation which grew significantly and coalesced in (C) at $0.85\epsilon_f$. Simultaneously, (D) shows the simulation of the region of interest from $0.5\epsilon_f$ to $0.85\epsilon_f$, where the displacement boundary conditions match exactly the experimental results from (A) to (C). The detected fibers are shown in (E), and the voids present at $0.5\epsilon_f$ can be seen in (F), where the three largest voids are the sites of damage initiation.	70
5.4	The coupled simulation and experiment results, where (A) shows the simulation result with the 99 th percentile matrix shear stress (YZ) overlaid, (B) shows the coupled simulation and experiment at $0.5\epsilon_f$ with the simulated maximum principal stress overlaid, and (C) and (D) show the 3D experimental results at $0.75\epsilon_f$ and $0.85\epsilon_f$, respectively. A different view of the same data with intersecting oblique planes (in order to capture both events which do not occur in the same plane) is shown in (E), with the corresponding tomography images at those planes shown in (F), (G), and (H) at $0.5\epsilon_f$, $0.75\epsilon_f$, and $0.85\epsilon_f$, respectively, where the dashed box contains the region of high shear stress that did not lead to damage, and the dashed circle contains the region of high shear stress emanating from a micro-void which led to damage progression.	74

Figure	Page
5.5 The coupled simulation and experiment results, where (A) shows the simulation result with the 99 th percentile matrix hydrostatic stress overlaid, (B) shows the coupled simulation and experiment at $0.5\varepsilon_f$ with the simulated maximum principal stress overlaid, and (C) and (D) show the 3D experimental results at $0.75\varepsilon_f$ and $0.85\varepsilon_f$, respectively.	76
5.6 The coupled simulation and experiment results, where (A) shows the simulation result with the 99 th percentile matrix hydrostatic stress overlaid, (B) shows the coupled simulation and experiment at $0.5\varepsilon_f$ with the simulated maximum principal stress overlaid, and (C) and (D) show the 3D experimental results at $0.75\varepsilon_f$ and $0.85\varepsilon_f$, respectively. A view of the same data with an intersecting plane is shown in (E), with the corresponding tomography image at that plane shown in (F), (G), and (H) at $0.5\varepsilon_f$, $0.75\varepsilon_f$, and $0.85\varepsilon_f$, respectively.	77
5.7 Experimental data of the damaged in-plane (XY plane) fiber shown at (A) the unloaded state, (B) $0.5\varepsilon_f$, (C) $0.75\varepsilon_f$, and (D) $0.85\varepsilon_f$ where a longitudinal fiber breakage event has occurred, as well as an image of the simulated fiber experiencing a high shear stress gradient in its plane (XY plane).	82
5.8 The experimental data rendered at the unloaded configuration of an in-plane fiber (A) which was damaged during the injection molding process as can be seen circled, with accompanying tomography images sectioned at the five planes described in (B), where it can be seen circled in Slices 1, 2, and 5 that neighboring fibers appeared to have applied force during injection molding leading to damage in the fiber at the unloaded state. . .	83
A.1 Reference and target fiber matching algorithm outline.	99

ABSTRACT

Hanhan, Imad Ph.D., Purdue University, May 2020. Investigating Damage in Discontinuous Fiber Composites through Coupled *in-situ* X-ray Tomography Experiments and Simulations. Major Professor: Michael D. Sangid.

Composite materials have become widely used in engineering applications, in order to reduce the overall weight of structures while retaining their required strength. Due to their light weight, relatively high stiffness properties, and formability into complex shapes, discontinuous fiber composites are advantageous for producing small and medium size components. However, qualifying their mechanical properties can be expensive, and therefore there is a need to improve predictive capabilities to help reduce the overall cost of large scale testing. To address this challenge, a composite material consisting of discontinuous glass fibers in a polypropylene matrix is studied at the microstructural level through coupled experiments and simulations, in order to uncover the mechanisms that cause microvoids to initiate and progress, as well as certain fiber breakage events to occur, during macroscopic tension. Specifically, this work coupled *in-situ* X-ray micro computed tomography (μ -CT) experiments with a finite element simulation of the exact microstructure to enable a 3D study that tracked damage initiation and propagation, and computed the local stresses and strains in the microstructure. In order to have a comprehensive 3D understanding of the evolution of the microstructure, high fidelity characterization procedures were developed and applied to the μ -CT images in order to understand the exact morphology of the microstructure. To aid in this process, ModLayer - an interactive image processing tool - was created as a MATLAB[®] executable, and the 3D microstructural feature detection techniques were compared to traditional destructive optical microscopy techniques. For damage initiation, this work showed how high hydrostatic stresses in the matrix can be used as a metric to explain and predict the

exact locations of microvoid nucleation within the composite's microstructure. From a damage propagation standpoint, matrix cracking - a mechanism that has been notably difficult to predict because of its apparent stochastic nature - was studied during damage propagation. The analysis revealed the role of shear stress in fiber mediated flat matrix cracking, and the role of hydrostatic stress in fiber-avoidance conoidal matrix cracking. Overall, a sub-fiber simulation and an *in-situ* experimental analysis provided the microstructural physical phenomena that govern certain damage initiation and progression mechanisms, further enabling the strength and failure predictions of short fiber thermoplastic composites.

1. INTRODUCTION

1.1 Background

Structural materials have played a pivotal role in human history, dating back thousands of years. Notably, the Maltese Megalithic Temples are arguably the oldest freestanding structures ever created by humans, and date back to the mid-third millennia BC [1]. Located in the Maltese Islands, these temples are made completely out of Globigerina Limestone and Coralline Limestone, and represent some of the most complex ancient stone structures in the world [1]. Just a few hundred years after the first human structure was built, composite materials were created.

Around 3000 BC in the Middle East, humans mixed clay and mud with chopped straw, and the first structural composite materials were invented [2]. Even laminate composites made their first appearance around the same time, dating as far back as 2750 BC to an iron laminate composite in the Great Pyramid in Gizeh [3]. Five thousand years later, advanced composites can be found in structures more complex than our early human ancestors could have ever imagined.

Specifically, fiber reinforced organic polymer matrix composites have reshaped the modern aerospace industry. In these composites, the matrix material is typically either a thermoplastic or a thermoset polymer, while the fibers are usually either carbon or glass. Certain combinations offer different advantages based on the mechanical performance requirements. For example, a thermoplastic matrix offers more ductility (a higher strain to failure), while a thermoset matrix offers a higher strength, but is typically more brittle [4]. A laminate composite with a thermoset epoxy matrix and continuous carbon fibers offers one of the the highest strength configurations, and can be found in the skins of aircraft wings as well as the fuselage of aircraft.

Composite materials were introduced onto aircraft structures because one of the most critical motivators in the aerospace industry, if not the most critical, is the desire to reduce the weight of a structure while retaining its required strength [5]. Consider the Boeing 787, which was designed with 50% advanced composites in the overall structure [6]. This resulted in weight savings which, just in the first 7 years of service, saved \$10 billion in fuel costs in the entire fleet [7]. Even more importantly is the environmental impact of this reduction of fuel, which reduces exhaust emissions. For example, the use of composites in the Boeing 787 helped save 18 billion pounds of fuel in the same 7 year period [7].

While composites can offer many weight saving advantages (and can even offer reduced scheduled maintenance), they have been implemented mainly for critical and relatively large components [6]. This is because the cost of manufacturing and qualifying composite components can be very expensive. Therefore, composites are very appealing for relatively larger critical components (which save a large amount of weight), but less appealing for small secondary components (which yield smaller weight savings); the opportunity to save additional weight exists, but is currently too expensive due to the high cost of manufacturing and qualifying composites.

This is where discontinuous fiber composites offer an advantage: they can be manufactured into complicated 3D geometries at a much lower cost. Additionally, while their strength is lower, their strain to failure is higher, providing a higher level of ductility and reducing the likelihood of catastrophic failure. These properties make them ideal for small and secondary components in aircraft structures, like brackets and clips. However, despite the lower cost of manufacturing, the cost of qualifying and validating their strength properties can still be equally as expensive as other composites, requiring large scale component-level testing.

Therefore, there is a need to also lower the cost of qualifying short fiber composite materials. This does not imply eliminating large scale component-level tests; instead, this implies that engineers could conduct less component-level testing if tools and methods exist which offer high accuracy predictions of mechanical strength. Develop-

ing such methods would empower engineers to utilize computing power to supplement experimental mechanical testing, and reduce the overall cost of qualification.

To address this challenge, this work comprehensively analyzed a short fiber composite material through experimental techniques (both destructive and non-destructive techniques), as well as sub-fiber 3D simulations of the microstructure, with the goal of increasing predictive capabilities of the non-linear mechanical behavior of short fiber composites. Specifically, the composite material was an injection molded polypropylene thermoplastic reinforced with E-glass fibers that (1) were 10 μm in diameter, (2) were pre-treated with a tailored silane solution (to promote adhesion with the polymer matrix), and (3) exhibited varying lengths and orientations in the finished part due to the injection molding process.

The material was injection molded to a cylindrical rod geometry, which was manufactured by DuPont, measuring approximately 1.27 cm (0.5 inch) in diameter and approximately 45.72 cm (1.5 feet) in length, where the flow direction was in the length direction of the rod. The final composite rod was then machined into three dog-bone shaped specimens with a gauge section diameter of approximately 2.4 mm . The first two specimens were used to quantify and compare characterization techniques. The third specimen was experimentally loaded in tension during an *in-situ* X-ray micro-computed tomography experiment, which was conducted at Argonne National Laboratory, beam-line 2-BM-A. The experiment successfully tracked each individual microstructural feature present in the tomography images as the specimen was loaded, and employed a coupled simulation of a virtual microstructure matching the exact experimental conditions.

In order to track all the microstructural features, they first had to be accurately detected from the acquired tomography images. This alone was a major challenge because of the complex 3D morphology of the fibers and pores, which exhibit varying intensity ranges within the images. Therefore, this work addressed these challenges by first developing an image processing tool, called ModLayer, that allows engineers and researchers to verify and correct feature detection in 3D images, discussed in

Chapter 2. Next, this work compared the detection capabilities of destructive optical microscopy (an historic method of characterization) with non-destructive X-ray tomography (a relatively newer technique), which is discussed in Chapter 3, increasing the confidence of the microstructural detection capabilities developed in this work.

The detected 3D features from *in-situ* X-ray tomography images were then used in a coupled experiment and simulation analysis to explore the fundamental mechanisms which govern micro-void nucleation during damage initiation, discussed in Chapter 4. Lastly, the physical phenomenon that drives propagation of these micro-voids in the form of interfacial matrix cracking and conoidal matrix cracking is explained and described in Chapter 5 through another coupled experiment and simulation analysis. Each chapter will contain a thorough introduction (with a corresponding literature review), methodology, and detailed conclusions. At the end of the dissertation, a broad conclusion will be provided. Overall, the results of this work provide a comprehensive understanding of the physics governing the initiation and propagation of damage within the complex and heterogeneous microstructures of short fiber reinforced thermoplastics, increasing the understanding of the non-linear micromechanical response and propelling engineers towards strength and failure predictions of short fiber composites.

1.2 Research Contributions

The four major research contributions of this PhD are:

1. Image processing: a tool called ModLayer was created and published as an open source interactive graphical user interface that removes the burden of import/export redundancies when interacting with 3D data in MATLAB during visualization, modification, or segmentation through manual drawing across image stacks. Overall, this tool is especially useful to engineers and researchers interested in correcting - within MATLAB — automated segmentation of noisy

3D images which can yield erroneous microstructural features in segmentation procedures.

2. Microstructural characterization: high fidelity detection and characterization techniques (non-destructive and destructive), including a novel approach for automatically determining the sign of the out-of-plane angles for thousands of fibers at once, were developed and compared. The differences in the detection capabilities of non-destructive X-ray tomography and destructive optical microscopy were quantified, shedding light on the specific advantages and disadvantages of each approach, and enabling engineers to quantify uncertainty in their microstructural characterization measurements especially as they relate to model based structural integrity activities.
3. Damage initiation: a coupled experiment and simulation were used to uncover the mechanisms that cause damage to initiate in the microstructure under macroscopic tension. Specifically, it was found that high hydrostatic stresses in the matrix can be used as a metric to explain and predict the exact location of micro-void nucleation that occurs during damage initiation within the composite's microstructure. Furthermore, this work provided evidence that hydrostatic stresses in the matrix can lead to coupled micro-void nucleation and early fiber breakage, and that small fragments of fibers can play an important role in the process of micro-void nucleation.
4. Damage propagation: a coupled experiment and simulation were used to uncover the mechanisms that cause damage to propagate in the microstructure under macroscopic tension. This work determined the role of shear stress in interfacial matrix cracking, the role of hydrostatic stress in conoidal matrix cracking, and the role of environmental damage in longitudinal fiber breakage. In doing so, this work enabled more accurate predictions of non-linear damage propagation behavior of thermoplastic fiber composites.

2. TOMOGRAPHY IMAGE PROCESSING

A version of this chapter was previously published by *Integrating Materials and Manufacturing Innovation* and is reproduced with copyright permission through license number 4763690664434. Imad Hanhan and Michael D. Sangid. ModLayer: A MATLAB GUI Drawing Segmentation Tool for Visualizing and Classifying 3D Data. *Integrating Materials and Manufacturing Innovation*, (0123456789), 11 2019. DOI: 10.1007/s40192-019-00160-5.

2.1 Introduction

Modern characterization techniques are able to yield robust 3D images of materials and their microstructures, providing engineers and scientists powerful capabilities in understanding the behavior of materials [8,9]. One requirement of most techniques is digital image processing, which is the process of either enhancing the images for visual observation, or segmenting and classifying features for measurement or statistical analysis [10]. Segmentation is a specific type of data processing and is defined as the separation of an image with intensity domain I into non-intersecting subsets. This can prove to be challenging, especially for 3D images [11]. In fact, selecting the appropriate segmentation technique in itself is usually a complex problem [12]. To combat the difficulties experienced in segmentation, which is typically considered the most critical step in image processing, a number of higher accuracy segmentation tools have been developed [13].

MATLAB is often used in these segmentation processes because of its user friendly matrix operation capabilities, as well as its robust image processing toolbox [14]. These capabilities are exemplified by MIPARTM, a MATLAB based software package used to align, pre-process, segment, visualize, and quantify 3D images [13]. MIPAR offers an automated segmentation module that allows the user to determine the optimum parameters for automated binary segmentation of 3D images, which can be con-

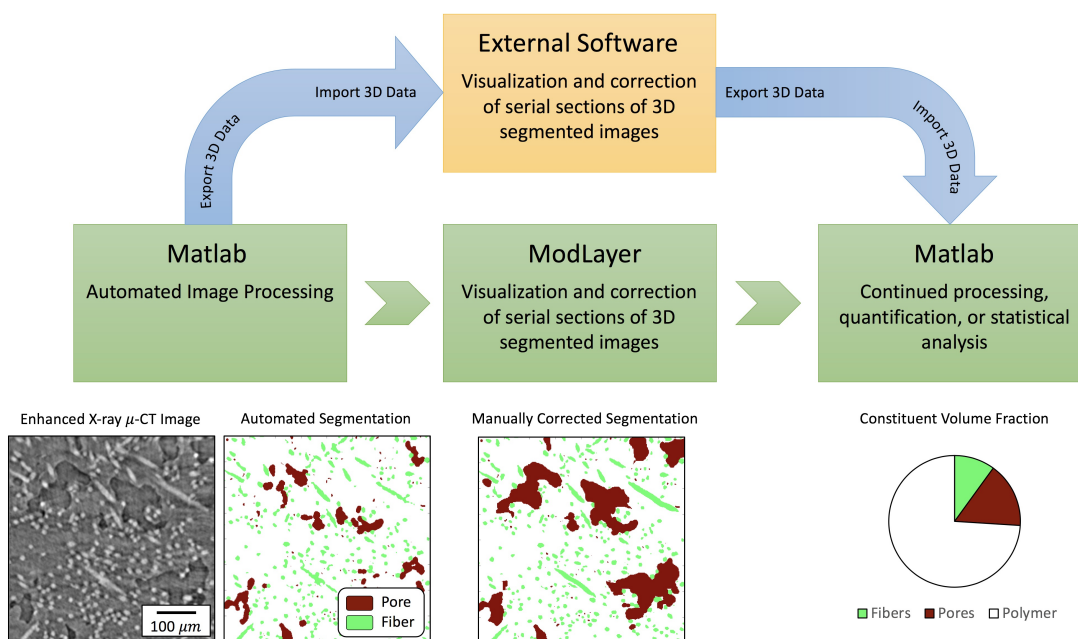


Figure 2.1. A flowchart showing the post-processing of 3D images in MATLAB, which sometimes requires the user to export their data to an external software for visualization and manual correction of automated segmentation results that incorrectly captured certain features, whereas ModLayer allows for direct visualization and free-hand drawing corrections of 3D stacked images within MATLAB (as shown by the sample images), providing a streamlined multi-class segmentation correction process that can yield accurate results for further quantification of segmented features.

ducted on different features within an image and stored as layers in multi-dimensional space (instead of a multi-class segmentation dataset). However, despite optimum segmentation parameters, certain imaging techniques - like X-ray micro-computed tomography (μ -CT) - contain stochastic fluctuations in image intensities which can still result in erroneous automated segmentation results. Even when coupled with trainable machine learning, automated multi-class segmentation procedures cannot always correctly segment every feature of interest and its exact edge [15]. Therefore, there remains a need to simultaneously view serial sections of 3D images, and apply manual modifications to multi-class 3D segmentation data. In MATLAB, this poses a challenge because there is no straightforward open-source method to visualize two sets of linked 3D images, and apply modifications through freehand drawing to multi-class datasets. To do so, the user would typically export their 3D data to external software with these capabilities [16], and re-import their 3D data back into MATLAB to continue their quantification analysis, as shown in Figure 2.1.

To alleviate this issue, ModLayer, a user-friendly, open source, and easily implemented MATLAB graphical user interface (GUI), was created to allow the user to view and simultaneously scroll, zoom, and pan through linked sets of stacked images (typically the raw 3D image and its multi-class segmentation). Additionally, ModLayer allows the user to apply modifications to 3D images in order to classify features of interest, or correct segmentation results for cases of under- or over-detection, incorrect segmentation, and/or incorrectly touching edges of segmented features, through interactive freehand drawing.

This paper will first describe the general function and GUI, then provide three case studies to show the functionality of ModLayer by (1) classifying regions of damage with *in-situ* time lapse X-ray μ -CT of a glass fiber reinforced polypropylene (GFRP), (2) correcting multi-class segmentation errors in segmented X-ray μ -CT images of a GFRP composite, and (3) capturing features of interest within *in-situ* 3D X-ray μ -CT images during fatigue crack growth experiments of aluminum 7050. For the first case study, an explanation is provided outlining the importance of image clas-

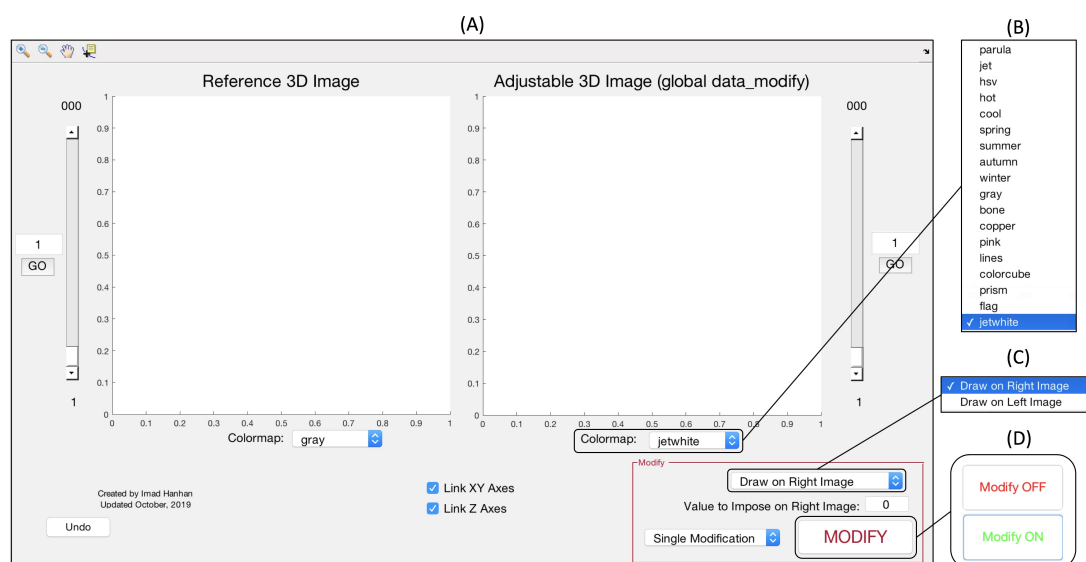


Figure 2.2. The overall layout of ModLayer shown in (A), with the Colormap options including the additional 'jetwhite' Colormap shown in (B), as well as the image selection menu in (C) and the modify toggle button in (D).

sification for time lapse μ -CT, followed by an example using ModLayer to identify regions of damage found within time-resolved images. For the last two case studies, a brief background of the importance of image segmentation for the particular application is provided, an explanation of an automated segmentation procedure is given, and examples are provided in each case showing the use of ModLayer in correcting segmentation inaccuracies.

2.2 Methods

ModLayer, which is freely available for download as part of this publication, is written as a GUI function in MATLAB that requires two inputs: the reference 3D image and the adjustable 3D image. The first input, the reference 3D image, is entered during the execution of the ModLayer function. The second input, the adjustable 3D image, is imported into ModLayer as a global variable. Therefore, the adjustable 3D image must be instantiated within the Workspace as a global variable called ‘data_modify’ prior to the execution of the function ModLayer. The use of the global variable (1) is a safety feature which ensures that in the event ModLayer is accidentally closed, manual modifications remain in the Workspace and are not lost, and (2) allows for real-time observations, within ModLayer, to bulk changes made to the adjustable 3D image in the MATLAB Workspace, such as feature dilation or erosion.

With both the reference 3D image and the adjustable 3D image (imported in the form of the global variable ‘data_modify’) visible in ModLayer, a Colormap that is best suited for viewing each of the data sets can be selected, as shown in Figure 2.2A and 2.2B. The Colormap options include all the default MATLAB Colormaps, as well as an additional Colormap called ‘jetwhite’, which can make certain multi-class segmentation visualizations easier to observe. The images may also be linked in the XY and Z which couples the scrolling, panning, and zooming of the reference and adjustable images. The linked 3D images can be observed for time lapse activity,

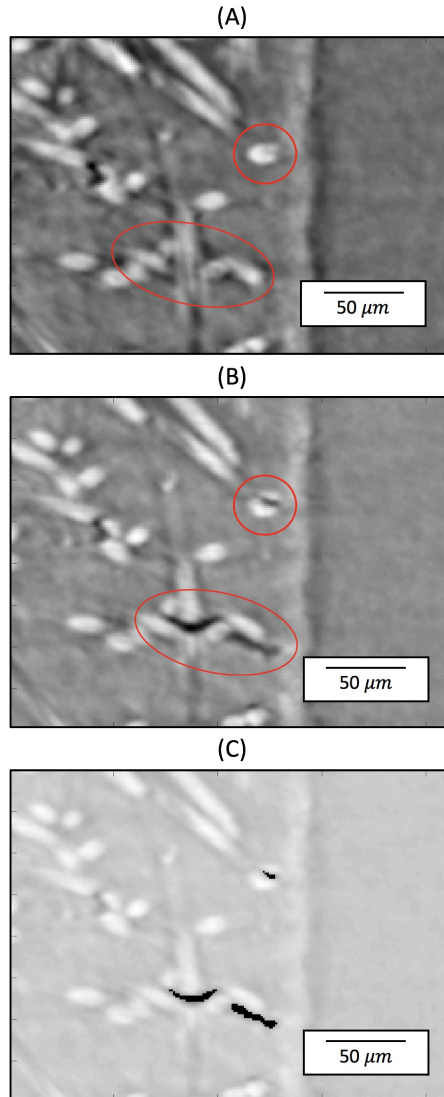


Figure 2.3. Using ModLayer to visualize and investigate time lapse X-ray μ -CT images of a GFRP composite simultaneously at (A) the unloaded state and (B) the loaded state by scrolling, zooming, and panning through the linked time-resolved images. ModLayer was then used to mark the locations of damage by drawing around the regions of interest circled in (B), in order to impose a segmentation value of -1 to produce the classified image shown in (C) for damage quantification.

or multi-class segmentation, in each layer by either using the scroll bars next to the images, or by typing the desired layer number and pressing ‘GO’.

If a region of interest or low accuracy segmentation is found, a manual modification to the adjustable 3D image can be conducted within ModLayer. Prior to applying a modification, a drop-down menu allows for the selection of freehand drawing on the left reference image (which is useful especially for under-detection corrections) or on the right adjustable image (which is useful especially for correcting over-detection or separating touching edges), as shown in Figure 2.2C. The user can input any multi-class segmentation value they wish to impose on the adjustable 3D image, and press the modify button to make modifications. The user can then click and drag to freehand draw on the selected image, and when the click is released, the change is immediately applied to the selected layer of the adjustable 3D image which is also immediately saved to the MATLAB Workspace.

2.3 Visualizing and Classifying 3D Data Using ModLayer

2.3.1 Identifying damage in 3D time lapse images

The first case study to show the functionality of ModLayer was time lapse sequences of 3D X-ray μ -CT images of a GFRP composite under tensile load. Time lapse CT, in general, can be useful in understanding the evolution of certain materials or structures as damage accumulates under external loading conditions [17, 18]. Usually, the analysis of time lapse 3D images requires image processing and classification to segment locations of damage and identify types of damage within the 3D images [19–21].

To show how ModLayer can be used to identify locations of activity in time lapse 3D images, the microstructure of a discontinuous GFRP (30% by weight glass fiber) was imaged using synchrotron X-ray μ -CT [15]. The 3D images were examined for signs of damage, which appear as dark pixels at the loaded state (4% strain) which were not present at the unloaded state. To visualize and locate these regions of damage, the 3D X-ray μ -CT images were normalized so that $0 \leq I \leq 1$, and were inputted into ModLayer so the unloaded state was the reference (Figure 2.3A) and the loaded

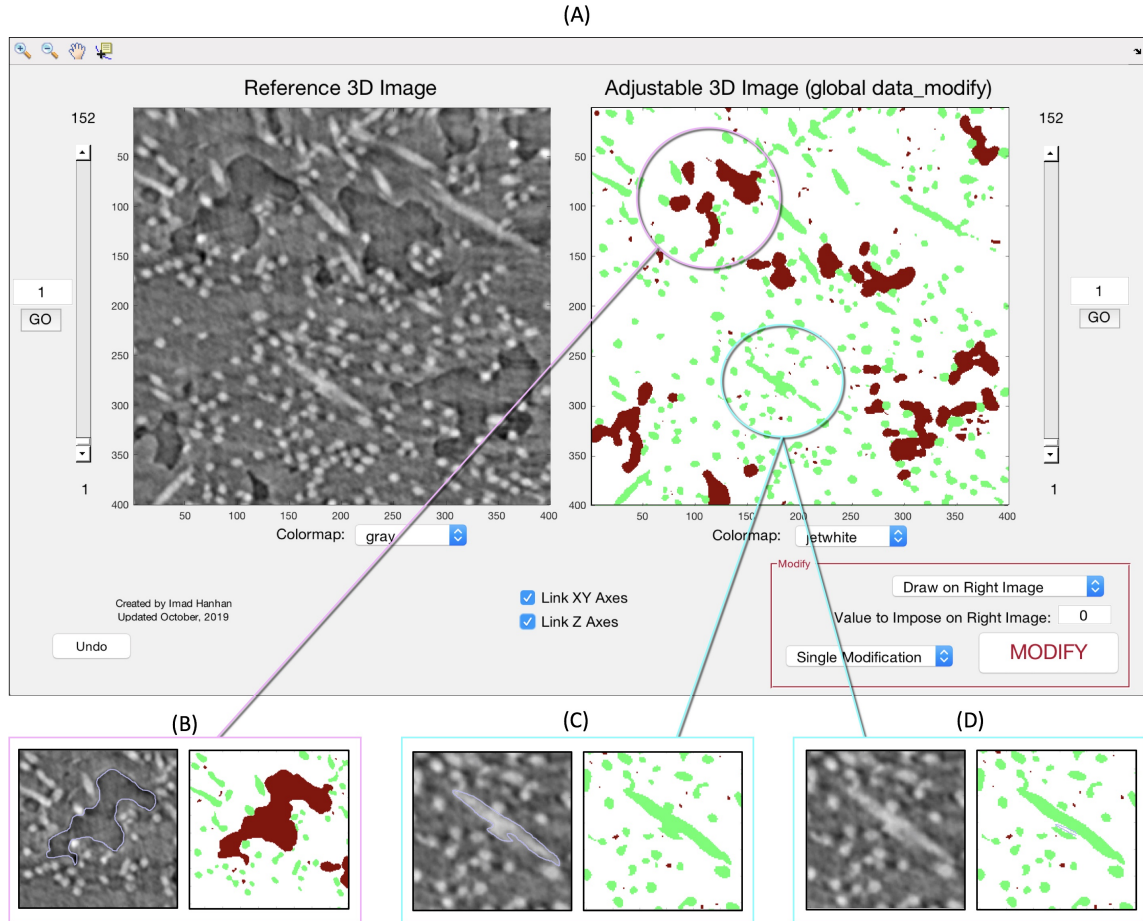


Figure 2.4. (A) Using ModLayer to improve automated segmentation conducted on X-ray μ -CT images (with axes shown in pixels and where 1 pixel = $1.3 \mu\text{m}$) of a glass fiber reinforced polymer, where (B) shows an example of drawing directly on the μ -CT image to correct the segmentation of a pore, (C) shows drawing directly on the μ -CT image to correct under-segmented fibers, and (D) shows drawing directly on the segmented image to separate touching segmented fibers.

state was the adjustable 3D image (Figure 2.3B). The 3D images were simultaneously inspected by scrolling, zooming, and panning through the linked stacked images and examined for regions of damage activity. When regions of damage activity were found in the image at the loaded state, like those circled in Figure 2.3B, ModLayer was used to draw directly on the image and impose a segmentation value of -1 (a value outside of the range of $0 \leq I \leq 1$) in order to classify regions of damage within the microstructure, as shown in Figure 2.3C. This shows that ModLayer can be used to examine and investigate linked time lapse 3D images directly in MATLAB without the need to open multiple windows or export to external software, while also providing the capability to classify locations of damage activity through freehand drawing for further quantification in MATLAB.

2.3.2 Correcting feature segmentation in tomography images of a composite material's microstructure

The second case study to show the functionality of ModLayer was to correct segmentation errors in X-ray μ -CT images of a fiber composite. In discontinuous fiber reinforced polymers, the full characterization of the microstructure, including the fiber volume fraction, porosity volume fraction, fiber length, and fiber orientation distributions, is important to not only qualify composite materials for use, but also predict their mechanical behavior [22–26]. Because the characterization of these microstructural features is sensitive to segmentation errors, researchers have worked to develop tools and techniques to conduct these characterizations with the highest possible fidelity and to minimize segmentation errors of microstructural features that could impact characterization or predictive capabilities [27–29]. However, despite these efforts, sometimes it can be very difficult - especially for characterizing porosity - to achieve high fidelity segmentation of every feature [15]. To show how ModLayer can be used to correct these occurrences, X-ray μ -CT images of a discontinuous GFRP (30% by weight) were analyzed [15].

The serial sections of the reference 3D image, as shown in Figure 2.4A, show high intensity pixels (white) at the locations of fibers, and low intensity pixels (black) at the locations of small pores and at the edges of large pores. An automated segmentation procedure was conducted in MATLAB to segment the image into values of 0 for the matrix, 1 for the fibers, and 2 for the pores. The procedure was as follows:

1. normalization so that $0 \leq I \leq 1$,
2. segmentation of fibers by $I > 0.65$,
3. segmentation of large pores by
 - (a) selection of pixels with $I < 0.33$,
 - (b) dilation using a spherical structural element with radius 4,
 - (c) adjustment to fill 3D holes,
 - (d) erosion using a spherical structural element with radius 5,
 - (e) removal of features with a volume smaller than 10,000 pixels, and
4. segmentation of small pores by $I < 0.25$.

The result of this automated procedure is shown in Figure 2.4A with the adjustable 3D image shown on the right, where it can be seen that small pores were detected well but large pores were generally under-detected.

ModLayer was then used to visualize the results of the segmentation analysis in each layer of the 3D images, and apply corrections to cases of low accuracy segmentation of porosity by drawing on the left reference image in Figure 2.4B (to capture the full pore) and imposing a value of 2 for the drawn region in the multi-class segmented image. Additionally, regions with fibers that were under-detected were corrected by drawing on the left reference image in Figure 2.4C and imposing a value of 1 for the drawn region in the multi-class segmented image. Lastly, regions with touching fiber edges were separated by drawing on the right segmented image in Figure 2.4D and

imposing a value of 0 between detected fibers in the multi-class segmented image. This shows that ModLayer can be used to visualize and improve the multi-class segmentation accuracy of the microstructural features of a composite material imaged through X-ray μ -CT, as was seen in Figure 2.4B-2.4D, especially for large pores which can be very difficult to capture through standard segmentation algorithms.

2.3.3 Correcting feature segmentation of *in-situ* AA7050 fatigue crack growth tomography images

To show another example of the functionality of ModLayer, segmented X-ray μ -CT images of an aluminum alloy acquired *in-situ* were improved to increase the accuracy of segmentation. Certain aluminum alloys, like AA7050, are known to have fatigue properties which can be severely impacted by intermetallic particles and voids [30]. Therefore, it is of interest to study the fatigue crack growth behavior within this alloy as the crack interacts with particles and voids [31]. Carter et al. noted that the noise levels and reconstruction artifacts in the X-ray μ -CT images posed many challenges in image segmentation, which is necessary in understanding the behavior of the crack in 3D. A sample of the tomography images acquired after 5651 cycles of fatigue loading on the specimen [31] is shown in Figure 2.5A, where the notch tip can be seen in the upper left corner. The particles are seen as high intensity white pixels, and the crack plane/voids are seen as dark gray pixels.

An automated segmentation procedure was conducted in MATLAB as follows:

1. normalization so that $0 \leq I \leq 1$,
2. segmentation of particles by $I > 0.7$,
3. segmentation of the notch by
 - (a) selection pixels with $0.44 < I < 0.57$,
 - (b) slice-by-slice 2D erosion with a disk structural element of radius 4,
 - (c) adjustment to fill holes,

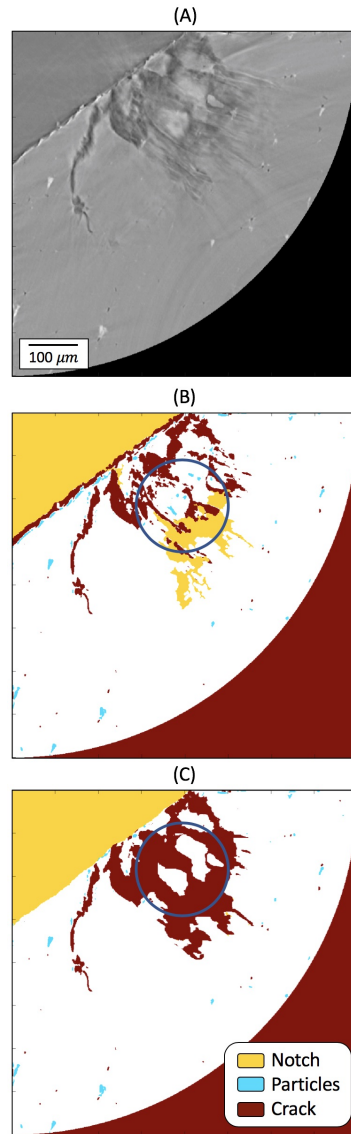


Figure 2.5. ModLayer was used to improve the automated segmentation conducted on (A) *in-situ* X-ray μ -CT images of an aluminum alloy undergoing fatigue crack growth, where (B) shows an example of the result of automated segmentation, and (C) shows the segmented image after corrections were conducted in ModLayer by drawing directly on the μ -CT image or on the multi-class segmentation, with locations of correcting over-detection of particles circled in (B) and (C).

- (d) removal of features with a volume smaller than 10,000 pixels,
 - (e) dilation with a disk structural element of radius 40, and
4. segmentation of the crack plane by $I < 0.49$.

It can be seen in the segmentation result (Figure 2.5B) that the notch was slightly under detected, and the sharp gradient near the edge of the notch caused some erroneous segmentation of particles as well as the crack plane. Additionally, it can be seen in Figure 2.5B that a portion of the crack plane had slightly higher intensity values and was therefore incorrectly segmented as part of the notch. Lastly, regions near the edge of the crack plane circled in Figure 2.5B and Figure 2.5C, had locations of particle over-detection. Therefore, ModLayer was used to draw on either the X-ray μ -CT image or the multi-class segmented image to correct the notch segmentation, increase the accuracy of the crack plane segmentation, and remove areas of erroneous crack and particle detection by imposing a value of 0 on the segmented image. The final multi-class segmentation after corrections conducted in ModLayer can be seen in Figure 2.5C, and shows that ModLayer can be used to increase the accuracy of the automated segmentation shown in Figure 2.5B for a more accurate analysis of the interaction of the crack plane with its neighboring microstructural features.

2.4 Conclusion

A tool was created within MATLAB that provides the capability of viewing successive slices of a reference 3D image and an adjustable 3D image. The tool, ModLayer, was created to also manually modify the adjustable 3D image - through an interactive freehand drawing GUI - in order to classify features that are either of interest, or correct the classification of features too difficult to segment automatically. ModLayer allows the user to select Colormaps that best display the images, while allowing the user to scroll, zoom, and pan through linked serial sections of the reference and adjustable 3D images. By clicking ‘Modify’, the user can draw directly on either of the two images to classify features or correct segmentation errors in the form of

under- or over-detection, incorrect segmentation, and/or incorrectly touching edges of segmented features. This tool is especially useful in correcting the multi-class segmentation of features that may arise from noise or erroneous artifacts in imaging techniques which are often too difficult to capture through standard automatic segmentation procedures. The utility of ModLayer was shown through its ability to classify regions of damage in time lapse 3D X-ray μ -CT images of a fiber reinforced polymer matrix composite, correct automated segmentation of porosity features, and separate touching segmented fiber regions. Additionally, it was shown to be useful in correcting automated segmentation errors of the notch, the particles, and the crack plane in a fatigue cracked AA7050 specimen captured through *in-situ* X-ray μ -CT. ModLayer is distributed as an open source MATLAB function freely available for download at <http://www.github.com/imadhanhan/ModLayer>.

3. NON-DESTRUCTIVE AND DESTRUCTIVE ANALYSIS

A version of this chapter was previously published by *Composites Science and Technology* and is reproduced with copyright permission through the Creative Commons license CC-BY-NC-ND. Imad Hanhan, Ronald Agyei, Xianghui Xiao, and Michael D. Sangid. Comparing non-destructive 3D X-ray computed tomography with destructive optical microscopy for microstructural characterization of fiber reinforced composites. *Composites Science and Technology*, 184:107843, 11 2019. DOI: 10.1016/j.compscitech.2019.107843.

3.1 Introduction

Short fiber reinforced polymers have gained attention in engineering applications due to their low-cost manufacturability and their ability to be easily fabricated into complex geometries. Since the features of the microstructure largely depend on the injection molding processing parameters, different geometries of injection molded composites can result in vastly different microstructures [32–35]. Often times, qualifying composite materials and predicting their bulk mechanical behavior requires a thorough characterization of their microstructural features including the fiber length and orientation distributions and the gas-phase pores [36–42]. Researchers have therefore developed a number of characterization techniques that can capture the microstructural details of discontinuous fiber composites, most of which are destructive in nature to the part or sample.

Specifically, techniques to measure the fiber orientation distributions in composites have historically been destructive, and include sectioning and polishing, followed by optical microscopy or scanning electron microscopy (SEM), in order to determine the in-plane and out-of-plane angles of the projected fibers from the surface characterization [22–26, 43]. Techniques to measure the fiber length distributions are also

typically destructive and involve heating the specimen to decompose the polymer matrix and down-selecting the fibers using an epoxy plug, in an effort to reduce bias in the measurement based on the potential for fiber breakage due to the release of stored strain energy during the matrix burn-off and fiber separation process. The extracted fibers are then suspended in a liquid such as water or glycerin, poured into a petri dish, and observed in an optical microscope in order to measure the fiber lengths [26, 44–47].

There are some challenges and limitations to these destructive techniques. A widely recognized challenge with sectioning and polishing specimens for fiber orientation analysis is the ambiguity in the 3D fiber orientation [27, 43, 48]. One way to resolve this issue is to determine the ambiguous angle by observing the shadow of each fiber that is exposed during plasma etching of the surface and then viewed in an optical microscope [43]. Another approach is to cut consecutive parallel sections from the composite [49], or successively polish the surface [50], followed by optical microscopy and observation of each fiber. The challenge with these approaches is that they are difficult to implement over a large area for thousands of fibers, which presents issues in characterization over a representative area/volume of the material or capturing gradient behavior in the orientation distribution spatially over a component.

Non-destructive techniques for characterizing the microstructure of composites have also been developed. One technique, known as scanning acoustic microscopy, uses interference fringes that result from echoes reflected by the fibers to conduct non-destructive fiber orientation measurements to depths of approximately $12\ \mu m$ [48]. However, this technique is limited by the fact that only fibers with out-of-plane angles less than 71.92° can be measured, and measurements deeper than $12\ \mu m$ require cutting the material [48]. Other techniques for non-destructive evaluation of composites that have become more popular in recent years involve X-ray radiation. Most commonly, high resolution X-ray micro computed tomography (μ -CT) can be used to non-destructively characterize a composite material’s microstructural features [8, 28, 51–57]. To understand the quantitative differences in microstructural char-

acterization achieved through non-destructive techniques, researchers have started to explore how fiber orientation distributions achieved through classical destructive optical microscopy differ from those achieved through μ -CT images using a Mean Intercept Length (MIL) technique. A MIL fiber tensor can be constructed to provide a global characterization of the general fiber alignment, but is not capable of capturing each single fiber [58]. Therefore, there remains a need to conduct a one-to-one feature comparison which comprehensively addresses all the microstructural and defect features.

This work addresses porosity and fiber volume fraction, fiber orientation, and fiber length distributions computed using μ -CT and optical microscopy as outlined in Figure 3.1. This paper will initially discuss the discontinuous fiber composite selected for analysis in this study and next provide detailed methodologies for the characterization methods to determine the porosity volume fraction, fiber volume fraction, fiber orientation, and fiber length distributions, first using μ -CT and then using optical microscopy. Furthermore, the ambiguity in the 3D fiber orientation measurements using destructive optical microscopy was resolved by successive polishing, plasma etching, and post-processed with the introduction of a new automated image processing algorithm, and the details of the algorithm are discussed. Overall, the results of this work provide a practical and useful comparative analysis between non-destructive μ -CT and destructive optical microscopy which comprehensively addresses all aspects of the microstructure.

3.2 Materials and Methods

3.2.1 Composite Material

The material used in this work was a short glass fiber reinforced polypropylene containing 30%, by weight, 10 μm diameter E-glass fibers (corresponding to a fiber volume fraction of 13.7%) manufactured using injection molding by DuPont into a cylindrical rod measuring approximately 1.27 *cm* (0.5 inch) in diameter and approx-

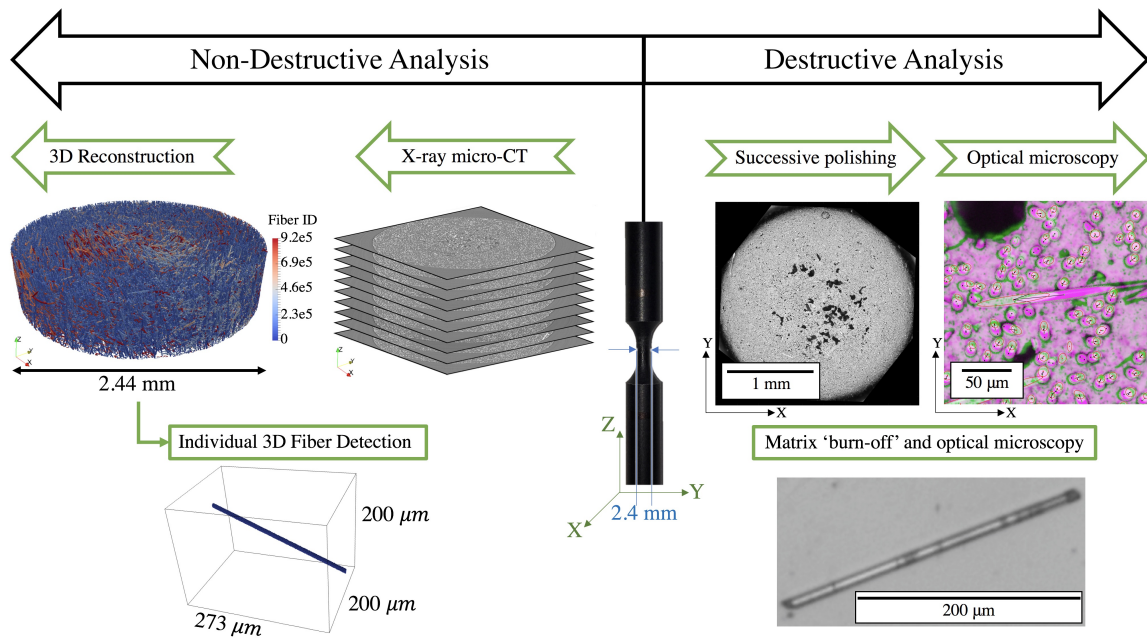


Figure 3.1. Comparing non-destructive X-ray μ -CT and typical destructive microscopy techniques for characterizing discontinuous fiber reinforced polymer matrix composites.

imately 45.72 *cm* (1.5 feet) in length, where the flow direction was in the length direction of the rod (Z axis). The final composite rod was then machined into dog-bone shaped specimens with a gauge section diameter of approximately 2.4 *mm*. One specimen was selected and imaged using μ -CT and then sectioned and polished for optical microscopy for a direct comparison of the fiber volume fraction, porosity volume fraction, and fiber orientation distribution, and a second specimen was selected for destructive characterization to provide a statistical comparison of the fiber length distribution.

3.2.2 Defining Fiber Orientation

The orientation of a fiber in 3D space, shown in Figure 3.2, can be characterized by two angles, an in-plane angle ϕ , and an out-of-plane angle θ [59,60]. It is standard to report the orientation of fibers, especially for discontinuous fibers, in the A_{ij} tensor form [59,60], where the components of the p vector are given by

$$\begin{aligned} p_1 &= \sin \theta \cos \phi \\ p_2 &= \sin \theta \sin \phi \\ p_3 &= \cos \theta \end{aligned} \tag{3.1}$$

and where A_{ij} is defined as

$$\begin{aligned} A_{ij} &= p_i p_j \\ &= \begin{bmatrix} \sin^2(\theta) \cos^2(\phi) & \sin^2(\theta) \cos(\phi) \sin(\phi) & \sin(\theta) \cos(\theta) \cos(\phi) \\ \sin^2(\theta) \cos(\phi) \sin(\phi) & \sin^2(\theta) \sin^2(\phi) & \sin(\theta) \cos(\theta) \sin(\phi) \\ \sin(\theta) \cos(\theta) \cos(\phi) & \sin(\theta) \cos(\theta) \sin(\phi) & \cos^2(\theta) \end{bmatrix} \end{aligned} \tag{3.2}$$

In this work, the in-plane angle is defined as $-90^\circ \leq \phi \leq 90^\circ$ and the out-of-plane is defined as $-90^\circ \leq \theta \leq 90^\circ$. The 2D elliptical cross-section of a fiber, shown in Figure 3.2B, contains enough information to determine the magnitude of θ , as

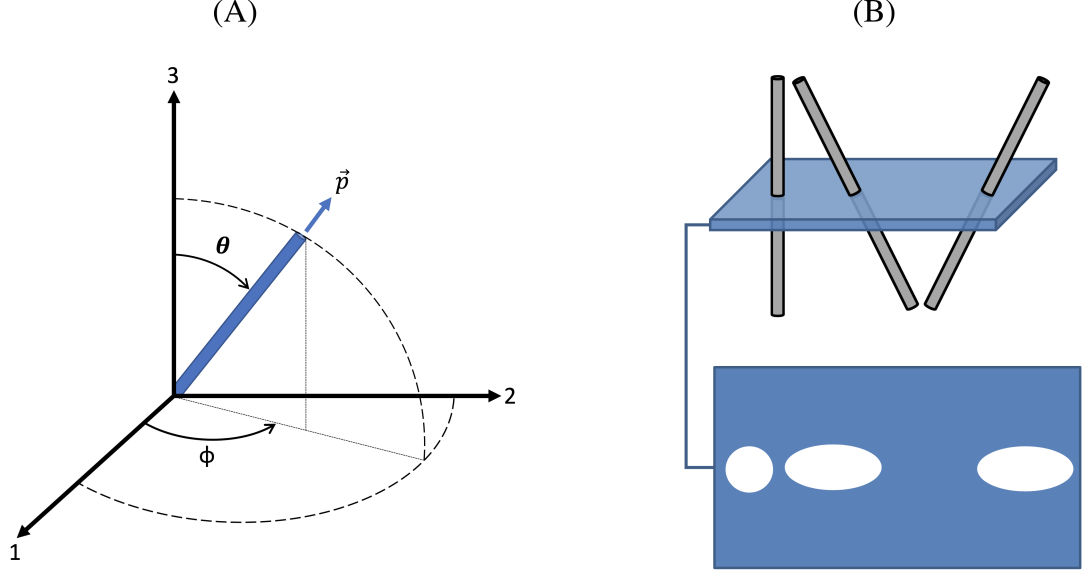


Figure 3.2. Schematic (A) showing the in-plane angle ϕ and the out-of-plane angle θ used to describe the 3D orientation of a fiber, and schematic (B) showing the elliptical cross-sections of three fibers, two of which have equal magnitude but opposite signs of θ .

well as the magnitude and sign of ϕ , resulting in A_{11} , A_{22} , A_{33} , and A_{12} . Since $\sin(\theta) \neq \sin(-\theta)$, additional 3D information is required to determine the sign of θ in order to resolve A_{13} and A_{23} , which each contain a $\sin(\theta)$ term [23, 25, 27]. In reporting the fiber orientation distributions, a theta correction was not applied since neither approaches were used here to estimate the volumetric quantity, but instead were compared directly [25].

3.3 Non-destructive X-ray μ -CT and Feature Detection

The selected specimen was studied at Argonne National Laboratory using synchrotron X-ray μ -CT, which offers significant advantages over lab-scale μ -CT analysis, specifically fast data acquisition, on the order of minutes using synchrotron X-rays, compared to hours for lab-based X-ray sources. Prior to imaging, an aluminum fidu-

cial marker was adhered to the center of the specimen's gauge section. An X-ray energy of 25 *keV* was used to scan the 2.44 *mm* diameter specimen, which was placed at a specimen to detector distance of 75 *mm*. Each X-ray projection was acquired with a 100 *ms* exposure time every 0.12° as the specimen was rotated at 0.5°/s within a range of 180°. The 1500 acquired X-ray projections were reconstructed using TomoPy [61], resulting in 2D images which stack to form a 3D image with dimensions 2560 x 2560 x 1240 pixels and a pixel size of 1.3 μm , as can be seen in the sample images in Figure 3.1. From the 3D image stack, the fibers and gas-phase pores can be observed visually but require rigorous image processing and segmentation to extract meaningful, quantifiable data across a large volume. The fiber volume fraction was determined by extracting the high intensity pixels corresponding to fibers. The porosity volume fraction was more complex to determine because large pores contain a combination of low and high intensity pixels in their interior and this gradient causes difficulties in detection and segmentation. To overcome this, a combination of Weka segmentation, a machine learning tool [62], combined with image processing in MATLAB® (binarization of pixels with intensity less than 17200, followed by erosion and dilation using a spherical structural element with a radius of 2 pixels) were used to create high fidelity 3D porosity reconstructions and compute the porosity volume fraction.

In order to determine fiber orientation and length distributions, a post-processing algorithm developed by Agyei and Sangid was employed, which combines 2D and 3D approaches to provide a complete 3D reconstruction of the fiber microstructure [28]. This allows for quantifying both the 3D fiber orientation distribution and the fiber length distribution in the same analysis. Please see [28] for additional details which are briefly summarized here for completeness. The algorithm initially processes each 2D image by iteratively enhancing the contrast, segmenting the image, and fitting ellipses around the fiber elliptical cross-sections present in each 2D μ -CT image. Then, this ellipse data is stacked and organized in 3D, and undergoes a number of 3D segmentation steps to determine which ellipses stack to form each individual fiber and

correct for errors in the 3D crude fiber architecture that are present due to random intensity fluctuations in the grayscale μ -CT images or imprecise segmentation. All components of the fiber orientation A_{ij} tensor and the fiber length can then be extracted directly for each individual fiber within the composite. Using image registration, a region which is $\pm 20\mu m$ the slice acquired destructively was compared for fiber orientation.

3.4 Destructive Optical Microscopy

3.4.1 Sectioning, polishing, and plasma etching

After acquiring μ -CT images of the specimen, it was mounted in acrylic for easy handling, placed in a Buehler EcoMetTM 250/AutoMet250 Pro Grinder/Polisher, and polished to the location of the aluminum fiducial marker. A head rotation speed of 60 rpm was used, and the polishing head was either programmed to rotate in the direction of the polishing pad ($>>$) or against the direction of the polishing pad ($><$), with an applied force of 22.24 N (5 lbs) per specimen. The specimen was polished (a) with a 120 grit silicon carbide pad until plane at a speed of 400 rpm ($><$), (b) with a 320 grit silicon carbide pad for 4 minutes at a speed of 400 rpm ($><$), (c) with a 400 grit silicon carbide pad for 2 minutes at speed of 120 rpm ($><$), (d) with a 600 grit silicon carbide pad for 2 minutes at a speed of 120 rpm ($>>$), (e) with 5 μm alumina on a low nap cloth for 90 minutes at a speed of 120 rpm ($>>$), (f) with 0.3 μm alumina on a low nap cloth for 60 minutes at a speed of 120 rpm ($>>$), and (g) with 0.05 μm alumina on a low nap cloth for 30 minutes at a speed of 120 rpm ($>>$). The specimen was sonicated in distilled water after each step, and select images of the surface progression are shown in Figure 3.3. It can be observed in the final polished optical image, shown in Figure 3.3B, that there is very little contrast between the polypropylene matrix and the glass fibers, but good contrast between the polymer matrix and the porosity. Therefore, the final polished surface is used

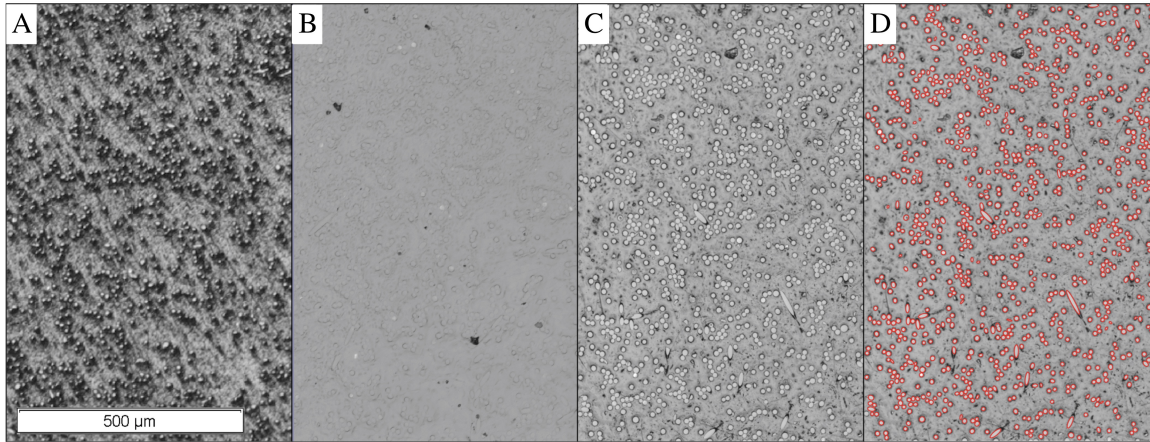


Figure 3.3. Progression of the surface after (A) rough polishing, (B) final polishing, (C) plasma etching, and (D) post-processing with elliptical fits around the cross-section of each fiber.

for porosity detection and for computing the porosity area fraction by extracting the dark pixels of the image.

To enhance the contrast for the purpose of fiber detection, the specimen's surface was plasma etched in a March Jupiter II Etcher with O₂ at a 50 cc flow rate for 1 hour at 100 W under a vacuum pressure of 234 *mTorr*. As can be seen in Figure 3.3C, plasma etching dramatically increased the contrast between the matrix and the fibers. Therefore, the plasma etched surface was used for computing the fiber area fraction (by extracting high intensity pixels), as well as the A_{11} , A_{22} , A_{33} , and A_{12} components of the fiber orientation tensor through elliptical fitting of the cross-section of each fiber [23, 25, 27].

In order to resolve the A_{13} and A_{23} components of the fiber orientation tensor, the polished and etched surface was polished again at the final polish parameter (0.05 μm alumina particle size) for approximately 25 minutes until the surface resembled Figure 3.3B (removing approximately 4.6 μm of material) and then etched again. To summarize, a total of 3 optical images were captured and analyzed: (1) the image of the final polished surface for porosity detection and porosity area fraction com-

putation (referred to as the porosity image), (2) the image of the final polished and etched surface for fiber area fraction and fiber orientation distribution (referred to as the fiber target image), and (3) the image of the successively polished and re-etched surface for resolving the A_{13} and A_{23} fiber orientation components (referred to as the fiber reference image).

These three optical images were acquired using an Olympus BX51M reflected light microscope with an X-Y-Z stage capable of acquiring an automatically stitched image of a large region with automatic focusing and at a user defined magnification. The entire cross-section of the gauge section (2.44 *mm* in diameter) was optically acquired in a seamless image at 10X with a pixel size of 651 *nm*.

3.4.2 Destructively determining the sign of the out-of-plane angle

Following the surface preparation, optical imaging, and elliptical fitting of each fiber cross-section, the fiber reference and target images were post-processed to resolve the A_{13} and A_{23} components of the fiber orientation tensor. The in-plane angle ϕ was measured directly from the in-plane elliptical fit of the cross-section of a fiber in the optical image, and the magnitude of the out-of-plane angle $|\theta|$ was determined by the major and minor axes of the ellipse [25, 58]. As can be seen in Figure 3.4A, the cross section of a fiber with a positive or negative out-of-plane angle (and the same in-plane angle) will result in the same elliptical cross section, creating an ambiguity in the sign of the out-of-plane angle, θ .

To overcome this ambiguity, the fiber reference and fiber target images were post-processed to uncover the sign of the out-of-plane angle shown in Figure 3.4B for thousands of fibers within a given cross section. This was accomplished through a unique automated image processing approach used to match the corresponding cross section of each fiber on the reference and target images. A crucial consideration for this procedure is that the images must be very well aligned. The aluminum foil fiducial marker that was adhered to the surface of the specimen was used to rotate and

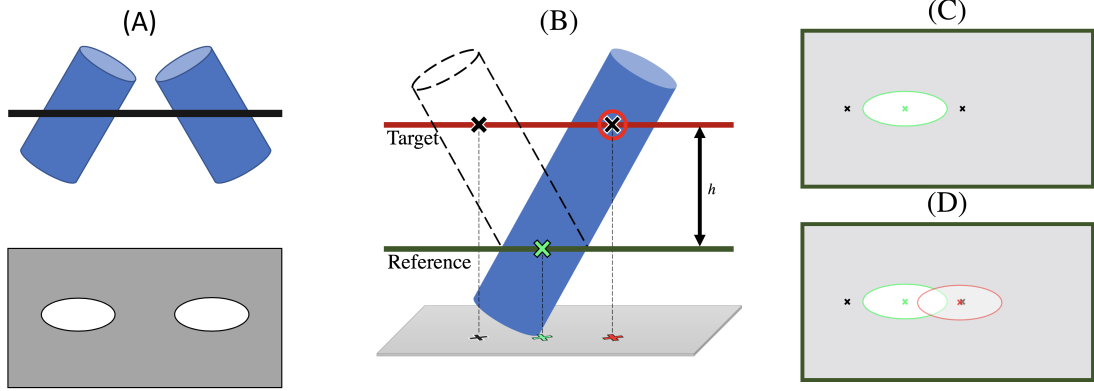


Figure 3.4. Schematic showing (A) the ambiguity of the out-of-plane angle θ , (B) successive polishing to determine the sign of θ , (C) the reference image with the two predicted centroid positions, and (D) the reference image and target image schematically overlaid to determine the sign of θ .

translate the digital optical micrographs to align them to the same relative position, allowing for any differences in the cross-sectional properties of the fibers to be from the out-of-plane angle, and not due to artificial translations from misaligned images.

Since the rate of removal while polishing was measured and kept constant, the distance between the reference image (shown in Figure 3.4C) and the target image (shown as the red ellipse in Figure 3.4D) was known and is referred to as h . Through elliptical fitting, the centroid coordinates of each fiber on the reference image, x_i^r and y_i^r , as well as the centroid coordinates of each fiber on the target image, x_k^t and y_k^t were known, where i ranges from 1 to the total number of fiber cross-sections in the reference image, and k ranges from 1 to the total number of fiber cross-sections in the target image. Using the magnitude of the out-of-plane angle of fiber i on the reference image, $|\theta_i^r|$, and the in-plane angle of fiber i on the reference image, ϕ_i^r , the two candidate positions for the centroid of fiber i on the target image were computed by

$$\begin{aligned} x_j^c &= x_i^r + \frac{h}{\tan(90 - \theta_j^r)} \cos \phi_i^r \\ y_j^c &= y_i^r - \frac{h}{\tan(90 - \theta_j^r)} \sin \phi_i^r \end{aligned} \quad (3.3)$$

where j ranges from 1 to 2 and θ_j^r is given by

$$\theta_j^r = \begin{cases} +|\theta_i^r|, j = 1 \\ -|\theta_i^r|, j = 2 \end{cases} \quad (3.4)$$

It is important to note that the origin of an image in MATLAB is the top left corner of the image, resulting in a positive y direction that points vertically down.

The two candidate centroid positions (one for $+\theta_i^r$ — and one for $-|\theta_i^r|$) were simultaneously compared with the fiber centroids on the fiber target image, as shown in Figure 3.4D. A target fiber cross-section was considered for matching if its centroidal position satisfied the following criteria:

$$\sqrt{(x_j^c - x_k^t)^2 + (y_j^c - y_k^t)^2} < \frac{d}{2} \quad (3.5)$$

where $d/2$ is the fiber radius (in this case, approximately 9 pixels is used, corresponding to $5.86 \mu m$). If only one target fiber matched and $|\theta_i^r - \theta_k^t| \leq 15^\circ$, it was considered a matching fiber. If more than one target fiber matched with the candidate positions (which can occur for groups of very closely packed fibers), the closely packed target fibers were organized in order of *minimum*($|\phi_i^r - \phi_k^t|$). The target fiber with the minimum difference in ϕ which also satisfied $|\theta_i^r - \theta_k^t| \leq 15^\circ$ was considered the final matching fiber. Based on whether $+\theta_i^r$ or $-|\theta_i^r|$ yielded the match from the reference fiber to the target fiber, the sign of θ_i^r was determined and the A_{13} and A_{23} components for each fiber were computed as can be seen in Figure 3.5, where the arrows in Figure 3.5A point from the reference centroid position (x_i^r, y_i^r) to the matched target fiber centroid position (x_k^t, y_k^t) . An outline of the algorithm is also provided in Appendix A.

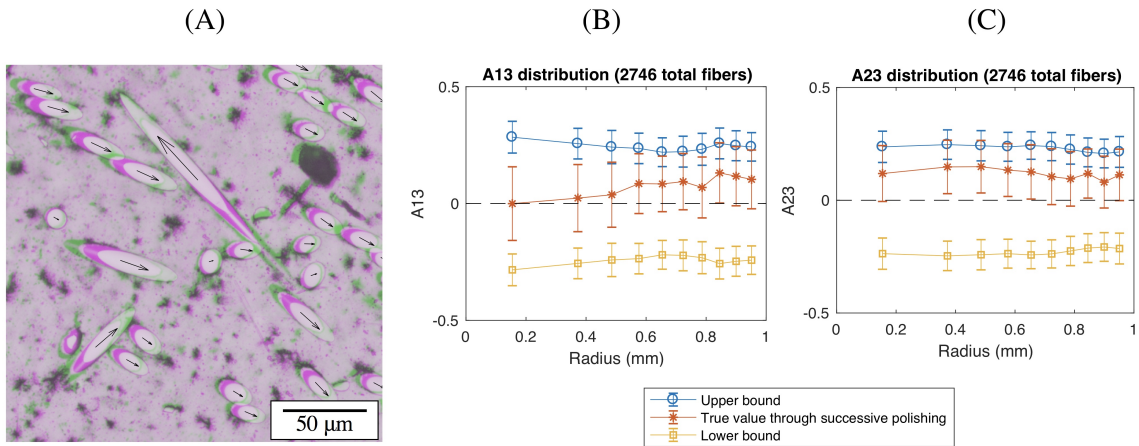


Figure 3.5. (A) Overlay of optical micrographs showing the reference image (green) and target image (red), with arrows pointing from the centroid on the reference image to the centroid on the target image, as well as plots of the (B) A_{13} and the (C) A_{23} components of the A_{ij} tensor, showing the upper bound, the lower bound, and the true value determined through successive polishing and automatic image analysis. (For interpretation of the references to colour in this figure legend, the reader is referred to the Web version of this article.

3.4.3 Destructively measuring the fiber length distribution

In order to destructively quantify the fiber length distribution, a second specimen was selected because the first specimen was sectioned and polished thereby inherently cutting through the fibers, rendering the specimen unusable for a fiber length comparison. The second specimen was placed inside a fitted aluminum cage, and was heated to 538° C and held at temperature for 1 hour to decompose the polymer matrix, leaving behind a tangled web of glass fibers (commonly referred to as a matrix 'burn-off'). This web of glass fibers was down selected using an epoxy cylinder with an approximate diameter of 3.6 *mm* that was injected using a syringe into the web of glass fibers. The down selection was then extracted and heated to 538 ° C and held at temperature for 1 hour to decompose the epoxy, leaving behind the down selection fibers [63]. Next, the fibers were suspended in distilled water and were sonicated to induce fiber separation. The water containing the glass fibers was poured into a petri dish and was heated to evaporate the water. Finally, the petri dish containing the separated fibers was imaged in an Olympus BX51M reflected light microscope equipped with an X-Y-Z stage to enable acquisition of many high resolution images and automated stitching to characterize a large region. This invasive technique has inherent challenges, including - but not limited to - potential damage induced to fibers during the matrix 'burn-off' and sonication processes, and difficulty in the detection of very short fibers in a suspension [26, 34].

3.5 Results

3.5.1 Fiber and porosity volume fractions

Fiber volume fraction, as determined from μ -CT, was compared to the fiber area fraction, determined by the optically acquired reference image, at the location of the fiducial marker adhered to the center of the specimen's gauge section. It was found that the fiber volume fraction determined through non-destructive μ -CT of the

gauge section was 13.4%, while the fiber area fraction determined with destructive optical microscopy was 13.3%. The porosity volume fraction non-destructively was found to be 2.6%, while the porosity area fraction determined from destructive optical microscopy at the matching region was found to be 2.3%.

3.5.2 Fiber orientation distribution

The fiber orientations using μ -CT and then optical microscopy for the exact same region of interest (determined using the aluminum fiducial marker on the same specimen) was computed. This allowed for a one-to-one comparison of the same fibers sampled in the μ -CT images and the destructive optical image. Using 10 concentric annuli with equal areas spanning the specimen's radius, each component of the A_{ij} tensor was averaged along the radial direction of the specimen and is plotted in Figure 3.6, with error bars representing plus and minus one standard deviation. Additionally, the generalized Herman's 3D orientation factor [59,64], which provides a general alignment criteria (whereas $f = 0$ for totally random alignment, $f = 0.5$ for moderate alignment, and $f = 1$ for complete alignment) was computed by

$$f = \frac{3}{2}A_{ij}A_{ij} - \frac{1}{2} \quad (3.6)$$

and non-destructively determined to be 0.52 and destructively determined to be 0.46.

Furthermore, the mean fiber alignments $\bar{\Phi}_X$, $\bar{\Phi}_Y$, and $\bar{\Phi}_Z$ with respect to the X, Y, and Z axes (respectively) can be found in Table 3.1 and were computed by

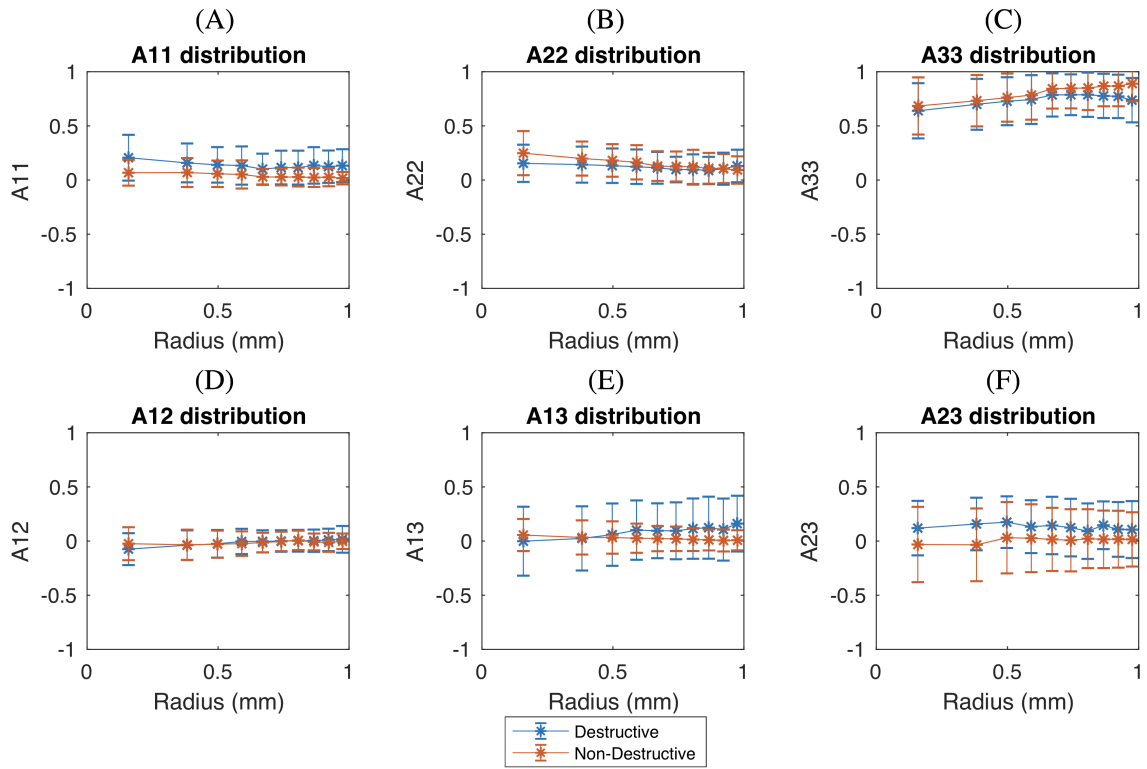


Figure 3.6. The radial fiber orientation distribution averaged along equal area concentric annuli of the specimen for (A) A_{11} , (B) A_{22} , (C) A_{33} , (D) A_{12} , (E) A_{13} , and (F) A_{23} from both non-destructive and destructive characterization of the same fibers.

$$\begin{aligned}
\bar{\Phi}_X &= \cos^{-1} \left(\begin{bmatrix} 1 & 0 & 0 \\ 0 & 0 & 0 \\ 0 & 0 & 0 \end{bmatrix} : \bar{A}_{ij} \right) \\
\bar{\Phi}_Y &= \cos^{-1} \left(\begin{bmatrix} 0 & 0 & 0 \\ 0 & 1 & 0 \\ 0 & 0 & 0 \end{bmatrix} : \bar{A}_{ij} \right) \\
\bar{\Phi}_Z &= \cos^{-1} \left(\begin{bmatrix} 0 & 0 & 0 \\ 0 & 0 & 0 \\ 0 & 0 & 1 \end{bmatrix} : \bar{A}_{ij} \right)
\end{aligned} \tag{3.7}$$

3.5.3 Fiber length distribution

The fiber length distribution was non-destructively determined from μ -CT by using an in-house MATLAB algorithm to compute the distance between the end points of each fiber which were extracted using the post-processing algorithms described in [28]. Destructively, the fiber lengths were measured manually from the optically acquired images of fibers after matrix decomposition using the manual measurement tools in OLYMPUS stream. The weight based fiber length distributions were computed [26, 47] by

$$w_i = \frac{N_i L_i}{\sum_k N_k L_k} \tag{3.8}$$

and are provided in Figure 3.7, where automatic detection using the non-destructive technique captured 58,082 fibers and manual measurement of fibers using the destructive technique captured 2,151 fibers. Since particles and small fragments of fibers are not of interest in this study, only fibers with an aspect ratio greater than 5 were included. Furthermore, the average fiber lengths are provided in Table 3.1, including the weight average fiber length, which was computed [26, 47] by

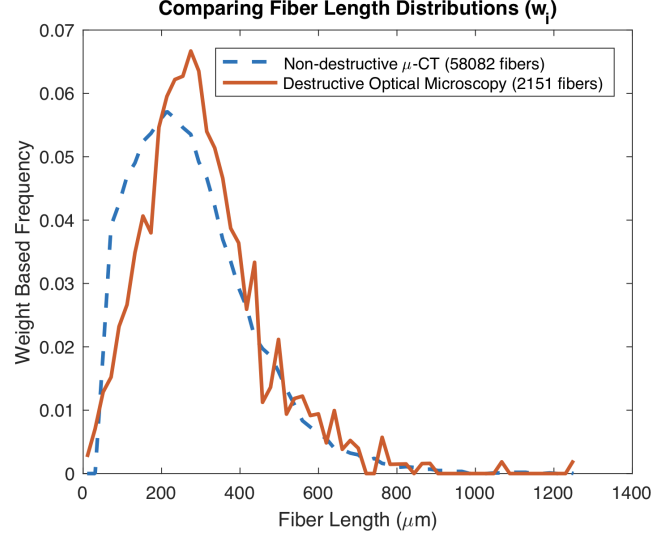


Figure 3.7. Comparison of the weight fiber length distributions determined non- destructively and destructively.

$$L_w = \frac{\sum N_i L_i^2}{\sum N_i L_i} \quad (3.9)$$

3.6 Discussion

In general, it is important to recognize some of the differences in cost and implementation of each destructive and non-destructive technique. Destructive approaches use less expensive equipment: typically a polishing machine, a furnace, and an optical microscope equipped with an x-y-z stage, whereas the final optical images can be used to estimate the fiber and porosity volume fractions, and compute the fiber orientation and length distributions. An advantage of destructive approaches is that the magnification of the images can be adjusted depending on the objective lenses used with the microscope. However, the quality of the microscopic image is directly influenced by the skill of the polisher and the contrast between different microstructural features. This contrast may require enhancement with the use of plasma etching, which

can be expensive. On the other hand, μ -CT is non-contact in nature, thereby allowing a non-destructive analysis of the specimen. However, it requires relatively more expensive X-ray equipment, a small specimen size with some restrictions in geometry (limiting fiber length measurements), and 360° access to the volume of interest. Non-destructive μ -CT is capable of resolving almost all details of the microstructure presented in the 3D image from the same specimen, including the morphology of the porosity (yielding porosity volume fraction) and the morphology of the fibers (yielding fiber volume fraction, fiber orientation, and fiber length distributions) which is advantageous compared to destructive methods, which require separate specimens for the fiber orientation and fiber length measurements. The biggest disadvantage is the rigorous, computationally expensive, and sensitive post-processing that must be conducted to extract meaningful information from the images which inherently include fluctuations in intensity due to fluctuations in X-ray energy. However, once successfully post-processed and reconstructed in 3D (please see [28]), the quantity and quality of the information gathered is comprehensive and robust.

When investigating the microstructural attributes of the composite, it was found that the fiber volume fraction determined through non-destructive μ -CT (13.4%) matched closely to the destructive optical microscopy's fiber area fraction (13.3%) which also matched closely to what was expected from the manufacturing specifications (13.7%). Therefore, fiber volume fraction can be expected to match well using both techniques. The porosity volume fraction determined through μ -CT (2.6%) was slightly higher than that which was computed through porosity area fraction from the destructive optical microscopy images (2.3%). This can be attributed to the very small pores which were captured in the μ -CT images but were not captured in the destructive optical imaging, as can be seen in Figure 3.6. To further quantify this, a one-to-one porosity comparison between the μ -CT images and the optical microscopy image was conducted, and it was found that pores smaller than approximately $700 \mu\text{m}^3$ (equivalent to spherical pores with radii less than $5.5 \mu\text{m}$) were not captured by sectioning and polishing, because they were likely filled in with polished polymer

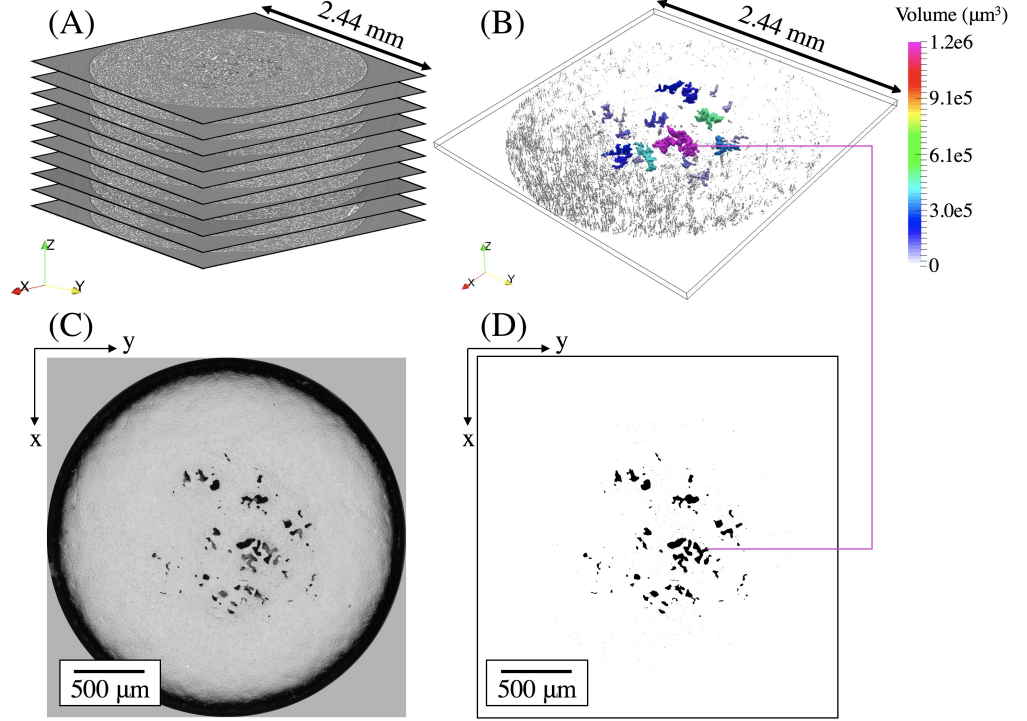


Figure 3.8. A sample of the of X-ray μ -CT images (A) which included the matching optical microscopy image plus and minus $26\ \mu m$, the detected 3D porosity (B), the surface of the specimen achieved through polishing but before plasma etching of the matching region (C) as well as the 2D porosity detected from the optical micrograph (D).

during the polishing routine (sometimes referred to as matrix smearing). After extracting only pores with a volume greater than $700\ \mu m^3$, the porosity volume fraction computed non-destructively was 2.3%, matching exactly to the porosity area fraction computed destructively.

The fiber orientation distribution matched relatively well between both methods as was seen in Figure 3.6 for all of the components of the A_{ij} tensor, with the non-destructive method reporting a slightly better alignment as can be seen in Table 3.1. Small deviations between the orientation distribution data are due to a combination of small perturbations in the elliptical fitting of the pixelized elliptical cross-sections of fibers, which can impact the average values creating fluctuations in the average

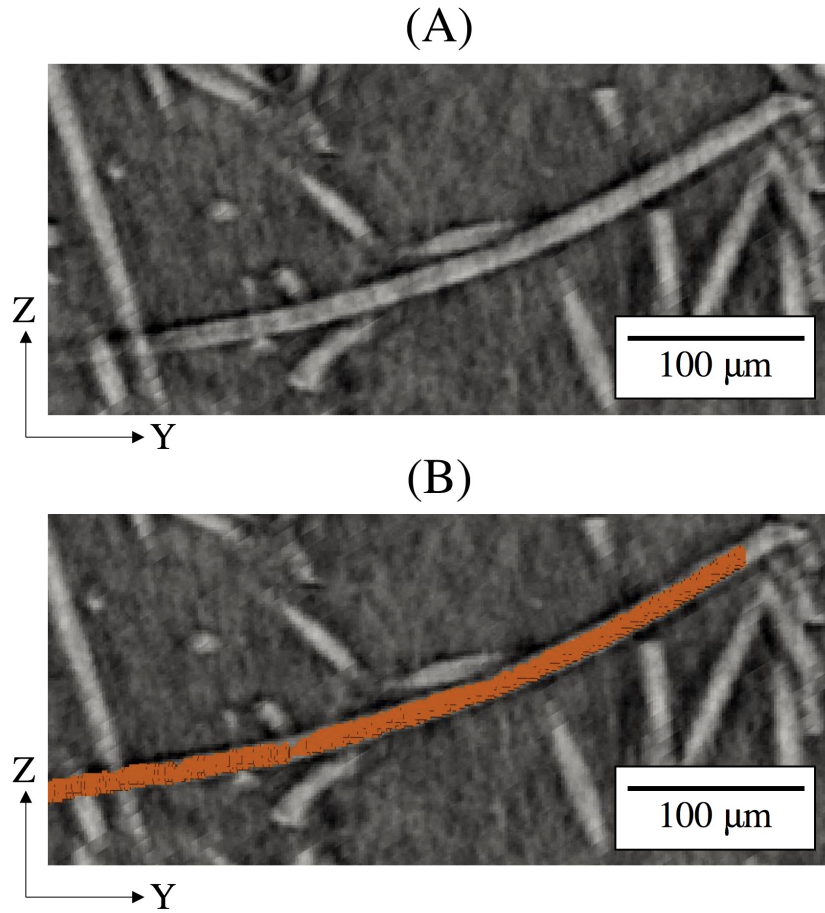


Figure 3.9. An example of a curved fiber towards the flow direction, Z, in a tomography image (A) with its detected 3D morphology overlaid in (B).

A_{ij} components in the range of 0.05 to 0.09 [27], as well as the fact the μ -CT is inherently 3D and therefore captures the full length of each fiber, which includes gentle curvatures of fibers towards the flow direction [65, 66] as can be seen in Figure 3.9, thereby reporting a slightly better alignment. In general, average fiber alignment with respect to each unit vector of the Cartesian coordinate axes can be expected to differ by less than 6° using both techniques.

The fiber length distributions for both the destructive and non-destructive techniques, which were shown in Figure 3.7, matched relatively well exhibiting a small

difference in the distributions and their corresponding average values provided in Table 3.1. This is due to two compounding factors, one being that in the destructive analysis it is difficult to manually find all the small fibers which can be mistaken for noise, and the second being that in the non-destructive analysis, natural fluctuations in intensity due to the X-ray scattering and tomographic reconstruction can sometimes result in a reduction of intensity along the length of a fiber, causing some fibers to appear to have a discontinuity. Furthermore, μ -CT images of the volume have a limited height (in this work, 1.6 mm and therefore on the order of the maximum fiber length) introducing a bias in the length distributions since some fibers touch the upper and lower boundaries of the images. Despite this discrepancy, the maximum fiber length was very similar as was seen in Figure 3.7, and the difference in the number average fiber length was 13.8 μm (corresponding to a difference in average aspect ratio of 1.38), which is relatively small and therefore would not have a notable effect on mechanical stiffness predictions [27]. Using the microstructural properties detected using both techniques (and including a theta correction for fiber orientation [25]), stiffness values in each direction were computed [27, 45, 67] and can be found in Table 3.1. It can be seen that stiffness values are close, but discrepancies exist, specifically in E_{33} aligned in the flow direction, mainly due to the slightly higher alignment detected non-destructively, which was on average 6° more aligned with the flow direction. These discrepancies in the overall stiffness properties of the composite illustrate the importance and need for precise microstructure characterization techniques.

3.7 Conclusion

This work focused on methods used to characterize fiber and porosity volume fraction, fiber orientation, and fiber length distributions in short fiber reinforced composites. Non-destructive X-ray μ -CT images were segmented to extract gas-phase porosity, and then rigorously post-processed to detect each 3D fiber using a supervised

Table 3.1. Microstructural parameters computed using non-destructive and destructive techniques.

Parameter	Non-Destructive Analysis	Destructive Analysis
Fiber Volume Fraction	13.4%	13.3%
Porosity Volume Fraction	2.6%	2.3%
Number Average Fiber Length	196.1 μm	209.9 μm
Weight Average Fiber Length	278.8 μm	305.3 μm
Average Fiber Alignment with X	87.7°	82.3°
Average Fiber Alignment with Y	81.5°	83.3°
Average Fiber Alignment with Z	35.6°	41.5°
3D Fiber Orientation Factor	0.52	0.46
Young's Modulus along X, E_{11}	3.07 GPa	2.93 GPa
Young's Modulus along Y, E_{22}	3.01 GPa	2.87 GPa
Young's Modulus along Z, E_{33}	4.62 GPa	5.60 GPa
Poisson's Ratio in the X-Y, ν_{12}	0.44	0.50
Poisson's Ratio in the Y-Z, ν_{23}	0.26	0.24
Poisson's Ratio in the X-Z, ν_{13}	0.41	0.33

iterative algorithm [28]. The same specimen was then analyzed at a matching region using successive polishing, plasma etching, and optical imaging to conduct a one-to-one comparison of the porosity volume fraction, fiber volume fraction, and fiber orientation distributions, utilizing an algorithm that was created to automatically resolve the ambiguous A_{13} and A_{23} components of the A_{ij} fiber orientation tensor. A second specimen machined from the same rod was selected for matrix 'burn-off' in a furnace, down-selection, secondary 'burn-off,' suspension of fibers in water, sonication, evaporation, and optical imaging to compare the fiber length distributions. Below are the significant findings from this study:

1. The fiber volume fraction computations matched very well using both techniques.
2. The porosity volume fraction detected by sectioning and polishing was slightly lower than that detected in the μ -CT images due to pores smaller than $700 \mu m^3$ (equivalent to spherical pores with radii less than $5.5 \mu m$) being filled in with polymer during polishing. When considering only pores greater than $700 \mu m^3$, the volume fraction computations matched almost exactly.
3. The A_{ij} fiber orientation distribution determined non-destructively and destructively matched fairly well (differing no more than 6° on average with respect to each Cartesian coordinate axes) with the non-destructive approach reporting a slightly higher alignment due to its ability to capture curvatures of 3D fibers in the injection molding flow direction.
4. The average fiber length when computed non-destructively and destructively matched within $13.8 \mu m$, with the non-destructive approach reporting a slightly lower average length due to inherent fluctuations in intensity of the μ -CT images and limitations in the μ -CT scanning volume, and with the destructive approach reporting a slightly higher average length due to difficulty in manually finding and measuring every short fiber.

Overall, the effects of destructive and non-destructive techniques and their ability to detect microstructural features were studied for the same exact region of interest. This analysis provides information necessary for engineers and researchers to identify the advantages/disadvantages of both approaches and understand the quantitative differences in microstructural characterization when using each method in order to confidently qualify composite materials and predict their mechanical behavior.

4. DAMAGE INITIATION: MICRO-VOID NUCLEATION

A version of this chapter was previously published by *Scientific Reports* and is reproduced with copyright permission through the Creative Commons CC-BY 4.0 License. Imad Hanhan, Ronald F. Agyei, Xianghui Xiao, and Michael D. Sangid. Predicting Microstructural Void Nucleation in Discontinuous Fiber Composites through Coupled in-situ X-ray Tomography Experiments and Simulations. *Scientific Reports*, 10(1):3564, 12 2020. DOI: 10.1038/s41598-020-60368-w.

4.1 Introduction

Composite materials have gained attention in many engineering applications, especially in the aerospace and automotive industries due to their low weight and high strength. Specifically, polymer matrix composites have allowed for major weight savings and higher performance aircraft and vehicles. Despite their high rate of implementation, scientists and engineers have faced challenges in predicting their mechanical behavior and performance, especially past the small strain regime and into the damage initiation and damage propagation regimes, because there exist a number of damage mechanisms which are often coupled and are active throughout the life of a component. Compared to continuous fiber composites, discontinuous fiber reinforced polymers exhibit vastly heterogeneous microstructures that can vary significantly depending on the component geometry, making mechanical behavior predictions even more complicated [32–34].

Until recently, most efforts in predicting the mechanical performance of discontinuous fiber composites have been focused on the elastic loading regime during which damage has not yet initiated and progressed [67, 68]. Efforts in understanding and predicting the behavior of fiber composites past the elastic regime have typically focused on attempting to replicate the macroscopic bulk stress-strain behavior of a specimen through phenomenological damage parameters [69]. In recent years, some

microstructural approaches have been used to explore the damage mechanisms in certain composites using homogenization approaches [70] as well as unit cell methods [71]. Experimentally, one *in-situ* study of a thermoset polymer, reinforced with discontinuous carbon fibers, showed that fiber tips play an important role in micro-void nucleation due to high shear stresses, while fiber breakage plays no role [72]. However, for thermoplastic polymers reinforced with discontinuous fibers, researchers have faced even more difficulty because compared to thermoset polymers, thermoplastic polymers experience highly non-linear plasticity creating more complications from a microstructural point of view, in which researchers have applied orientation averaging in unit cells to model this behavior [73].

Efforts in experimentally examining the damage mechanisms of short fiber reinforced thermoplastics through *in-situ* scanning electron microscopy have shown that under tensile loads, damage initiation appears in the form of micro-void nucleation at fiber tips [74,75]. In attempting to improve predictive capabilities and include this damage initiation mechanism, researchers have modeled the macroscopic behavior of short fiber reinforced thermoplastic composites by defining fiber matrix debonding at fiber tips as the governing damage mechanism with good results at simulating the macroscopic stress-strain response [76]. To try and explain this phenomena, researchers have hypothesized that the underlying mechanism of micro-void nucleation in a thermoplastic matrix is similar to that of ductile metals and is related to high tensile hydrostatic stresses or high stress triaxiality [77–79]. However, the appropriate treatment of micro-void nucleation in composites still remains uncertain, mainly because of its stochastic nature and the challenges in computing the local stress states in complex composite microstructures [80].

Recently, high resolution X-ray micro computed tomography (μ -CT) has become a popular tool to characterize composite materials' 3D microstructural features [8, 28, 52, 53, 55], sometimes *in-situ*, in order to observe the evolution of the microstructure [21, 72, 81]. In this work, high resolution X-ray μ -CT was conducted *in-situ* (with a pixel size of $1.3\ \mu\text{m}$) in order to study damage initiation events within

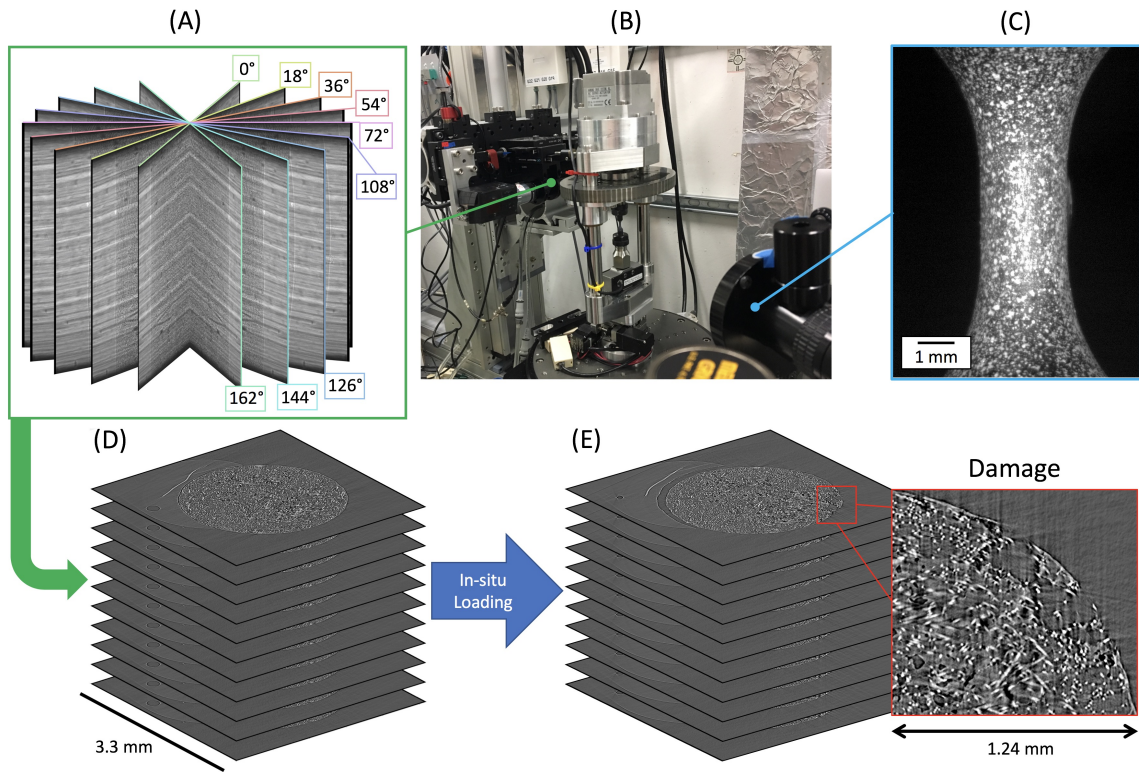


Figure 4.1. An overview of the *in-situ* study where (A) shows a sample 9 of the 1500 X-ray projected radiographs captured by the detector over 180°, (B) shows the *in-situ* loading set-up with the miniature load frame, (C) shows the view of the speckled specimen from the optical camera used for computing macroscopic strain, and (D) and (E) show the reconstructed tomography images at 0 load and at maximum load (just before fracture), respectively.

the microstructure of a discontinuous glass fiber reinforced polypropylene specimen as shown in Figure 4.1, by conducting digital volume correlation (DVC) of the 3D tomography images, and post-processing the tomography images to extract all the microstructural features. The resultant complex 3D microstructure was then examined during deformation and associated initiation of microstructural damage, while a virtual representation of the exact microstructure was simultaneously simulated to quantify the local stresses and strains using a finite element model, including non-linear plasticity in the thermoplastic matrix as well as any porosity manufacturing defects. Through the coupled experiments and simulation of the exact microstructure, this work provides evidence that micro-void nucleation during damage initiation in a fiber reinforced thermoplastic is hydrostatic stress based, validating and propelling forward engineers' and scientists' predictive capabilities past the elastic regime and towards the strength prediction of complex heterogeneous composites.

4.2 Methods

4.2.1 Experimental details

The material used in this work was a polypropylene thermoplastic reinforced with 30% by weight E-glass fibers which were approximately $10\ \mu m$ in diameter and were pre-treated with a tailored silane solution to promote fiber-matrix adhesion. The composite material was injection molded into a cylindrical rod measuring $1.27\ cm$ in diameter and $45.72\ cm$ in length where the flow direction was in the length direction of the rod, and the rod was then machined into a dog-bone shaped specimen with a gauge section diameter of $2.4\ mm$ and length of $5\ mm$ containing fibers that were, on average, approximately $300\ \mu m$ long [15]. The specimen was studied *in-situ* by applying tensile load (at a quasi-static strain rate of approximately $0.001\ s^{-1}$) using a custom motorized screw driven miniature load frame, interrupting the tensile load by holding the cross-head displacement, and acquiring an *in-situ* X-ray μ -CT scan. A total of 58 interruptions and scans were conducted from the unloaded state to

final fracture which occurred at 5.77% strain. The experiments were conducted at Argonne National Laboratory using synchrotron X-rays with an X-ray energy of 25 keV , collected on an area detector placed 75 mm downstream from the specimen. Each X-ray projection was acquired with a 100 ms exposure time every 0.12° while the specimen and load frame were rotated at $0.5^\circ/s$ through a 180° range. The use of synchrotron X-rays enabled a full μ -CT scan to be acquired in 6 minutes. The 1500 X-ray projections captured at each scan were reconstructed using TomoPy [61] resulting in 2D images which stack to form a 3D image with dimensions 2560 by 2560 by 1240 pixels, and a pixel size of $1.3 \mu m$. The exterior surface of the specimen was painted to exhibit a black and white speckle pattern which was optically imaged at each tensile increment, in order to compute (using VIC-2D) the macroscopic strain experienced by the specimen. The reconstructed tomography images acquired just before failure were visually inspected in order to identify the region that contained the ductile fracture zone, which was traced back to the tomography images at the unloaded state shown in Figure 4.4A using slice-by-slice 2D image correlation. The time lapse tomography images of the ductile failure zone were then inspected to identify the location of damage initiation, which was determined to be the region shown in Figure 4.4C. The microscopic strains in the matrix at this region were computed using a DVC algorithm which makes use of fast Fourier transform based cross-correlation in conjunction with an iterative deformation method [82] that was conducted on the tomography images at the unloaded state and at 30% of the macroscopic failure strain using a subset size of 64 pixels and a subset spacing of 4 pixels. In analyzing the DVC results, locations of high ϵ_{zz} strain were defined as voxels with computed strain in the 99.7th percentile of the distribution of ϵ_{zz} . Finally, the tomography images at this region were further inspected in a 2D slice-by-slice comparison between the unloaded state, 30%, and 50% of the macroscopic failure strain to identify the locations of microvoid nucleation during damage initiation within the microstructure, which were then post-processed in 3D using the three detection approaches described below.

4.2.2 Simulation details

Fibers were detected using an iterative and supervised 2D and 3D combined algorithm [28] that was extended with a condensed data approach in order to reduce artificial discontinuities (which only occur to 3% of the fibers). The condensed data approach developed in this work identified the endpoints of each fiber, and organized the information into a matrix which contained the metadata for each fiber, shown in Figure 4.2.

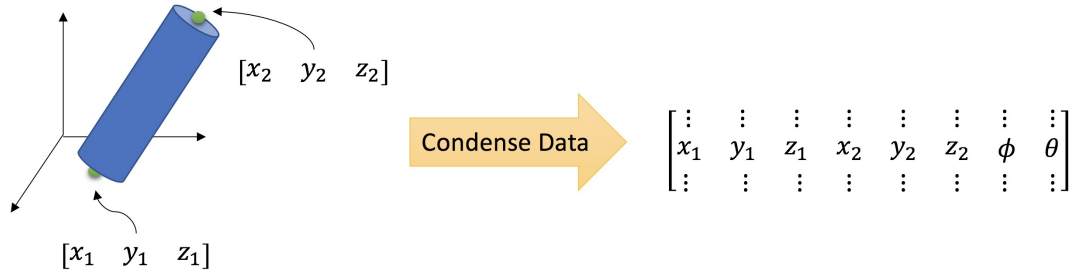


Figure 4.2. A schematic representation of the condensed data procedure, which converts 3D matrix data (high memory demand) to meta-data format, which reduces the file size by approximately 99%.

The condensed file, which offered a file size reduction of 99%, allowed for more computationally efficient analysis. The condensed fiber data was then processed through mathematical matrix operations in order to identify fibers with overlapping end-points that have matching orientations, as shown in Figure 4.3.

Fibers with touching endpoints and matching orientations may contain artificial discontinuities. These fibers were inspected by visual observation of the tomography images at the corresponding fiber locations in order to confirm if there is a true discontinuity, or if the segments should be connected to form a single fiber. Inspections to the 3D data and stitching to the fibers were conducted in ModLayer [83].

Porosity manufacturing defects (and in later loading steps, nucleation of microvoids) were detected using a combination of Weka machine learning segmentation [62]

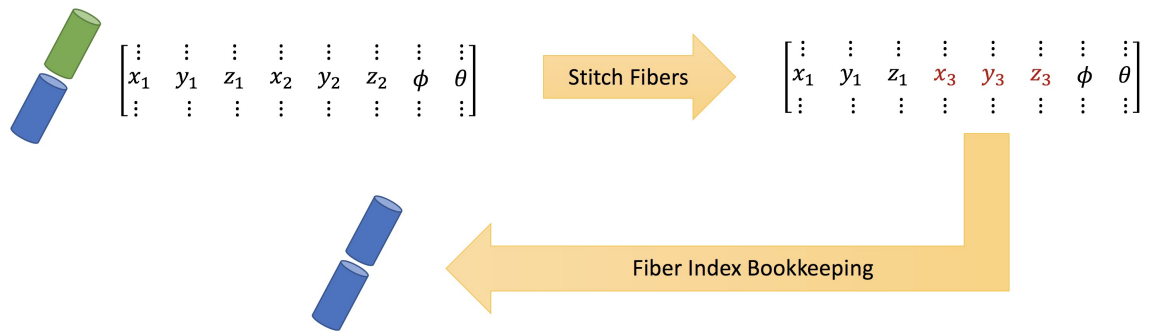


Figure 4.3. A schematic representation of using condensed fiber data to determine which fibers may contain artificial discontinuities.

and manual correction using ModLayer [83]. The specimen's free surface was detected through 2D image processing of each tomography slice using an in-house MATLAB algorithm that utilized the intensity gradient at the free surface, which can be seen in Figure 4.4A, and an initial guess of the approximate center and radius of the cylindrical specimen. This region was then adjusted by mapping the intensity values from a range of $[0, 1]$ to a range of $[0.4, 0.9]$, converted to a binary image using a threshold of 0.655 of the median intensity of the image (which accounts for X-ray energy fluctuations), dilated by a disk structural element with a radius of 4, and finally adjusted to fill any holes in the edge region. The detection of the fibers, pores, and the free surface of the quadrant containing the ductile fracture zone can be seen in Figure 4.4B, with the simulated region's free surface, fibers, and pores shown in Figure 4.4C, 4.4D, and 4.4E, respectively.

The voxels (which were $1.3 \mu m$ in size) corresponding to porosity manufacturing defects were removed from the rendered 3D volume as shown in Figure 4.5A and 4.5B, and the remaining matrix and fiber features were meshed using tetrahedral elements directly from the voxelated microstructure shown in Figure 4.5C and 4.5D. This procedure was conducted in ParaView, and resulted in uniform and ideal tetrahedral elements and perfect bonding between the fibers and the matrix, as shown in Figure 4.5E, which can be generally assumed for fiber reinforced thermoplastics where the fibers have been pre-treated [74]. The meshed fiber elements were assigned linear elastic properties with an elastic modulus of $72.4 GPa$ and a Poisson's ratio of 0.2 [84, 85]. The meshed matrix elements were simulated to include nonlinear plasticity through a multilinear isotropic hardening model [86]. The positive X, negative Y, and negative Z surfaces were constrained using roller boundary conditions, and the positive Z surface was displaced in the positive Z direction by $7.8 \mu m$, matching the displacement experimentally observed by the microstructure at 50% of the failure strain. The microstructural region shown in Figure 4.4C, which was analyzed using finite elements, contained 7.56 million nodes and 44.5 million elements, and was solved using ABAQUS in 92.5 hours utilizing 300 processors and 1.92 TB of memory.

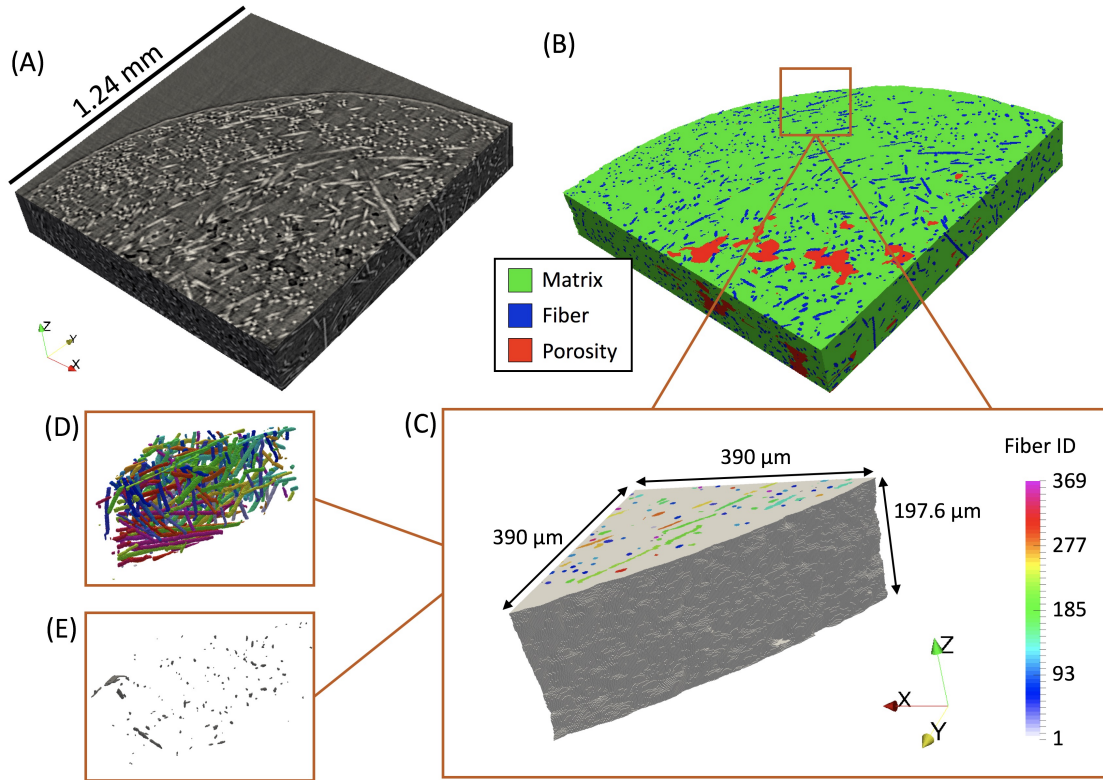


Figure 4.4. The sequence of post-processing the reconstructed tomography images in (A) to achieve high fidelity feature detection shown in (B), which includes specimen edge detection, porosity manufacturing defect detection, and individual fiber detection in 3D, as well as the instantiated model (C), the 368 fibers within the model (D), and the manufacturing porosity defects within the model (E).

In analyzing the results of the simulation, hydrostatic stress hot-spots were defined as agglomerations of at least 1000 connected matrix elements that were all in the 99.997th percentile of hydrostatic stress, slightly higher than the DVC analysis due to the finer mesh size.

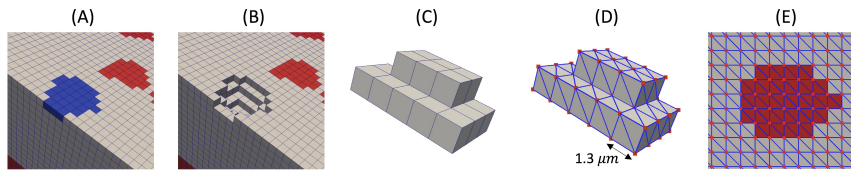


Figure 4.5. The procedure used to mesh the instantiated model where (A) shows a fiber in red, a porosity manufacturing defect in blue, and the matrix in grey, (B) shows the removed manufacturing pore, (C) and (D) show the voxels meshed using tetrahedral elements, and (E) shows a meshed fiber in the matrix.

4.3 Results

4.3.1 The role of porosity manufacturing defects and the ductile fracture zone

The specimen was loaded in tension until fracture, and the *in-situ* X-ray μ -CT images allowed for the observation of the fibers, porosity manufacturing defects, as well as the tracking of microstructural damage events that led to final fracture. Each fiber detected in the cylindrical specimen is shown in Figure 4.6A, with a green outline highlighting the region of the specimen which experienced ductile fracture that led to final fracture, shown in Figure 4.6B. Manufacturing defects in the form of preexisting large pores were detected in the center of the specimen as can be seen in Figure 4.6C, with preexisting small pores present closer to the free surface. As the specimen was loaded and ductile fracture occurred, it was found that these large pores did not significantly coalesce and grow leading to final fracture as expected in typical ductile fracture [87]. Instead, a large void nucleation event occurred near the free surface of the specimen circled in Figure 4.6D, which - just before fracture - finally coalesced with the preexisting large pores leading to final fracture shown in Figure 4.6E. This shows that while porosity manufacturing defects have historically been viewed as a major detriment to a composite's strength [88], in this discontinuous reinforced thermoplastic, a variety of complex microstructural features exist which can be more detrimental to the overall mechanical performance. In this composite specimen, it was found that these features existed at the critical region near the free surface circled in Figure 4.6D, which was analyzed in more detail to detect the exact locations of damage initiation, and simulated through a finite element model to compute the stresses and strains.

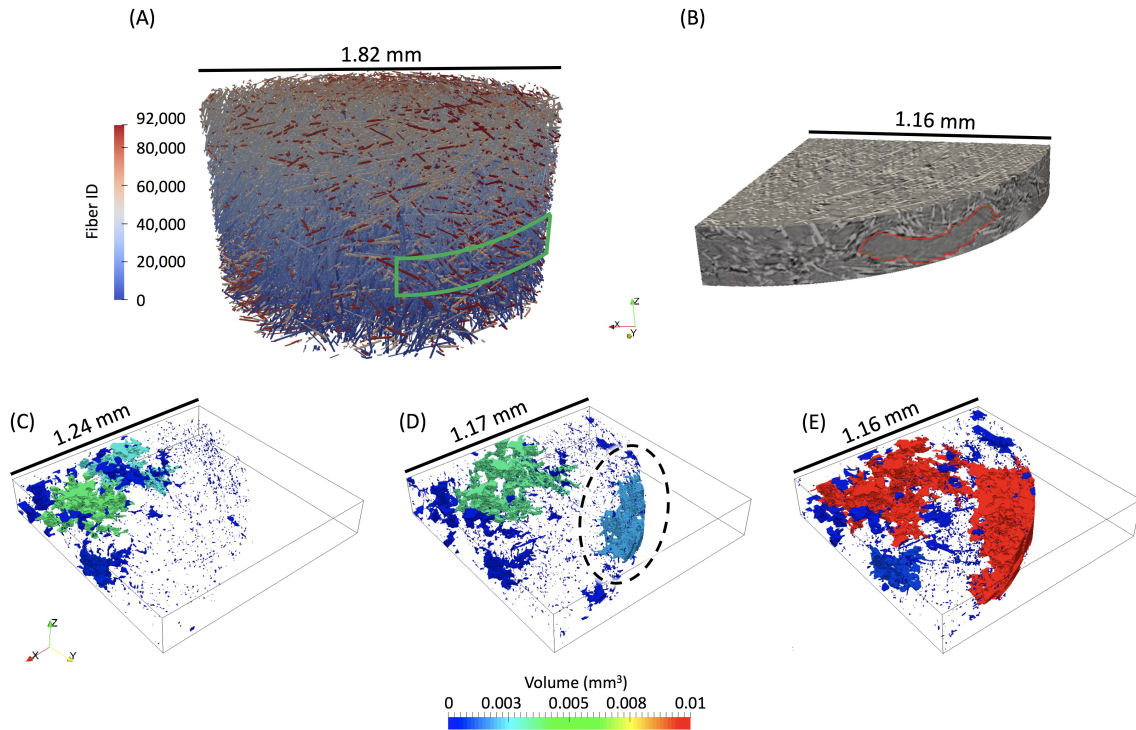


Figure 4.6. Shown in (A) are the fibers detected within the gauge section of the specimen at 0 load where each fiber is individually detected and assigned a fiber ID, and where the green outline indicates the location of ductile fracture observed experimentally, which is also shown in the tomography images just before fracture in (B). Pre-existing porosity, micro-void nucleation, and eventual void coalescence in the ductile fracture zone are shown in (C) at 0 load, (D) at 96% of failure, and (E) just before failure.

4.3.2 Experimental micro-void nucleation during damage initiation

Experimentally, five locations within the critical region showed evidence of micro-void nucleation during damage initiation and have been visualized at the unloaded state in Figure 4.7A and at 50% of the macroscopic failure strain in Figure 4.7B, with a sample of the DVC results overlaid in Figure 4.7C. Two of the five locations consisted of T-type intersections, where at least one fiber was well aligned with the loading direction and interacted with fiber(s) that were highly misaligned with the loading direction. One region consisted of two well aligned fibers with slightly overlapping end-points, where a micro-void nucleated at one fiber end-point, but not both. Another region consisted of two fibers highly aligned with the loading direction that had nearly touching end-points, which resulted in micro-void nucleation between the end-points and a coupled early fiber breakage in a neighboring fiber shown in Figure 4.7D-4.7G. Lastly, one case of micro-void nucleation consisted of two well aligned fibers with end-points near a small fragment of glass fiber, all of which are shown in Figure 4.7B. It is important to note that the locations of micro-void nucleation, while always relating to fiber tips, were not confined to one single configuration of fiber tips, but instead included a few different configurations.

4.3.3 Simulated heterogeneous stresses and strains in the microstructure

The results of the finite element simulation of the exact microstructure experimentally analyzed, which has been visualized in Figure 4.8A and Figure 4.8B, showed that there was in fact a large degree of heterogeneity in the strains and stresses. As expected, the ductile thermoplastic matrix experienced most of the deformation as can be seen by the strain plot in Figure 4.8C, while the fibers, acting as the toughening constituent in the composite, experienced most of the stress in the specimen, shown by the stress plot in Figure 4.8D. The hydrostatic stress was computed by

$$\sigma_{hyd} = \frac{\sigma_{xx} + \sigma_{yy} + \sigma_{zz}}{3} \quad (4.1)$$

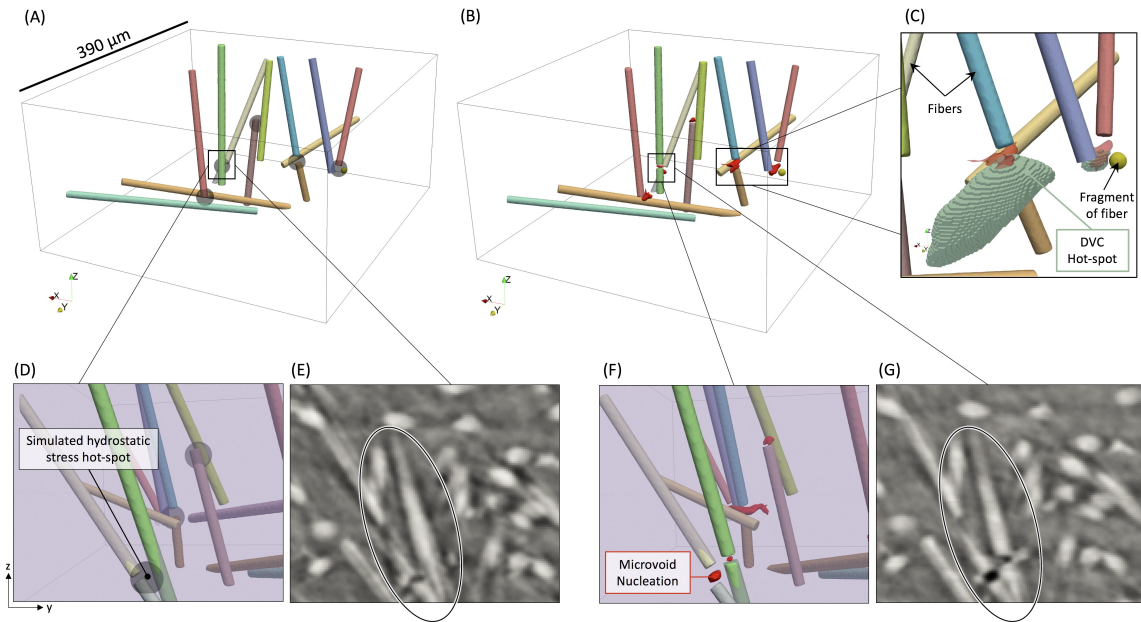


Figure 4.7. The fibers that interacted with the micro-void nucleation events (A) at the unloaded state with grey spheres at the locations of simulated matrix hydrostatic stress hot-spots, and (B) at 50% of the macroscopic failure strain with the experimentally determined micro-void nucleation shown in red, with (C) an overlay of a sample of the DVC ϵ_{zz} strain hot-spots. The coupled micro-void nucleation and early fiber breakage is shown in (D) and (E) at the unloaded state, and in (F) and (G) at 50% of the macroscopic failure strain.

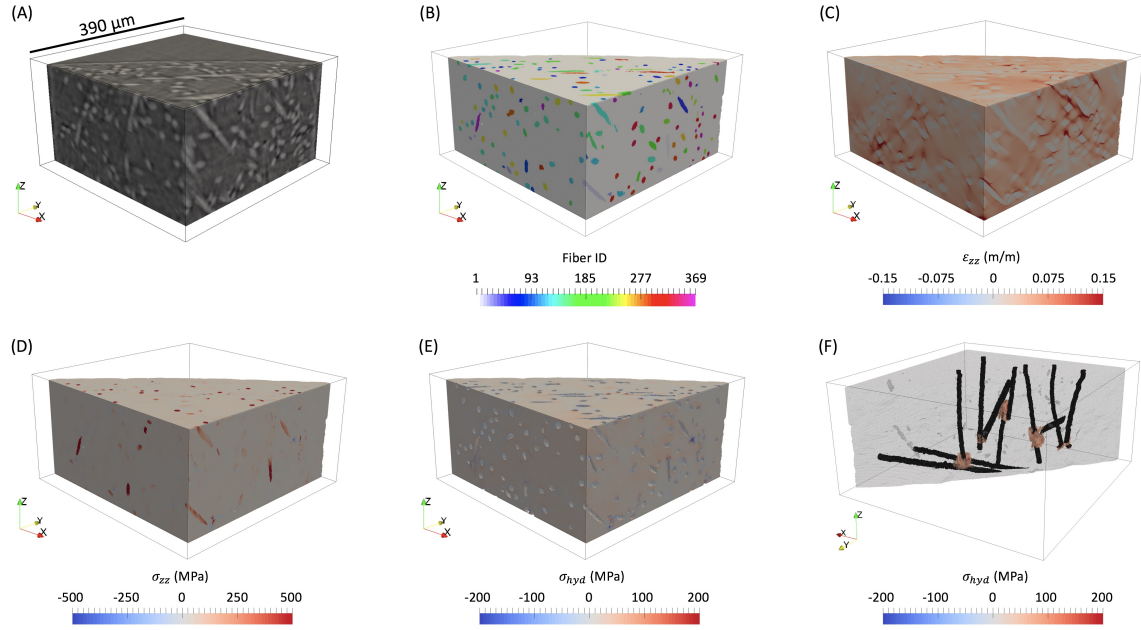


Figure 4.8. An overview of the cropped simulation results (cropped to visualize away from the boundary conditions) of the specimen region shown in the tomography images of (A) which were post-processed for feature detection shown in (B). The heterogeneous strain in the loading direction (ϵ_{zz}) is shown in (C), the heterogeneous stress in the loading direction (σ_{zz}) is shown in (D), the heterogeneous hydrostatic stress (σ_{hyd}) of the matrix is shown in (E), and the agglomerations of matrix elements in the 99.997th percentile of hydrostatic stress, with the fibers they interact with, are shown in (F).

and was found to be normally distributed in the matrix, visualized in Figure 4.8E, with an average hydrostatic stress of 10.83 MPa and a standard deviation of 15.96 MPa. While there were scattered regions within the matrix whose elements experienced high hydrostatic stress (sometimes in a single line of elements and other times isolated only to the side of a fiber at a corner of a 3D voxel), only large agglomerations, referred to as hydrostatic stress hot-spots, were of interest because they ensured that the region of high (99.997th percentile) matrix hydrostatic stress was not artificially induced from meshing effects, and are shown in Figure 4.8F.

4.4 Discussion

The matrix hydrostatic stress hot-spots computed in the simulation have been overlaid onto the experimental results in Figure 4.7A as transparent black spheres within the microstructure. These simulated hydrostatic stress hot-spots correlated directly to the five locations of micro-void nucleation experimentally observed in the microstructure during damage initiation, shown by the red regions in Figure 4.7B. Of the five cases of hydrostatic stress hot-spots in the matrix and their corresponding micro-void nucleation events, two were of interest because of their unique behavior. The first case of interest was a location that experienced coupled micro-void nucleation and fiber breakage. Fiber breakage occurring at 50% of the macroscopic failure strain of 5.77%, experimentally observed in Figure 4.7D-4.7G, is atypical in these composites [74]. Specifically, the green fiber shown first at the unloaded state in Figure 4.7D, and then at 50% of the failure strain in Figure 4.7F, was the only fiber that broke in the critical region at this early loading condition; yet this fiber was simulated to experience (prior to micro-void nucleation) only 45% of its ultimate tensile strength [84] at the same loading condition observed experimentally. When overlaying the simulation results, it can be seen that a matrix hydrostatic stress hot-spot was in contact with the fiber at the location of fiber breakage, which experimentally resulted in micro-void nucleation in the matrix next to the fiber, followed by early fiber breakage shown in Figure 4.7E and 4.7G. This provides evidence that high hydrostatic stress can be used not only as a metric to describe and predict micro-void nucleation during damage initiation, but also - in certain cases - describe micro-void nucleation coupled with other damage mechanisms.

Another case of micro-void nucleation that was of interest consisted of two fibers that were well aligned with the loading direction which interacted with a small fragment of a glass fiber that was approximately spherical, which was also experimentally verified by the DVC analysis shown in Figure 4.7C. The experimentally-based DVC analysis showed that the highest strain values were localized in the region of

micro-void nucleation, which corresponded spatially to the hydrostatic stress hot-spot predicted by the finite element model. Typically, engineers are not interested in fragments of fibers with aspect ratios close to one because they contribute almost no load bearing capability when compared to their longer cylindrical neighbors present in the microstructure [26, 45, 47]. Therefore, techniques and algorithms to detect and characterize fibers are typically not suitable for $l/d \leq 1$, which can be easily confused with noise [15, 26]. In this work, the fragment of glass was manually observed in the *in-situ* tomography images, detected as a fragment of a fiber, included in the microstructural simulation, and proved to be a region of high hydrostatic stress and a region of corresponding micro-void nucleation, as was seen in Figure 4.7A, 4.7B, and identified more closely in Figure 4.7C. This provides evidence that while short fragments (even as short as $l/d = 1$) in the presence of long fibers can be ignored in elastic stiffness predictions, as they do not strongly influence the elastic properties, they can strongly influence damage initiation past the elastic regime and therefore must be included and considered in strength predictions.

4.5 Conclusion

In general, this work coupled experiments and simulations to show that large porosity manufacturing defects do not consistently play a role in initiating and propagating damage, and that additional microstructural features, like T-type configurations and overlapping fiber tips, play a critical role in the microstructure's overall resistance to damage initiation. The experiment, which tracked approximately 92,000 fibers, as well as manufacturing and damage induced porosity, identified the critical region of the material that led to failure. A high fidelity model (comprised of 44.5 million elements) was created of this sub-region, in which 368 fibers were instantiated. The results showed that the 5 experimentally observed locations of micro-void nucleation corresponded with the 5 highest regions of hydrostatic stress, which substantiates the use of the hydrostatic stress metric to explain and predict micro-void

nucleation in the microstructure of fiber reinforced thermoplastic composites, proving a long standing hypothesis of the role of stress triaxiality in damage initiation for thermoplastic matrix composites. Lastly, this work showed that although small fragments of fibers, which are almost negligible in size compared to the average fiber length, can be ignored during elastic mechanical property predictions, they must be included in the damage initiation and strength predictions of these composites.

5. DAMAGE PROGRESSION: CRACK PROPAGATION

A version of this chapter was published in *[pending publication]* and is reproduced with copyright permission under license [pending publication]. Imad Hanhan and Michael D. Sangid. Damage propagation in short fiber thermoplastic composites analyzed through coupled 3D experiments and simulations. DOI: [pending publication].

5.1 Introduction

Short fiber composites have become popular in many engineering applications due to their relatively low cost of manufacturing, especially for complicated 3D geometries. The microstructure of these composites, which is typically characterized by parameters like the fiber volume fraction, fiber orientation distribution, fiber length distribution, and porosity volume fraction, is dependent on the manufacturing parameters [32–34] and strongly influences the mechanical performance [37–41]. Therefore, researchers have developed techniques and tools to not only predict the microstructure of these composites based on their manufacturing parameters [47, 89, 90], but to also try and predict the mechanical response using these microstructural parameters [45, 59, 67].

However, predicting the complete mechanical behavior of these short fiber composites is challenging due to the heterogeneity of the microstructure and its behavior past the elastic regime. Therefore, most predictive capabilities have been focused on the elastic loading regime [67, 68], before damage initiation or progression has occurred. These anisotropic elastic properties can be predicted using fiber volume fraction, orientation, and length distributions. Some recent work has been done in predicting the bulk mechanical response past the elastic regime, towards the strength predictions of short fiber composites, using phenomenological damage parameters and/or homogenization [69–71].

Within the microstructure of thermoplastic composites when loaded past the elastic regime, damage initiation is usually observed in the form of micro-void nucleation in the thermoplastic matrix, specifically at fiber tips, which early works have shown through *in-situ* scanning electron microscopy [74,75]. In understanding and predicting this behavior, the two main challenges for these composites are the highly non-linear response of the thermoplastic matrix (which experiences significant plasticity) and its interaction with fibers of varying lengths and orientations [73]. For damage initiation, a recent work used coupled 3D experiments and simulations to show that micro-void nucleation during damage initiation is related to localized high hydrostatic stresses in the matrix at fiber tips [91]. However, it is unclear how micro-voids evolve during damage progression, especially in 3D.

One historically observed behavior during the early stages of damage progression is debonding of the fiber and the matrix [92]. In an effort to retain the integrity of a fiber's load bearing ability, researchers have worked to develop a number of different techniques to improve the adhesion of the fiber and the matrix through fiber surface pre-treatments [93]. These fiber pre-treatments create a chemical reaction at the surface of the fiber with a thickness that varies depending on the material system; for E-glass fibers and a polypropylene matrix, it is expected to be on the order of 100 *nm* [94]. The development of such fiber treatments has proven to be very successful, making debonding extremely unlikely (occurring only in the early loading sequence for a small fraction of fibers which may have had unfavorable bonding conditions) as has been shown through fractography [74,95]. With well bonded fibers, debonding is not typically observed during damage progression. Instead, due to strong adhesion to the fiber, interfacial microcracking of the matrix along fiber sides is the first observed behavior during damage propagation, and it occurs late in the monotonic loading sequence (at about 75% of the failure load) [74]. This is hypothesized to be a result of a shear stress concentration along the fiber side [74].

A second observed behavior active during damage progression is cracking through the matrix in a manner that is not along a fiber edge, first referred to as 'zigzag'

matrix microcracking, which activates to connect and coalesce micro-voids and interfacial matrix cracks [74]. To try to understand this mechanism of matrix cracking, researchers isolated a single fiber in a matrix and analyzed the behavior of matrix cracking through surface measurements. It was found that even with a single fiber in a matrix, there exists a mechanism of matrix cracking which is not necessarily fiber interface mediated. This observed mechanism has been described more broadly as mode γ cracking [96] and fiber avoidance cracking [97,98], or more specifically by its shape, such as penny [99], conical [100,101], conoidal (a mix of conical and flat) [102], and helicoidal [102]. In this work, this form of matrix cracking, that is not fiber interface mediated, will be simply referred to as conoidal matrix cracking.

A third behavior sometimes observed during damage progression is fiber breakage. In general, fiber breakage is not a common occurrence in short fiber reinforced thermoplastic composites and is either not observed [74] or considered to be rare [76]. While uncommon, some fiber breakage events have been documented for these material systems, and are generally characterized as either (1) transverse breakage of a fiber that is well aligned with the loading direction (which is well understood), or (2) longitudinal breakage of a fiber highly misaligned with the loading direction, which is less common and not well understood [21].

From a prediction standpoint, interfacial matrix cracking along a fiber, conoidal cracking through the matrix, and longitudinal fiber breakage have been challenging to predict due to a lack of understanding of the physical phenomena that govern their behavior. Specifically, conoidal matrix cracking has proven to be challenging for researchers to predict because of its apparent stochastic nature. In an attempt to predict this conoidal matrix cracking behavior, researchers studied a single isolated perfectly aligned fiber in an epoxy matrix in 2D, and through a modified Rice and Tracey model were able to successfully predict the angle between a conoidal matrix crack and the fiber (within 2°) [101]. However, there has not been a clear and comprehensive explanation of the interaction of interfacial cracks and conoidal cracks, especially in 3D for a thermoplastic matrix, other than they might be accelerated by

shear stress [97, 103]. Understanding the physical phenomenon that drives conoidal matrix cracking and interfacial matrix cracking along a fiber, especially if it results in major damage coalescence, as well as exposing possible causes for longitudinal fiber breakage of misaligned fibers, would allow for more accurate predictions of the complete mechanical behavior of short fiber reinforced thermoplastics.

Therefore, this work coupled an *in-situ* X-ray micro-computed tomography (μ -CT) experiment (shown in Figure 5.1) with a 3D finite element method (FEM) simulation of the exact microstructure, including all fibers, all manufacturing induced pores, and non-linear behavior in the thermoplastic matrix, in order to compute the stresses in the microstructure and compare them to the behavior of damage propagation. Specifically, locations of damage initiation within the ductile fracture zone were tracked as the material was loaded, and processed through robust image processing and segmentation procedures to extract each individual fiber and pore [91]. The experimental 3D behavior of matrix cracking was analyzed for regions of interface mediated matrix cracking, as well as conoidal matrix cracking. The finite element simulation, which contained over 7 million elements, computed the full stress field and allowed for a direct comparison to the experimentally observed matrix cracking within the microstructure.

This paper will first describe the material, followed by the experimental procedure and its corresponding tomography post-processing. The methods of the FEM simulation will then be described, followed by the results and discussions of three damage propagation mechanisms active during damage propagation. The behavior of the material during damage propagation, which occurred between $0.75\varepsilon_f$ (75% of the macroscopic strain to failure) and $0.85\varepsilon_f$ (85% of the macroscopic strain to failure), was analyzed for regions of damage coalescence which eventually led to major ductile failure in the ductile fracture zone. Through the coupled experiment and simulation analysis, this work determined the active mechanisms during damage propagation, and provided insight on the physical phenomena that govern interfacial matrix cracking and conoidal matrix cracking. Lastly, fiber breakage was analyzed

and categorized as either transverse breakage of a well aligned fiber, or longitudinal breakage of a misaligned fiber. Only one fiber was found to break in a longitudinal fashion, and is explored in this analysis. Overall, the results of this work provide a comprehensive understanding of the physics governing the coalescence of damage initiation sites within the complex and heterogeneous microstructure of short fiber reinforced thermoplastics, increasing the understanding of the micromechanical response past damage initiation and propelling engineers towards strength and failure prediction of these short fiber composites.

5.2 Materials and Methods

5.2.1 Composite Material

The material used in this work was a polypropylene matrix reinforced with 30% by weight E-glass fibers which are approximately $10\ \mu m$ in diameter. The glass fibers were pre-treated with a tailored silane solution to promote adhesion between the fibers and the polymer. The composite material was injection molded into a cylindrical rod with a diameter of $1.27\ cm$ and a length of $45.72\ cm$, where the injection molding flow direction was in the length direction of the rod. From the injection molded rod, a smaller dog-bone shaped specimen was machined from the center with a grip diameter of approximately $6.3\ mm$, a gauge section diameter of $2.5\ mm$, and a gauge section length of $5\ mm$.

5.2.2 Experimental Details

An *in-situ* tomography study was conducted at the the Advanced Photon Source at Argonne National Laboratory using the assembly shown in Figure 5.1A. Each X-ray projection, which was acquired with an X-ray energy of $25\ keV$, was collected on an area detector placed $75\ mm$ downstream from the specimen with an exposure time of $100\ ms$ collected every 0.12° . The assembly, which included the specimen

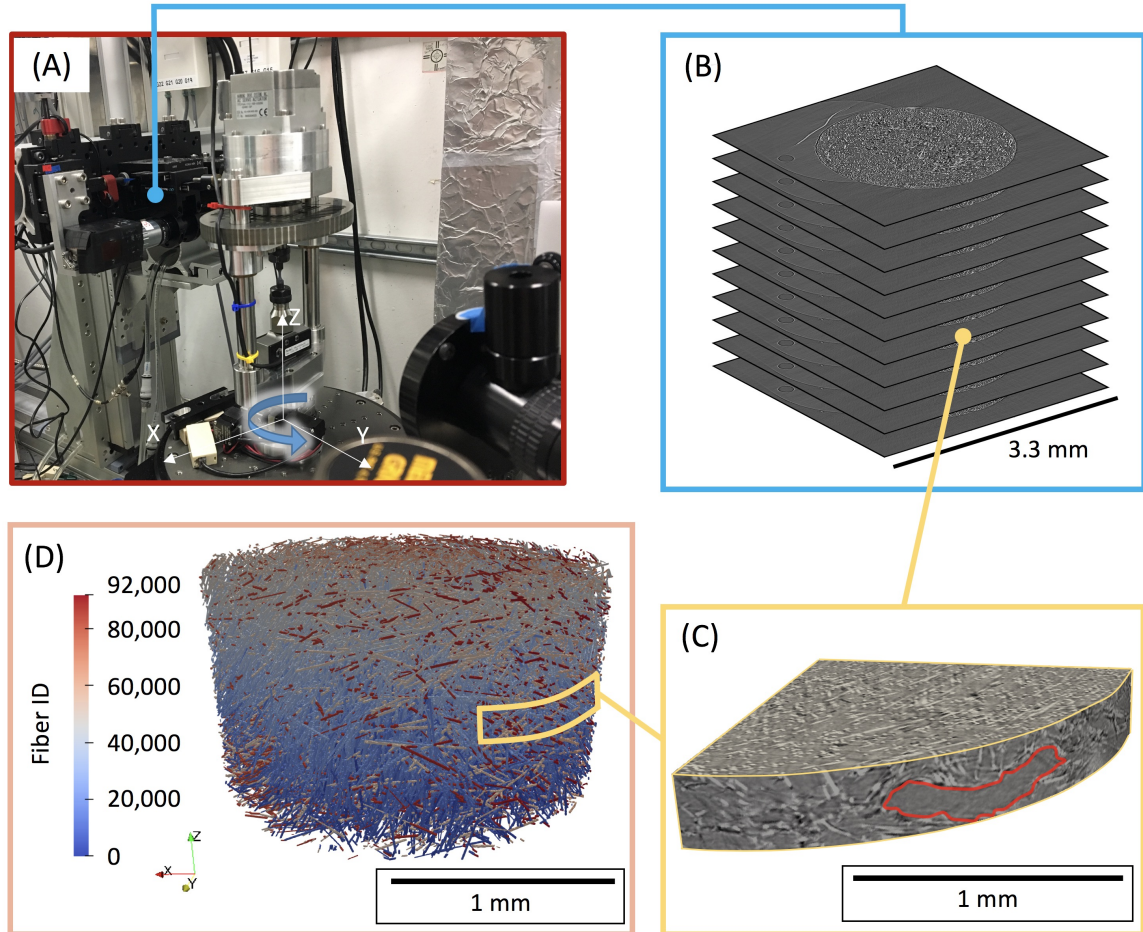


Figure 5.1. An overview of the *in-situ* study where (A) shows the *in-situ* loading set-up with the miniature load frame, (B) shows a sample of the reconstructed tomography images, (C) shows the ductile fracture zone just before fracture, and (D) shows a sample of the fibers detected in the microstructure (cropped away from the edges by 340 μm radially).

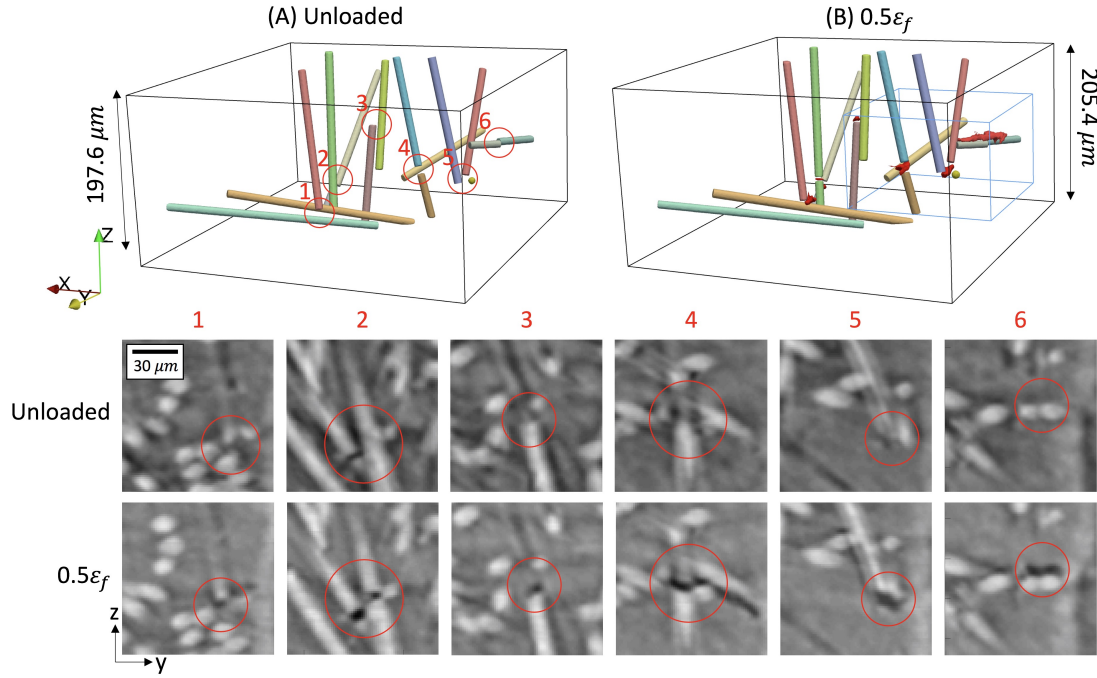


Figure 5.2. An overview of the damage initiation events labeled 1 through 6 that occurred within the ductile fracture zone visualized at (A) the unloaded state, and at (B) $0.5\epsilon_f$, with a blue box indicating the region of interest for the damage propagation analysis, and with corresponding tomography images at each of the 6 locations, where sites labeled 1-5 were micro-void nucleation, and site 6 was early debonding.

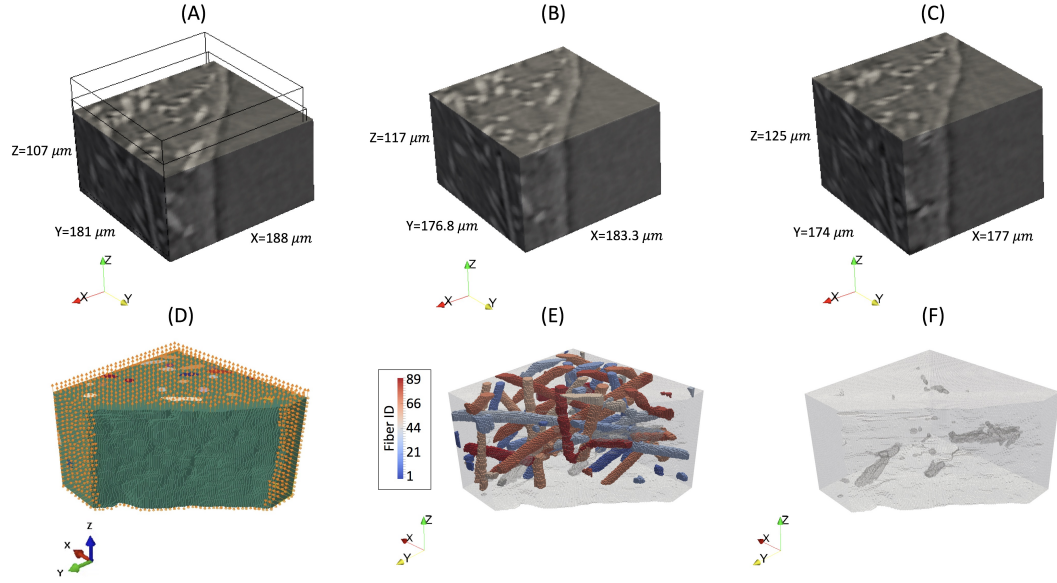


Figure 5.3. An overview of the coupled experiment and simulation, where (A) is the region of interest for the damage propagation analysis at 0 load, (B) is the tracked region at $0.5\varepsilon_f$ that contained sites of damage initiation which grew significantly and coalesced in (C) at $0.85\varepsilon_f$. Simultaneously, (D) shows the simulation of the region of interest from $0.5\varepsilon_f$ to $0.85\varepsilon_f$, where the displacement boundary conditions match exactly the experimental results from (A) to (C). The detected fibers are shown in (E), and the voids present at $0.5\varepsilon_f$ can be seen in (F), where the three largest voids are the sites of damage initiation.

placed within a custom miniature load frame, was rotated at $0.5^\circ/s$ through a 180° range. The use of synchrotron X-rays allowed for a μ -CT scan of a volume with dimensions 3.33 by 3.33 by 1.61 mm to be acquired with a pixel size of 1.3 μm in about 6 minutes. The 1500 X-ray projections acquired during each tomography scan were reconstructed using TomoPy [61] resulting in 2D images which stack to form a 3D image, as shown in Figure 5.1B.

Using the custom miniature load frame, the specimen was loaded in tension by incrementally displacing the cross-head 0.01 mm at a quasi-static cross-head displacement rate of approximately $0.001 s^{-1}$, holding the cross-head displacement, and acquiring an *in-situ* tomography scan. Once the scan was completed, the cross-head was displaced 0.01 mm again and held for the next scan. The 3D time-lapse tomography data allowed for the observation of damage (Figure 5.1C) and the extraction of microstructural features, including each fiber (Figure 5.1D). The exterior of the specimen was painted with a black and white speckle pattern and monitored using an optical camera at each increment in order to allow for the computation of macroscopic strain through digital image correlation which was conducted using VIC-2D. A total of 58 scans were acquired between the unloaded state and final fracture, which occurred at 5.77% macroscopic strain.

5.2.3 Experimental Post-Processing

The tomography images acquired at $0.99\varepsilon_f$ (99% of the macroscopic strain to failure) were inspected using ImageJ and the ductile fracture zone (the region of ductile fracture which transitions to brittle fracture just before final failure [74]) was determined [91]. Using six face 2D cross-correlation in MATLAB, the ductile fracture zone was traced from $0.99\varepsilon_f$ back to the microstructure at $0.85\varepsilon_f$, $0.7\varepsilon_f$, $0.5\varepsilon_f$, $0.3\varepsilon_f$, and 0 load.

The 3D tomography images at each load step were adjusted first using median scaling [104], followed by three general procedures: fiber detection, porosity detection,

and free surface detection. Fiber detection was conducted using a combined 2D/3D iterative approach developed by Agyei and Sangid [28]. The algorithm iteratively enhances and segments each 2D image in the stack of reconstructed μ -CT images. The cross-section of each fiber on each slice is fitted using an elliptical fit, and this ellipse data is stacked and undergoes a number of 3D segmentation steps [28]. The segmentation of the fibers was inspected and corrections to the automated segmentation were conducted using ModLayer [83].

Fibers in the experimental analysis, which played a role by interacting with damage events within the ductile fracture zone, were rendered in ParaView using a cylindrical fit of the detected fibers to aid in visual interpretation. These can be seen in Figure 5.2A and Figure 5.2B at the unloaded state and at $0.5\varepsilon_f$, respectively. An in-depth 3D reconstruction of the surface of certain fibers of interest was conducted by first segmenting pixels in the region of the fiber with normalized intensity greater than 0.65 followed by inspection and segmentation correction using ModLayer [83]. The manufacturing induced porosity in the unloaded state, as well as micro-voids that nucleated after loading, were detected using Weka machine learning segmentation [62] and manually corrected using ModLayer [83]. This procedure aided in the 3D interpretation of damage events as can be seen in Figure 5.2B.

The specimen's free surface was determined through 2D image processing of each tomography slice using an in-house MATLAB algorithm that utilized the intensity gradient at the free surface, and an initial estimate of the approximate center and radius of the cylindrical specimen [91]. This region was enhanced by mapping the intensity values from a range of 0 to 1 into a range of 0.4 to 0.9, converted to a binary image using a threshold of 0.655 of the median normalized intensity of the image (which accounts for X-ray energy fluctuations), dilated by a disk structural element with a radius of 4 pixels, and finally adjusted to fill any holes in the edge region [91].

Through analysis of the 3D tomography data from the unloaded state to $0.5\varepsilon_f$, six sites of damage initiation were found and were tracked throughout loading. Of the six total sites of damage initiation, sites numbered 1-5 were associated with micro-void

nucleation, and site 6 exhibited early debonding, all shown in Figure 5.2. A region of interest which contained damage initiation sites 4-6 (blue box in Figure 5.2B) was chosen for the damage progression analysis because it was experimentally observed to (1) contain coalescence of all three damage initiation sites between $0.5\varepsilon_f$ and $0.85\varepsilon_f$, (2) led to the formation of the largest void at $0.85\varepsilon_f$ which also reached the free surface, and (3) eventually led to catastrophic failure (outlined in red in Figure 5.1C just before fracture). This smaller region of interest within the ductile fracture zone is shown at the unloaded state, $0.5\varepsilon_f$, and $0.85\varepsilon_f$ (through 6 face 2D cross-correlation tracking) in Figure 5.3A, B, and C, respectively.

5.2.4 Simulation Details

The experimental post-processing procedures were used to also instantiate a 3D model of the exact microstructure in the region of interest at $0.5\varepsilon_f$ (after damage initiated but before it progressed and coalesced) which includes the free surface shown in Figure 5.3D, the fibers shown in Figure 5.3E, as well as pores and nucleated microvoids shown in Figure 5.3F.

Prior to meshing the microstructure, each voxel which corresponded to a void in the material was removed in ParaView, and the remaining voxels were meshed using tetrahedral elements directly from the voxelated microstructure which results in tetrahedral elements with ideal and uniform geometry [91]. This meshing procedure was conducted in ParaView, and resulted in perfect bonding between the fibers and the matrix, which has been shown to be accurate for fiber reinforced thermoplastics where the fibers have been pre-treated [74, 91]. The meshed fiber elements were assigned linear elastic properties with an elastic modulus of 72.4 GPa and a Poisson's ratio of 0.2 [84, 85]. The meshed matrix elements were simulated to include nonlinear plasticity through a multilinear isotropic hardening model based on experimental and simulation data in Ref. [86].

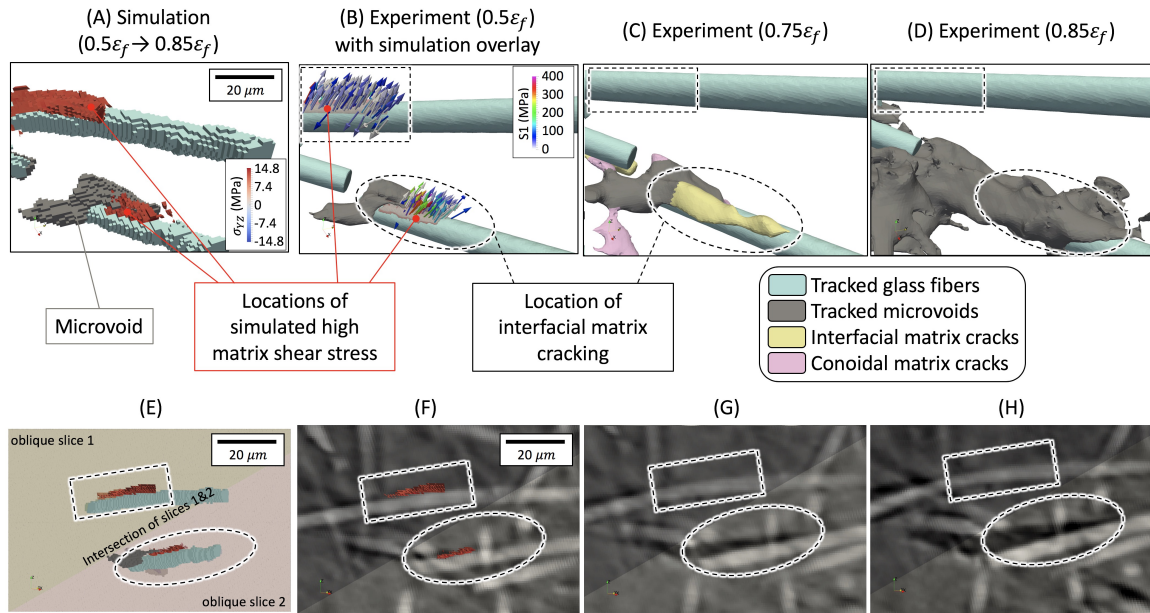


Figure 5.4. The coupled simulation and experiment results, where (A) shows the simulation result with the 99th percentile matrix shear stress (YZ) overlaid, (B) shows the coupled simulation and experiment at 0.5 ϵ_f with the simulated maximum principal stress overlaid, and (C) and (D) show the 3D experimental results at 0.75 ϵ_f and 0.85 ϵ_f , respectively. A different view of the same data with intersecting oblique planes (in order to capture both events which do not occur in the same plane) is shown in (E), with the corresponding tomography images at those planes shown in (F), (G), and (H) at 0.5 ϵ_f , 0.75 ϵ_f , and 0.85 ϵ_f , respectively, where the dashed box contains the region of high shear stress that did not lead to damage, and the dashed circle contains the region of high shear stress emanating from a micro-void which led to damage progression.

The experimental six face cross-correlation used to track the exact volume of tomography images between the unloaded state and $0.85\varepsilon_f$ was used to apply boundary conditions to the meshed microstructure at $0.5\varepsilon_f$. This corresponded to roller boundary conditions on the +X, -Y, and -Z surfaces, and displacement boundary conditions of $9.7\ \mu m$ on the -X surface, $-5.2\ \mu m$ on the +Y surface, and $20\ \mu m$ on the +Z surface. The simulation contained approximately 7.42 million elements, and was solved using Abaqus on 160 parallel processors and 512 GB of memory in 35 hours.

In the analysis of the simulation, hydrostatic stress was computed by

$$\sigma_{hyd} = \frac{\sigma_{xx} + \sigma_{yy} + \sigma_{zz}}{3} \quad (5.1)$$

and the maximum principal stress was computed by solving the eigenvalue problem

$$[\sigma_{ji} - \lambda\delta_{ij}]^T \hat{n}_j = 0 \quad (5.2)$$

where σ_{ji} is the stress tensor, δ_{ij} is the Kronecker delta, λ_1 , λ_2 , and λ_3 are the principal stresses (eigenvalues) and \hat{n}_1 , \hat{n}_2 , and \hat{n}_3 are the principal directions (eigenvectors) for the principal stresses, respectively. The maximum principal stress, S_1 , was then computed by $\max(\lambda_1, \lambda_2, \lambda_3)$ and the direction of maximum principal stress was the corresponding eigenvector. The computations were conducted element by element in MATLAB, and all visualizations of the simulation results were conducted in ParaView.

5.3 Results and Discussion

Using the microstructural data at the unloaded state, it was found that the average weight based fiber length is approximately $300\ \mu m$ and that fibers are moderately aligned with the loading direction forming an average angle of 40.4° with the Z axes [15,28]. From the time-lapse *in-situ* tomography data, it was found that damage initiation sites 4, 5, and 6 (Figure 5.2) coalesced into a large void that reached the

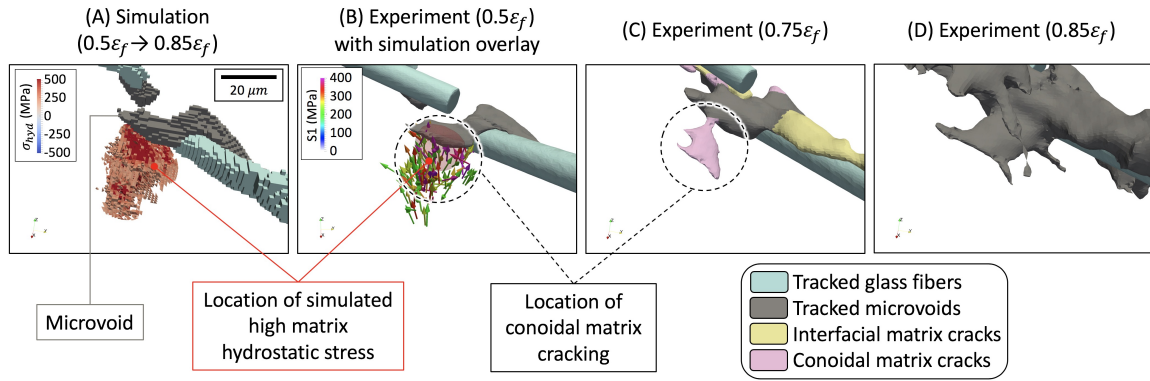


Figure 5.5. The coupled simulation and experiment results, where (A) shows the simulation result with the 99th percentile matrix hydrostatic stress overlaid, (B) shows the coupled simulation and experiment at $0.5\epsilon_f$ with the simulated maximum principal stress overlaid, and (C) and (D) show the 3D experimental results at $0.75\epsilon_f$ and $0.85\epsilon_f$, respectively.

free surface. The experimental analysis, which tracked the microstructure as damage propagated, revealed that coalescence either occurred through interfacial matrix cracking along a fiber edge, or conoidal matrix cracking, and appeared to emanate from sites of damage initiation, not from existing manufacturing pores in the region of interest. Additionally, an unlikely event of longitudinal fiber breakage of an in-plane fiber was documented within the ductile fracture zone and was observed to occur between $0.75\epsilon_f$ and $0.85\epsilon_f$.

5.3.1 Interfacial Matrix Cracking

Experimentally, portions of the damage profile were determined to be interfacial matrix cracking along a fiber edge if the damage exhibited an elongated shape and was along the edge of a fiber, as determined by 3D visualization and oblique slicing of the tomography data in ParaView. The simulation of the region of interest revealed that there were certain fiber-matrix interface regions which experienced very high matrix shear stress (99th percentile), as shown in Figure 5.4A. Specifically, this was found to

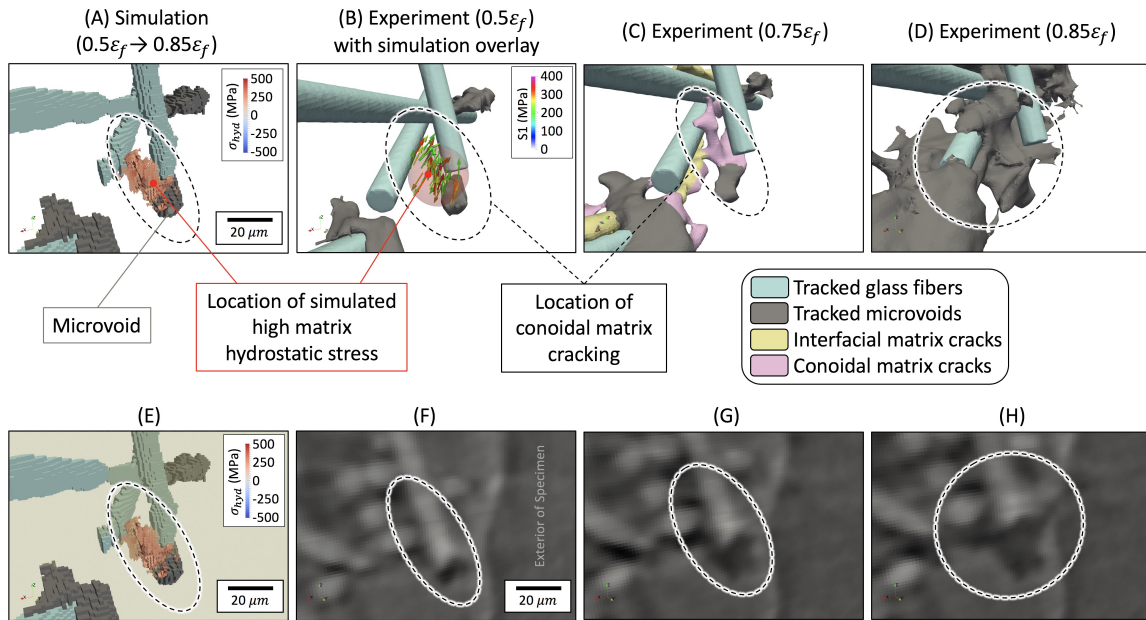


Figure 5.6. The coupled simulation and experiment results, where (A) shows the simulation result with the 99th percentile matrix hydrostatic stress overlaid, (B) shows the coupled simulation and experiment at $0.5\epsilon_f$ with the simulated maximum principal stress overlaid, and (C) and (D) show the 3D experimental results at $0.75\epsilon_f$ and $0.85\epsilon_f$, respectively. A view of the same data with an intersecting plane is shown in (E), with the corresponding tomography image at that plane shown in (F), (G), and (H) at $0.5\epsilon_f$, $0.75\epsilon_f$, and $0.85\epsilon_f$, respectively.

be the case for shear stress in the YZ, σ_{YZ} , due to the boundary conditions discussed in Section 5.2.4 which imposed the largest compression along the X direction leading to high shear activity in the YZ plane. In order to ensure this was not a mesh effect, only agglomerations of matrix elements along the edge of a fiber (which met the high shear stress criteria) were considered.

The analysis found a few agglomerations of high matrix shear stress along fibers. Consider the bottom fiber shown in Figure 5.4A, which is a misaligned fiber forming an 80° angle with the loading axes. A region of matrix material along this fiber contained 866 agglomerated matrix elements all within the 99th percentile of matrix σ_{YZ} . Experimentally, this same region was observed to contain interfacial cracking, shown circled in Figure 5.4B-H.

However, not all matrix regions of high shear stress along misaligned fibers led to interfacial cracking. This can be seen in the top fiber shown in Figure 5.4A, which is also a misaligned fiber, forming an 85° angle with the loading axes. A region of matrix material along this fiber contained 4950 agglomerated elements all within the 99th percentile of matrix σ_{YZ} , but in this case did not result in interfacial matrix cracking as can be seen outlined in a square in Figure 5.4B-H.

One of the main differences between the lower case which led to interfacial cracking (circled) and the upper case which did not lead to interfacial cracking (boxed), as shown in Figure 5.4, is that the region of high shear stress that led to interfacial cracking was emanating from a micro-void in the material (damage initiation site 4 in Figure 5.2). The presence of the micro-void increased the maximum principal stress, S1, in the matrix along the fiber edge, as shown circled in Figure 5.4B (where the arrows represent the directions of S1), which instigated the matrix cracking along the lower fiber.

This can be contrasted to the upper case of high matrix shear stress which was not emanating from an existing micro-void and experienced relatively lower values of matrix maximum principal stress along the interface. This region of isolated high shear stress did not contain signs of damage shown in Figure 5.4D and H, while the

region of high shear stress emanating from a micro-void led to continued interfacial matrix cracking along the lower fiber edge, leading to coalescence of all three sites of damage by $0.85\varepsilon_f$.

5.3.2 Conoidal Matrix Cracking

Another active mechanism during damage propagation that was observed experimentally was matrix driven conoidal cracking. The damage profile was characterized as matrix conoidal cracking (through 3D analysis and oblique slicing of the tomography data in ParaView) if it appeared that the crack grew in a conoidal shape, and not necessarily along an interface of a fiber edge, but in a tortuous manner through the fibrous microstructure.

One location within the microstructure that exhibited conoidal matrix cracking was also connected to the micro-void at the lower fiber discussed in Section 5.3.1 near damage initiation site 4. The results of the simulation in this region contained 4038 agglomerated matrix elements all experiencing high hydrostatic stress (99th percentile of hydrostatic stress in the matrix), as shown in Figure 5.5A. This agglomeration of matrix elements, while in close proximity to other fibers, was not along the edge of a fiber.

Instead, these matrix elements with high hydrostatic stress were emanating from the micro-void, and therefore, these elements were also experiencing high maximum principal stress, as shown in Figure 5.5B. Experimentally, this same region showed evidence of conoidal matrix cracking which occurred by $0.75\varepsilon_f$ as shown in Figure 5.5C, and by $0.85\varepsilon_f$ coalesced into one void shown in Figure 5.5D. This experimental analysis shows that matrix cracking can behave in a fiber-avoidance mode sub-surface, corroborating previous observations made using surface measurement techniques; the coupled simulation shows that it is related to hydrostatic stress emanating from a micro-void.

Another location within the microstructure that exhibited conoidal matrix cracking is shown in Figure 5.6A and 5.6B. This location, labeled as site 5 in Figure 5.2, exhibited a complicated fiber microstructure with highly misaligned fibers interacting with well aligned fibers during damage propagation. The simulation revealed 1163 agglomerated matrix elements experiencing high matrix hydrostatic stress (99th percentile matrix hydrostatic stress) shown in Figure 5.6A and sliced in Figure 5.6E.

Similar to the previous conoidal matrix cracking case, this location was also emanating from a micro-void and experienced high maximum principal stress as shown in Figure 5.6B. By $0.75\varepsilon_f$, this region showed damage progression in the form of conoidal matrix cracking, which was part of the large coalesced void by $0.85\varepsilon_f$. This region was particularly interesting because it was very close to the free surface of the specimen shown in Figure 5.6F. By $0.85\varepsilon_f$, this location of damage coalesced with the other locations of damage described in this work, and reached the free surface eventually leading to catastrophic brittle failure as the ductile fracture zone eventually transitioned to brittle fracture [91].

5.3.3 Fiber Breakage

Fiber breakage in general has not been considered a common occurrence in short fiber thermoplastic composites. Furthermore, when observed, it is usually a transverse break of a well aligned fiber [21,91]. Out of the nearly 400 fibers in the ductile fracture zone, only one fiber breakage event occurred by $0.5\varepsilon_f$ (shown in Figure 5.2 at damage initiation site 2). This fiber was well aligned with the loading direction, forming a 17.6° angle with the loading direction, and broke via the more commonly expected transverse mode due to neighboring micro-void nucleation [91].

However, this analysis showed that between $0.5\varepsilon_f$ and $0.85\varepsilon_f$, five additional fibers broke, representing 1.5% of the total fibers in the ductile fracture zone. Of the five fiber breakage events that occurred between $0.5\varepsilon_f$ and $0.85\varepsilon_f$, four were transverse breaks of well aligned fibers, and one was a longitudinal break of an in-plane fiber.

The longitudinal break occurred at a fiber that was $241\ \mu\text{m}$ long and was aligned almost perpendicular to the loading axes, forming an angle of 86° with the loading direction (Z).

The longitudinal fiber break of the nearly in-plane fiber can be seen in Figure 5.7A, B, C, and D at the unloaded state, $0.5\varepsilon_f$, $0.75\varepsilon_f$, and $0.85\varepsilon_f$, respectively, where the longitudinal break can be observed at $0.85\varepsilon_f$. This occurrence is unexpected because even with a pre-treatment of the fiber surface (which promotes adhesion with the matrix), the polypropylene matrix material has a much lower ultimate strength than the E-glass fiber [84,86]. Therefore, the matrix near the interface would be expected to fail first.

The simulation result showed that this fiber experienced a high shear stress gradient shown in the insert of Figure 5.7B. Yet, this stress state was not unique to this fiber alone; almost all highly misaligned fibers in the microstructure were simulated to experience a similar shear stress gradient. Therefore, the longitudinal fiber break of this particular misaligned fiber was not only a result of its shear stress state, but was found to be a result of its morphology which was observed through a reconstruction of the exact fiber surface. Specifically, an in-depth surface reconstruction of the fiber showed that it was damaged at the unloaded state (Figure 5.8A) likely due to environmental damage of the E-glass fiber [44]. The damage can be seen in the tomography images at the oblique slices shown in Figure 5.8B, where tomography images in slice one, two, and five have been circled and clearly show that the fiber is damaged in the unloaded state. It is important to note that fiber damage is challenging to detect and can be missed when observing tomography images in the orthogonal Cartesian planes; sometimes it is necessary to view an accurate surface reconstruction of the fiber, or view tomography data at oblique angles to observe the true morphology of certain features.

Overall, for this in-plane fiber (that was highly misaligned with the loading direction), it was found that the fiber surface pre-treatment used to promote adhesion with the matrix was very effective because there were no signs of debonding in the

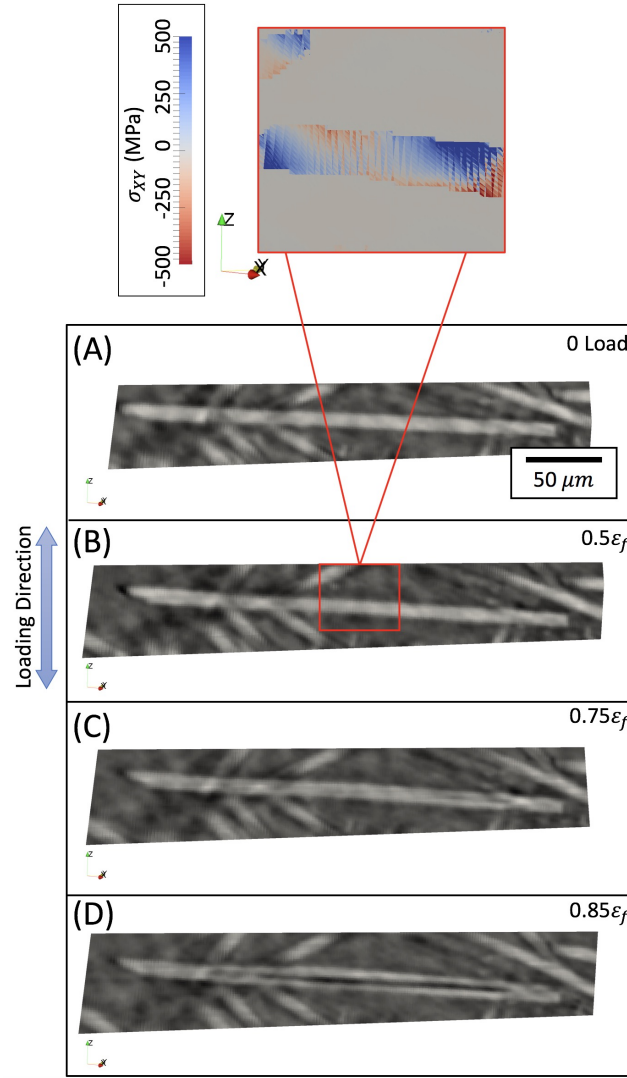


Figure 5.7. Experimental data of the damaged in-plane (XY plane) fiber shown at (A) the unloaded state, (B) $0.5\epsilon_f$, (C) $0.75\epsilon_f$, and (D) $0.85\epsilon_f$ where a longitudinal fiber breakage event has occurred, as well as an image of the simulated fiber experiencing a high shear stress gradient in its plane (XY plane).

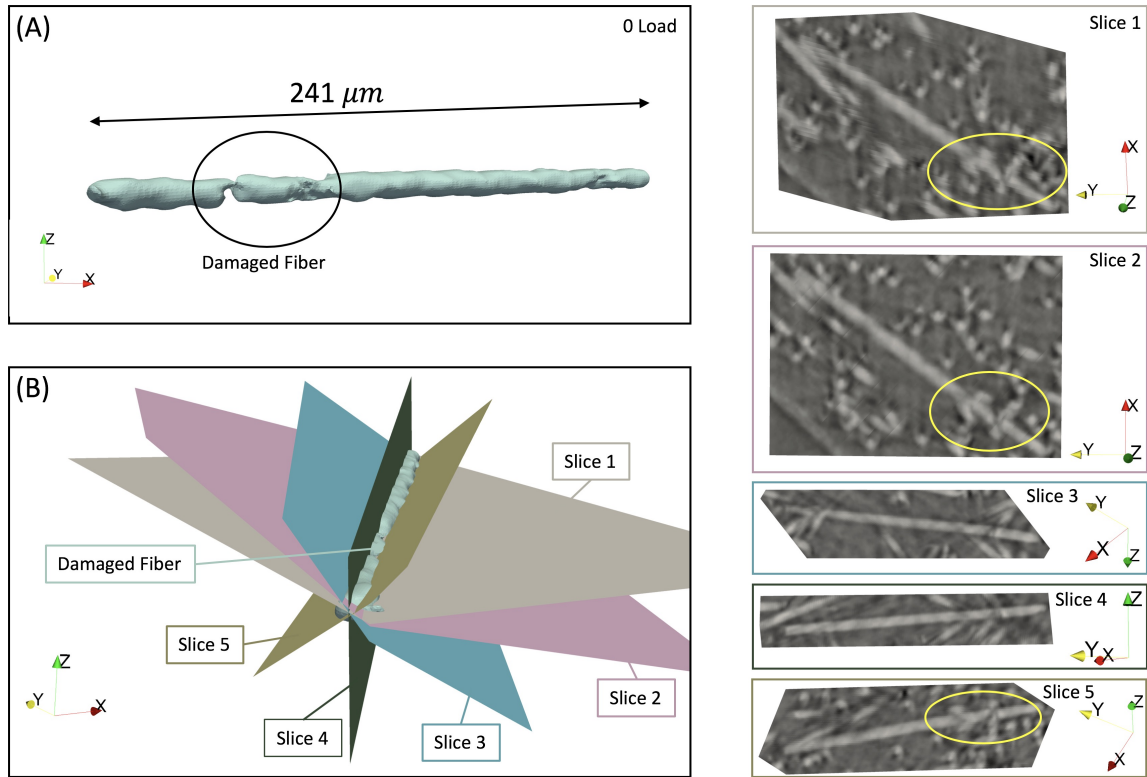


Figure 5.8. The experimental data rendered at the unloaded configuration of an in-plane fiber (A) which was damaged during the injection molding process as can be seen circled, with accompanying tomography images sectioned at the five planes described in (B), where it can be seen circled in Slices 1, 2, and 5 that neighboring fibers appeared to have applied force during injection molding leading to damage in the fiber at the unloaded state.

in-situ tomography images, as was seen in Figure 5.7. With a strong bond to the matrix, it is therefore hypothesized that the highly misaligned fiber broke longitudinally because (1) it was damaged at the unloaded state likely due to the injection molding fabrication, and (2) it experienced a high shear stress gradient between $0.5\varepsilon_f$ and $0.85\varepsilon_f$, as was shown in Figure 5.7D.

5.4 Conclusion

This work analyzed specific damage events that occurred in a short fiber reinforced thermoplastic. Specifically, the specimen studied in this work was an injection molded polypropylene that was reinforced with 30%, by weight, $10\ \mu m$ diameter E-glass fibers which were pre-treated to promote adhesion between the fibers and the matrix. The experiment was an incremental tension test that was conducted *in-situ* where X-ray μ -CT images were acquired at a total of 58 interruptions between the unloaded state and failure, which occurred at 5.77% macroscopic strain (computed through digital image correlation of the speckled surface of the specimen during the *in-situ* experiment).

Analysis of the 3D tomography images was conducted to determine the ductile fracture zone just before brittle fracture occurred. Through 2D image correlation, the ductile fracture zone was traced back to the microstructure at the unloaded state. The progression of the microstructure was then studied in detail using a total of three detection procedures: fiber detection, void detection, and specimen edge detection. The 3D analysis revealed the exact locations of damage initiation within the ductile fracture zone, which were observed to occur by $0.5\varepsilon_f$. There were six independent sites of damage initiation: one site of micro-void nucleation coupled with fiber breakage [91], four sites of micro-void nucleation at fiber tips [91], and one site of debonding of a highly misaligned fiber which occurred likely as a result of low adhesion with the matrix (since it was observed early in the loading sequence).

Three of the six total locations of damage initiation (two micro-void nucleation sites and the one debonding location) were experimentally observed to coalesce into one connected void which reached the free surface by $0.85\varepsilon_f$ through either fiber-interface matrix cracking or conoidal matrix cracking. To understand the complex growth of cracking which caused large coalescence in the three sites of damage, a FEM simulation was conducted of the exact local microstructure as extracted through the three detection techniques described in this work. This region within the ductile fracture zone had a volume of 117 by 176.8 by 183.3 μm , and was tracked throughout the experimental loading history using six face 2D cross-correlation. The 3D simulation of this region of interest, which contained 89 tracked fibers and 7.42 million elements, was conducted to replicate the experimental boundary conditions experienced by the region.

The coupled experimental and simulation analysis revealed that high shear stress along a fiber edge does not necessarily result in interfacial matrix cracking, but that high shear stress along a fiber edge that is also emanating from a site of micro-void nucleation results in interfacial matrix cracking. Furthermore, the analysis showed that conoidal matrix cracking was found at locations of high hydrostatic stress emanating from sites of micro-void nucleation. Additionally, five fiber breakage events were experimentally documented: four typical transverse fiber breakage events of well aligned fibers, and one unlikely longitudinal fiber breakage event of a highly misaligned fiber. The longitudinal fiber breakage event was further examined by extracting the exact morphology of the fiber at the unloaded state, which revealed that the fiber was damaged during the injection molding process, which likely led to its unexpected fracture behavior.

Overall, this work has provided clarity into the 3D damage propagation events of short fiber reinforced thermoplastics by providing insight into the physical phenomena that govern their micromechanical behavior. This includes the role of shear stress and hydrostatic stress in the evolution of micro-voids which nucleated during damage initiation. Specifically, using the criteria of high shear stress at the presence

of a nucleated micro-void with relatively high maximum principal stress, the path of interfacial matrix cracking can be predicted. Additionally, using localized high hydrostatic stress near a nucleated micro-void coupled with high maximum principal stress, conoidal matrix cracking behavior can also be predicted. This understanding will allow engineers to increase their predictive capabilities of the mechanical response of these materials past the elastic regime and well into the damage propagation regimes, and eventually towards strength predictions and robust material qualification.

6. CONCLUSIONS

This work focused on studying the microstructural behavior of a short fiber reinforced thermoplastic. Specifically, the material studied in this work was an injection molded polypropylene that was reinforced with 30%, by weight, 10 μm diameter E-glass fibers which were pre-treated to promote adhesion between the fibers and the matrix. The first major contribution of this work was a MATLAB based image processing tool that was created and is available for free download. The tool, named ModLayer, provides the capability of viewing successive slices of a reference 3D image and an adjustable 3D image, and allows for comprehensive microstructural feature detection. This tool is especially useful in correcting the multi-class segmentation of features that may arise from noise or erroneous artifacts in imaging techniques which are often too difficult to capture through standard automatic segmentation procedures. Using automated image processing algorithms and ModLayer, the microstructure of three total specimens were analyzed in this work. Two specimens were analyzed in order to compare microstructural characterization techniques, and one specimen was tested *in-situ* to study microstructural damage initiation and propagation behavior.

The first phase of this project focused on comparing non-destructive X-ray tomography with destructive optical microscopy for their capabilities in detecting microstructural features. The X-ray tomography images were acquired at Argonne National Laboratory using synchrotron X-rays. The 3D image set was then analyzed for fiber volume fraction, fiber orientation distribution, fiber length distributions, as well porosity volume fraction. Destructively, the specimen was analyzed by sectioning, mounting in acrylic, successively polishing, and plasma etching. This allowed for a direct comparison between X-ray tomography and optical microscopy for porosity volume fraction, fiber volume fraction, and fiber orientation distribution. Since sectioning and mounting the specimen cuts through the fibers, a separate specimen

was destructively analyzed for a statistical comparison of the fiber length distribution through a matrix burn-off technique.

The characterization analysis revealed that using X-ray μ -CT and optical microscopy results in fiber volume fraction computations that match well. On the other hand, the porosity volume fraction detected destructively was slightly lower than that which was detected in the μ -CT images due to pores smaller than $700 \mu m^3$ (equivalent to spherical pores with radii less than $5.5 \mu m$) being filled in with polymer during polishing. For fiber orientation distributions, the A_{ij} fiber orientation distribution determined non-destructively and destructively matched fairly well (differing no more than 6° on average with respect to each Cartesian coordinate axes) with the non-destructive approach reporting a slightly higher alignment due to its ability to capture curvatures of 3D fibers in the injection molding flow direction. The average fiber length computed non-destructively and destructively matched within $13.8 \mu m$. This phase of the project contributed necessary information for engineers and researchers to identify the advantages/disadvantages of both approaches and understand the quantitative differences in microstructural characterization when using each method in order to confidently qualify composite materials.

The second phase of the project focused on analyzing damage initiation behavior through a coupled experiment and simulation analysis that was conducted on a pristine glass fiber reinforced polypropylene specimen. Specifically, the experiment was an incremental tension test that was conducted *in-situ* where X-ray μ -CT images were acquired at a total of 58 interruptions between the unloaded state and failure, which occurred at 5.77% macroscopic strain (computed through digital image correlation of the speckled surface of the specimen during the *in-situ* experiment). By analyzing the microstructure at the unloaded state, 30%, and 50% of macroscopic failure, locations of damage initiation were found and analyzed.

Experimentally during damage initiation, it was found that large porosity manufacturing defects do not consistently play a role in initiating and propagating damage, and that additional microstructural features, like T-type configurations and overlap-

ping fiber tips, play a critical role in the microstructure's overall resistance to damage initiation. A high fidelity model (comprised of 44.5 million elements) was created of a sub-region within the ductile fracture zone, in which 368 fibers were instantiated. The results of the coupled simulation analysis showed that the 5 experimentally observed locations of micro-void nucleation corresponded with the 5 highest regions of hydrostatic stress, which substantiates the use of the hydrostatic stress metric to explain and predict micro-void nucleation in the microstructure of fiber reinforced thermoplastic composites, proving a long standing hypothesis of the role of stress tri-axiality in damage initiation for thermoplastic matrix composites. Additionally, this work showed that although small fragments of fibers, which are almost negligible in size compared to the average fiber length, can be ignored during elastic mechanical property predictions, they must be included in the damage initiation and strength predictions of these composites.

Lastly, the third phase of the project focused on analyzing damage propagation via matrix cracking through another coupled simulation. Experimentally, regions of matrix cracking were segmented into either interfacial matrix cracking or conoidal matrix cracking (sometimes referred to as fiber-avoidance cracking) by analyzing the microstructure at 50%, 75%, and 85% of the macroscopic strain to failure. The coupled simulation analysis revealed that high shear stress along a fiber edge that is also emanating from a site of micro-void nucleation results in interfacial matrix cracking. Furthermore, the analysis showed that conoidal matrix cracking was found at locations of high hydrostatic stress emanating from sites of micro-void nucleation. Separately, a longitudinal fiber breakage event was examined by extracting the exact morphology of the fiber at the unloaded state, which revealed that the fiber was damaged during the injection molding process, which likely led to its unexpected fracture behavior.

Overall, this work has provided clarity into the 3D damage initiation and propagation events of short fiber reinforced thermoplastics by providing insight into the physical phenomena that govern their micromechanical behavior. Using these results,

locations of micro-void nucleation within the microstructure can now be predicted, and the propagation of these micro-voids through different forms of matrix cracking which leads to catastrophic failure can also be predicted. This understanding will allow engineers to increase their predictive capabilities of the mechanical response of these materials past the elastic regime and well into the damage propagation regimes, and eventually towards strength predictions and robust material qualification. By doing so, component level testing can be supplemented by computer simulations. For example, this can be done without necessarily conducting X-ray μ -CT. Consider the fact that there currently exist commercial tools which can simulate the injection molding process and predict the microstructure of a final injection molded part [47, 90]. Small perturbations within the microstructure due to injection molding variability can also be simulated, and the resultant microstructures can be used to supplement large scale component-level testing using the criteria that was determined in this work through the coupled experiments and simulations. The four major research contributions of this work (image processing tool development, comprehensive characterization of the microstructure, the role of hydrostatic stress in damage initiation, and the roles of shear and hydrostatic stress in damage propagation) bring scientists and engineers four steps closer to high accuracy strength prediction and low cost qualification of discontinuous fiber reinforced thermoplastic composites.

REFERENCES

- [1] J. Cassar, M. Galea, R. Grima, K. Stroud, and A. Torpiano. Shelters over the Megalithic Temples of Malta: Debate, design and implementation. *Environmental Earth Sciences*, 63(7):1849–1860, 2011.
- [2] A. Moropoulou, A. Bakolas, and S. Anagnostopoulou. Composite materials in ancient structures. *Cement and Concrete Composites*, 27(2):295–300, 2005.
- [3] Jeffrey Wadsworth and Donald R. Lesuer. Ancient and modern laminated composites - From the Great Pyramid of Gizeh to Y2K. *Materials Characterization*, 45(4-5):289–313, 2000.
- [4] Hal F. Brinson and L. Catherine Brinson. *Polymer Engineering Science and Viscoelasticity*. Springer US, Boston, MA, 2015.
- [5] Morris A. Steinberg. MATERIALS FOR AEROSPACE. *Scientific American*, 255(4):67–72, 1986.
- [6] Jeff Fraga. Boeing 787 from the Ground Up. *AERO Magazine*, pages 17–23, 2006.
- [7] Andrew McIntosh. 18 billion pounds of fuel saved: Boeing releases new Dreamliner data, 10 2017.
- [8] Eric N. Landis and Denis T. Keane. X-ray microtomography. *Materials Characterization*, 61(12):1305–1316, 2010.
- [9] T. L. Burnett, S. A. McDonald, A. Gholinia, R. Geurts, M. Janus, T. Slater, S. J. Haigh, C. Ornek, F. Almuaili, D. L. Engelberg, G. E. Thompson, and P. J. Withers. Correlative tomography. *Scientific Reports*, 4:1–6, 2014.
- [10] John C. Russ and F. Brent Neal. *The Image Processing Handbook*. CRC Press, 9 2016.
- [11] Jianbo Shi and Jitendra Malik. Normalized Cuts and Image Segmentation Part of the Electrical and Computer Engineering Commons Recommended Citation Normalized Cuts and Image Segmentation Normalized Cuts and Image Segmentation. *IEEE Transactions on Pattern Analysis and Machine Intelligence*, 22(8):888–905, 2000.
- [12] V. Vaithyanathan and U. Rajappa. A review on clustering techniques in image segmentation. *International Journal of Applied Engineering Research*, 8(20 SPEC. ISSUE):2685–2688, 2013.
- [13] John M Sosa, Daniel E Huber, Brian Welk, and Hamish L Fraser. Development and application of MIPAR: a novel software package for two- and three-dimensional microstructural characterization. *Integrating Materials and Manufacturing Innovation*, 3(1):1–18, 2014.

- [14] Chris Solomon and Toby Breckon. *Fundamentals of Digital Image Processing: A practical approach with examples in Matlab*. John Wiley & Sons, 2011.
- [15] Imad Hanhan, Ronald Agyei, Xianghui Xiao, and Michael D. Sangid. Comparing non-destructive 3D X-ray computed tomography with destructive optical microscopy for microstructural characterization of fiber reinforced composites. *Composites Science and Technology*, 184:107843, 11 2019.
- [16] Michael D Abràmoff, Paulo J Magalhães, and Sunanda J Ram. Image processing with ImageJ. *Biophotonics international*, 11(7):36–42, 2004.
- [17] E. Maire and P. J. Withers. Quantitative X-ray tomography. *International Materials Reviews*, 59(1):1–43, 2014.
- [18] Ying Wang, Lars P. Mikkelsen, Grzegorz Pyka, and Philip J. Withers. Time-lapse helical X-ray computed tomography (CT) study of tensile fatigue damage formation in composites for wind turbine blades. *Materials*, 11(11), 2018.
- [19] A. E. Scott, M. Mavrogordato, P. Wright, I. Sinclair, and S. M. Spearing. In situ fibre fracture measurement in carbon-epoxy laminates using high resolution computed tomography. *Composites Science and Technology*, 71(12):1471–1477, 2011.
- [20] Brian M. Patterson, Nikolaus L. Cordes, Kevin Henderson, Jason J. Williams, Tyler Stannard, Sudhanshu S. Singh, Angel Rodriguez Ovejero, Xianghui Xiao, Mathew Robinson, and Nikhilesh Chawla. In situ X-ray synchrotron tomographic imaging during the compression of hyper-elastic polymeric materials. *Journal of Materials Science*, 51(1):171–187, 2015.
- [21] H. Rolland, N. Saintier, and G. Robert. Damage mechanisms in short glass fibre reinforced thermoplastic during in situ microtomography tensile tests. *Composites Part B: Engineering*, 90:365–377, 2016.
- [22] S. H. McGee and R. L. McCullough. Characterization of fiber orientation in short-fiber composites. *Journal of Applied Physics*, 55(5):1394–1403, 1984.
- [23] B Mlekusch. Thermoelastic properties of short-fibre-reinforced thermoplastics. *Composites Science and Technology*, 59(6):911–923, 5 1999.
- [24] Luc Avérous, Jean C Quantin, Dominique Lafon, and Alain Crespy. Determination of 3D fiber orientations in reinforced thermoplastics, using scanning electron microscopy. *Acta Stereologica*, 1995.
- [25] Randy S. Bay and Charles L. Tucker. Stereological measurement and error estimates for three-dimensional fiber orientation. *Polymer Engineering & Science*, 32(4):240–253, 1992.
- [26] Bhisham N. Sharma, Seth A. Kijewski, Leonard S. Fifield, Yongsoon Shin, Charles L. Tucker, and Michael D. Sangid. Reliability in the characterization of fiber length distributions of injection molded long carbon fiber composites. *Polymer Composites*, 39(12):4594–4604, 2018.
- [27] Bhisham N Sharma, Diwakar Naragani, Ba Nghiep Nguyen, Charles L Tucker, and Michael D Sangid. Uncertainty quantification of fiber orientation distribution measurements for long-fiber-reinforced thermoplastic composites. *Journal of Composite Materials*, page 002199831773353, 2017.

- [28] Ronald F. Agyei and Michael D. Sangid. A supervised iterative approach to 3D microstructure reconstruction from acquired tomographic data of heterogeneous fibrous systems. *Composite Structures*, 206(August):234–246, 2018.
- [29] Monica Jane Emerson, Vedrana Andersen Dahl, Knut Conradsen, Lars Pilgaard Mikkelsen, and Anders Bjorholm Dahl. Statistical validation of individual fibre segmentation from tomograms and microscopy. *Composites Science and Technology*, 160(January):208–215, 2018.
- [30] C. Q. Bowles and J. Schijve. The role of inclusions in fatigue crack initiation in an aluminum alloy. *International Journal of Fracture*, 9(2):171–179, 6 1973.
- [31] Stephen T. Carter, John Rotella, Ronald F. Agyei, Xiaghui Xiao, and Michael D. Sangid. Measuring fatigue crack deflections via cracking of constituent particles in AA7050 via in situ x-ray synchrotron-based microtomography. *International Journal of Fatigue*, 116(May):490–504, 2018.
- [32] Karthik Ramani, Dave Bank, and Nick Kraemer. Effect of screw design on fiber damage in extrusion compounding and composite properties. *Polymer Composites*, 16(3):258–266, 1995.
- [33] R Bailey and H Kraft. A study of fibre attrition in the processing of long fibre reinforced thermoplastics. *International Polymer Processing*, 2(2):94–101, 1987.
- [34] K. Stade. Techniques for compounding glass fiber-reinforced thermoplastics. *Polymer Engineering & Science*, 17(1):50–57, 1977.
- [35] David Wall. Co-Rotating Twin Screw Extruders. *Polymer Composites*, 70(2), 1989.
- [36] J. L. Kardos and J. C. Halpin. Short predicting the strength and toughness of fiber composites. *Macromolecular Symposia*, 153(1):139–153, 1999.
- [37] R. Byron Pipes, Roy L. McCullough, and David G. Taggart. Behavior of discontinuous fiber composites: Fiber orientation. *Polymer Composites*, 3(1):34–39, 1982.
- [38] Mahesh Gupta and K. K. Wang. Fiber orientation and mechanical properties of short-fiber-reinforced injection-molded composites: Simulated and experimental results. *Polymer Composites*, 14(5):367–382, 1993.
- [39] A Vaxman, M Narkis, A Siegmann, and S Kenig. Short-fiber-reinforced thermoplastics. Part III: Effect of fiber length on rheological properties and fiber orientation. *Polymer Composites*, 10(6):454–462, 12 1989.
- [40] Shao Y. Fu and Bernd Lauke. Effects of fiber length and fiber orientation distributions on the tensile strength of short-fiber-reinforced polymers. *Composites Science and Technology*, 56(10):1179–1190, 1996.
- [41] Mark P. Connolly. The Measurement of Porosity in Composite Materials Using Infrared Thermography. *Journal of Reinforced Plastics and Composites*, 11(December):1367–1375, 1992.
- [42] Usha Martin. Integrated Process, 2015.

- [43] Gregorio M. Vélez-García, Peter Wapperom, Donald G. Baird, Alex O. Aning, and Vlastimil Kunc. Unambiguous orientation in short fiber composites over small sampling area in a center-gated disk. *Composites Part A: Applied Science and Manufacturing*, 43(1):104–113, 2012.
- [44] Ulku Yilmazer and Murat Cansever. Effects of processing conditions on the fiber length distribution and mechanical properties of glass fiber reinforced nylon-6. *Polymer Composites*, 23(1):61–71, 2002.
- [45] Ba Nghiep Nguyen, Satish K. Bapanapalli, James D. Holbery, Mark T. Smith, Vlastimil Kunc, Barbara J. Frame, Jay H. Phelps, and Charles L. Tucker. Fiber length and orientation in long-fiber injection-molded thermoplastics - Part I: Modeling of microstructure and elastic properties. *Journal of Composite Materials*, 42(10):1003–1029, 2008.
- [46] S. Y. Fu, B. Lauke, E. Mäder, C. Y. Yue, and X. Hu. Tensile properties of short-glass-fiber- and short-carbon-fiber-reinforced polypropylene composites. *Composites Part A: Applied Science and Manufacturing*, 31(10):1117–1125, 2000.
- [47] Jay H. Phelps, Ahmed I. Abd El-Rahman, Vlastimil Kunc, and Charles L. Tucker. A model for fiber length attrition in injection-molded long-fiber composites. *Composites Part A: Applied Science and Manufacturing*, 51:11–21, 2013.
- [48] Munehiro Kawamura, Satoshi Ikeda, Satoru Morita, and Yukio Sanomura. Unambiguous determination of 3D fiber orientation distribution in thermoplastic composites using SAM image of elliptical mark and interference fringe. *Journal of Composite Materials*, 39(4):287–299, 2005.
- [49] Yong Lee, Seok Lee, Jae Youn, Kwansoo Chung, and Tae Kang. Characterization of fiber orientation in short fiber reinforced composites with an image processing technique. *Materials Research Innovations*, 6(2):65–72, 2002.
- [50] N. C. Davidson, A. R. Clarke, and G. Archenhold. Large-area, high-resolution image analysis of composite materials. *Journal of Microscopy*, 185(2):233–242, 1997.
- [51] Jérôme Lux, Christine Delisée, and Xavier Thibault. 3D Characterization of Wood Based Fibrous Materials: an Application. *Image Analysis & Stereology*, 25(1):25, 2011.
- [52] Muhammad Tausif, Brian Duffy, Sergei Grishanov, Hamish Carr, and Stephen J. Russell. Three-dimensional fiber segment orientation distribution using X-ray microtomography. *Microscopy and Microanalysis*, 20(4):1294–1303, 2014.
- [53] Hellen Altendorf and Dominique Jeulin. 3D directional mathematical morphology for analysis of fiber orientations. *Image Analysis and Stereology*, 28(3):143–153, 2009.
- [54] F. Malmberg, J. Lindblad, C. Östlund, K. M. Almgren, and E. K. Gamstedt. Measurement of fibre-fibre contact in three-dimensional images of fibrous materials obtained from X-ray synchrotron microtomography. *Nuclear Instruments and Methods in Physics Research, Section A: Accelerators, Spectrometers, Detectors and Associated Equipment*, 637(1):143–148, 2011.

- [55] Hongbin Shen, Steven Nutt, and David Hull. Direct observation and measurement of fiber architecture in short fiber-polymer composite foam through micro-CT imaging. *Composites Science and Technology*, 64(13-14):2113–2120, 2004.
- [56] S. C. Garcea, Y. Wang, and P. J. Withers. X-ray computed tomography of polymer composites. *Composites Science and Technology*, 156:305–319, 2018.
- [57] Monica Jane Emerson, Ying Wang, Philip John Withers, Knut Conradsen, Anders Bjorholm Dahl, and Vedrana Andersen Dahl. Quantifying fibre re-orientation during axial compression of a composite through time-lapse X-ray imaging and individual fibre tracking. *Composites Science and Technology*, 168(August):47–54, 2018.
- [58] A. Bernasconi, F. Cosmi, and P. J. Hine. Analysis of fibre orientation distribution in short fibre reinforced polymers: A comparison between optical and tomographic methods. *Composites Science and Technology*, 72(16):2002–2008, 2012.
- [59] S.G Advani and C.L. Tucker III. The Use of Tensors to Describe and Predict Fiber Orientation in Short Fiber Composites. *Journal of Rheology*, 31(8):751–784, 1987.
- [60] P. J. Hine, N. Davidson, R. A. Duckett, A. R. Clarke, and I. M. Ward. Hydrostatically extruded glass-fiber-reinforced polyoxymethylene. I: The development of fiber and matrix orientation. *Polymer Composites*, 17(5):720–729, 1996.
- [61] Doğa Gürsoy, Francesco De Carlo, Xianghui Xiao, and Chris Jacobsen. TomoPy: A framework for the analysis of synchrotron tomographic data. *Journal of Synchrotron Radiation*, 21(5):1188–1193, 2014.
- [62] Ignacio Arganda-Carreras, Verena Kaynig, Curtis Rueden, Kevin W. Eliceiri, Johannes Schindelin, Albert Cardona, and H. Sebastian Seung. Trainable Weka Segmentation: A machine learning tool for microscopy pixel classification. *Bioinformatics*, 33(15):2424–2426, 2017.
- [63] V. Kunc, B. Frame, J. Pryor, B.N. Nguyen, C.L. Tucker III, S. Case, D. Penumadu, and E.W. Guffey. Techniques and results for fiber length distribution determination as a function of thickness in long fiber reinforced injection molded thermoplastics. *Oak Ridge National Laboratory (ORNL) Report*, 2008.
- [64] Petrus Hendrik Hermans. *Contribution to the physics of cellulose fibres*. Elsevier Publishing Company, Inc.; London, 1946.
- [65] C. G. Joung, N. Phan-Thien, and X. J. Fan. Viscosity of curved fibers in suspension. *Journal of Non-Newtonian Fluid Mechanics*, 102(1):1–17, 2002.
- [66] Satish Bapanapalli and Ba Nghiep Nguyen. Prediction of elastic properties for curved fiber polymer composites. *Polymer Composites*, 2008.
- [67] Charles L Tucker and Erwin Liang. Stiffness predictions for unidirectional short-fiber composites. *Composites Science and Technology*, 59, 1999.
- [68] J.D. Eshelby. The determination of the elastic field of an ellipsoidal inclusion, and related problems. *Proceedings of the Royal Society of London. Series A. Mathematical and Physical Sciences*, 241(1226):376–396, 8 1957.

- [69] A. Matzenmiller, J. Lubliner, and R.L. Taylor. A constitutive model for anisotropic damage in fiber-composites. *Mechanics of Materials*, 20(2):125–152, 1995.
- [70] S. Kammoun, I. Doghri, L. Adam, G. Robert, and L. Delannay. First pseudo-grain failure model for inelastic composites with misaligned short fibers. *Composites Part A: Applied Science and Manufacturing*, 42(12):1892–1902, 2011.
- [71] H. J. Böhm, A. Eckschlager, and W. Han. Multi-inclusion unit cell models for metal matrix composites with randomly oriented discontinuous reinforcements. *Computational Materials Science*, 25(1-2):42–53, 2002.
- [72] Xiaofang Hu, Jian Fang, Feng Xu, Bo Dong, Yu Xiao, and Luobin Wang. Real internal microstructure based key mechanism analysis on the micro-damage process of short fibre-reinforced composites. *Scientific Reports*, 6(September):1–9, 2016.
- [73] J. Modniks and J. Andersons. Modeling the non-linear deformation of a short-flax-fiber-reinforced polymer composite by orientation averaging. *Composites Part B: Engineering*, 54(1):188–193, 2013.
- [74] N. Sato, T. Kurauchi, S. Sato, and O. Kamigaito. Microfailure behaviour of randomly dispersed short fibre reinforced thermoplastic composites obtained by direct SEM observation. *Journal of Materials Science*, 26(14):3891–3898, 1991.
- [75] A. Bourmaud, G. Ausias, G. Lebrun, M. L. Tachon, and C. Baley. Observation of the structure of a composite polypropylene/flax and damage mechanisms under stress. *Industrial Crops and Products*, 43(1):225–236, 2013.
- [76] D. Notta-Cuvier, F. Lauro, and B. Bennani. Modelling of progressive fibre/matrix debonding in short-fibre reinforced composites up to failure. *International Journal of Solids and Structures*, 66:140–150, 2015.
- [77] D. Notta-Cuvier, F. Lauro, B. Bennani, and R. Balieu. Damage of short-fibre reinforced materials with anisotropy induced by complex fibres orientations. *Mechanics of Materials*, 68:193–206, 2014.
- [78] J L Chaboche. Continuum Damage Mechanics: Part II — Damage Growth, Crack Initiation, and Crack Growth. *Journal of Applied Mechanics*, 55(March 1988), 2014.
- [79] J. LLorca and J. Segurado. Three-dimensional multiparticle cell simulations of deformation and damage in sphere-reinforced composites. *Materials Science and Engineering A*, 365(1-2):267–274, 2004.
- [80] C. Tekoglu and T. Pardoen. A micromechanics based damage model for composite materials. *International Journal of Plasticity*, 26(4):549–569, 2010.
- [81] Karolina Martyniuk, Bent F. Sørensen, Peter Modregger, and Erik M. Lauridsen. 3D in situ observations of glass fibre/matrix interfacial debonding. *Composites Part A: Applied Science and Manufacturing*, 55:63–73, 2013.
- [82] E. Bar-Kochba, J. Toyjanova, E. Andrews, K. S. Kim, and C. Franck. A Fast Iterative Digital Volume Correlation Algorithm for Large Deformations. *Experimental Mechanics*, 55(1):261–274, 2015.

- [83] Imad Hanhan and Michael D. Sangid. ModLayer: A MATLAB GUI Drawing Segmentation Tool for Visualizing and Classifying 3D Data. *Integrating Materials and Manufacturing Innovation*, 8(0123456789):468–475, 11 2019.
- [84] Bhagwan D Agarwal, Lawrence J Broutman, and K Chandrashekhara. *Analysis and performance of fiber composites*. John Wiley & Sons, 1990.
- [85] Michael Bauccio. *ASM engineered materials reference book*. CRC, 1994.
- [86] Ehsan Mohammadpour, Mokhtar Awang, Saeid Kakooei, and Hazizan Md Akil. Modeling the tensile stress-strain response of carbon nanotube/polypropylene nanocomposites using nonlinear representative volume element. *Materials and Design*, 58:36–42, 2014.
- [87] Xiaosheng Gao and Jinkook Kim. Modeling of ductile fracture: Significance of void coalescence. *International Journal of Solids and Structures*, 43(20):6277–6293, 2006.
- [88] Rgio Frascino Mfiller de Almeida and Zabulon dos Santos Nogueira Neto. Effect of void content on the strength of composite laminates. *Composite Structures*, 28:139–148, 1994.
- [89] Fransisco Folgar and Charles L Tucker. Orientation Behavior of Fibers in Concentrated Suspensions. *Journal of Reinforced Plastics and Composites*, 3(2):98–119, 1984.
- [90] Jay H. Phelps and Charles L. Tucker. An anisotropic rotary diffusion model for fiber orientation in short- and long-fiber thermoplastics. *Journal of Non-Newtonian Fluid Mechanics*, 156(3):165–176, 2009.
- [91] Imad Hanhan, Ronald F. Agyei, Xianghui Xiao, and Michael D. Sangid. Predicting Microstructural Void Nucleation in Discontinuous Fiber Composites through Coupled in-situ X-ray Tomography Experiments and Simulations. *Scientific Reports*, 10(1):3564, 12 2020.
- [92] R Talreja. Damage Development In Composites: Mechanisms and Modelling. *Journal of Strain Analysis*, 24(4):215–222, 1989.
- [93] a.T. DiBenedetto. Tailoring of interfaces in glass fiber reinforced polymer composites: a review. *Materials Science and Engineering: A*, 302(1):74–82, 2001.
- [94] Shang-lin Gao and Edith Ma. Characterisation of interphase nanoscale property variations in glass fibre reinforced polypropylene and epoxy resin composites. *Composites*, 33:559–576, 2002.
- [95] Norio Sato, Toshio Kurauchi, Shigeyuki Sato, and Osami Kamigaito. Mechanism of fracture of short glass fibre-reinforced polyamide thermoplastic. *Journal of Materials Science*, 19(4):1145–1152, 1984.
- [96] K. L. Goh, R. M. Aspden, and D. W.L. Hukins. Review: Finite element analysis of stress transfer in short-fibre composite materials. *Composites Science and Technology*, 64(9):1091–1100, 2004.
- [97] Hansong Huang and Ramesh Talreja. Numerical simulation of matrix microcracking in short fiber reinforced polymer composites: Initiation and propagation. *Composites Science and Technology*, 66(15):2743–2757, 2006.

- [98] R. Talreja. Defect damage mechanics: Broader strategy for performance evaluation of composites. *Plastics, Rubber and Composites*, 38(2-4):49–54, 2009.
- [99] A. P. S. Selvadurai, B. M. Singh, and M. C. Au. The Matrix-Fiber Crack in an Elastic Solid. *Journal of Applied Mechanics*, 63(3):639–649, 9 1996.
- [100] J. J. Horst and J. L. Spoormaker. Fatigue fracture mechanisms and fractography of short-glassfibre-reinforced polyamide 6. *Journal of Materials Science*, 32(14):3641–3651, 1997.
- [101] S. Sirivedin, D. N. Fenner, R. B. Nath, and C. Galiotis. Matrix crack propagation criteria for model short-carbon fibre/epoxy composites. *Composites Science and Technology*, 60(15):2835–2847, 2000.
- [102] A. P.S. Selvadurai and A. Ten Busschen. Mechanics of the segmentation of an embedded fiber, part II: Computational modeling and comparisons. *Journal of Applied Mechanics, Transactions ASME*, 62(1):98–107, 1995.
- [103] J. Mullin, J.M. Berry, and A. Gatti. Some Fundamental Fracture Mechanisms Applicable to Advanced Filament Reinforced Composites. *Journal of Composite Materials*, 2(1):82–103, 1 1968.
- [104] Imad Hanhan, Francesco De Carlo, and Michael Sangid. Investigating Surface and Sub-Surface Damage in IM7/8552 via in-situ Synchrotron X-ray Computed Tomography. In *AIAA Scitech 2020 Forum*, pages 1–5, Orlando, FL, 1 2020. American Institute of Aeronautics and Astronautics.

A. ALGORITHM FOR DESTRUCTIVE OUT-OF-PLANE ANGLE ANALYSIS

1. **READ** reference '.csv' ellipse fit file containing $x^r, y^r, |\theta^r|, \phi^r$
2. **READ** target '.csv' ellipse fit file containing $x^t, y^t, |\theta^t|, \phi^t$
3. **READ** optical microscopy images
4. **SET** specimen radius and center coordinates
5. **SET** height between reference and target images, $h = 7$ (7 pixels corresponding to $\sim 4.5 \mu m$)
6. **SET** search limit criteria, $limit = 9$ (9 pixels corresponding to $\sim 5.8 \mu m$, approximately half the fiber diameter)
7. **GET** all centroidal parameters from the reference and target files

Search and Match Procedure

```

FOR reference fiber = 1 : length(reference fibers)
    a. CALCULATE projected translational displacement on the target image
    b. CALCULATE the candidate positions  $x_j^c$  and  $y_j^c$ 

        FOR target fiber = 1 : length(target fibers)
            a. CALCULATE the distance between the 2 candidate positions and the target fiber
            b. SELECT target fiber if it matches limit criteria
        END

    c. CALCULATE number of matches based on limit criteria
    d. SET best match based on the minimum difference of the in-plane-angle (if more than one match present)
    e. SET best match if the difference in  $\theta$  is less than  $15^\circ$  (which is selected as a suitable threshold for comparison)
    f. SET sign of  $\theta_l^r$  based on the candidate that yielded the match

END

```

Save and Visualize

8. **SAVE** updated fiber properties with sign of θ included as a '.csv'
9. **SHOW** optical microscopy images overlaid using *imfuse* with arrows using *quiver*

Figure A.1. Reference and target fiber matching algorithm outline.